



저작자표시-비영리-변경금지 2.0 대한민국

이용자는 아래의 조건을 따르는 경우에 한하여 자유롭게

- 이 저작물을 복제, 배포, 전송, 전시, 공연 및 방송할 수 있습니다.

다음과 같은 조건을 따라야 합니다:



저작자표시. 귀하는 원저작자를 표시하여야 합니다.



비영리. 귀하는 이 저작물을 영리 목적으로 이용할 수 없습니다.



변경금지. 귀하는 이 저작물을 개작, 변형 또는 가공할 수 없습니다.

- 귀하는, 이 저작물의 재이용이나 배포의 경우, 이 저작물에 적용된 이용허락조건을 명확하게 나타내어야 합니다.
- 저작권자로부터 별도의 허가를 받으면 이러한 조건들은 적용되지 않습니다.

저작권법에 따른 이용자의 권리는 위의 내용에 의하여 영향을 받지 않습니다.

이것은 [이용허락규약\(Legal Code\)](#)을 이해하기 쉽게 요약한 것입니다.

[Disclaimer](#)

Ph.D. DISSERTATION FOR NATURAL SCIENCE

**Experimental and Numerical Investigation of
Thermal Dispersion and its Significance for Designing
Groundwater Heat Pump (GWHP) Systems**

실험 및 수치적 고찰을 통한 개방형 지열
시스템에서의 열분산의 중요성 규명

Byeong-Hak Park

August 2019

School of Earth and Environmental Sciences

The Graduate School

Seoul National University

Experimental and Numerical Investigation of Thermal Dispersion and its Significance for Designing Groundwater Heat Pump (GWHP) Systems

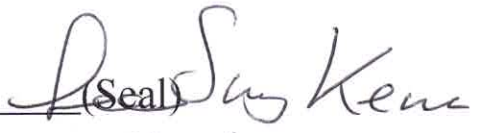
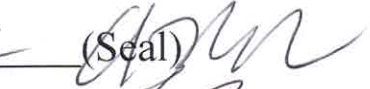
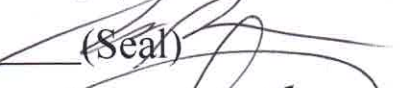
Advising Professor Kang-Kun Lee

Submitting a Ph.D. Dissertation for
Natural Science
May 2019

School of Earth and Environmental Sciences
The Graduate School
Seoul National University

Byeong-Hak Park

Confirming the Ph.D. Dissertation written by
Byeong-Hak Park
June 2019

Chair	이성근	(Seal)	
Vice Chair	이강근	(Seal)	
Examiner	이준기	(Seal)	
Examiner	김득진	(Seal)	
Examiner	이영민	(Seal)	

Abstract

Groundwater heat pump (GWHP) systems are not always efficient and sustainable. GWHP systems generally generate thermal plumes in the aquifer, which can adversely affect the system performance and the subsurface environment. The prediction of thermal plumes is therefore a matter of great concern in the design stage. The plumes can propagate in saturated porous media by conduction, advection, and dispersion. Thermal dispersion, however, has been underestimated in the subsurface heat transport processes by making use of default values in the numerical simulator or solute dispersivity as thermal dispersivity, without any field-based evaluation. These conventions or assumptions can play a crucial role in assessing thermal impacts of GWHP systems but they have not been fully examined so far.

Field and numerical studies were performed on the alluvial aquifer to investigate the importance of thermal dispersivity in GWHP systems. Numerical analysis indicates that thermal dispersivity has a great effect on the temperature distribution as well as the extent of thermal plume. Observed data also show that mechanical thermal dispersion can dominate over thermal diffusion even under the natural groundwater flow. Field-based model was modified to analyze the role of aquifer properties. The sensitivity analysis confirms and advances the previous finding that hydrodynamic parameters affect thermal plume development, and thereby reveals that aquifer properties composing mechanical thermal

dispersion are of great importance for predicting thermal plumes of GWHP systems.

A laboratory-scale experimental system was designed to control flow and temperature boundary conditions, and investigate the thermal dispersion behavior in porous media under forced flow field by injected water. Transport experiments using two different heat sources as tracers were conducted in saturated coarse sand ($d_{50} = 1.28$ mm) at various background flow velocities ($Re < 0.52$). Experimental and analytical results describe the scatter in the relationships between thermal dispersion coefficients and thermal front velocities with conduction dominant regime, nonuniform flow field, and heterogeneous thermal properties. Numerical results indicate that injected water greatly increases flow velocities and thermal dispersion coefficients, and thus makes the regions near the injection well stay in transition zone or convection dominant regime. Therefore, mechanical thermal dispersion becomes important even at low flow velocity.

Additional heat tracer tests were performed to investigate the validity of the general assumption that transverse thermal dispersivity is one-tenth of longitudinal one, and to analyze its impacts on thermal plume propagation. Experimental results confirm that such assumption can be violated. Numerical results show that the effect of dispersivity ratio is time-dependent, anisotropic, and varying with injection rates. These results indicate that the thermal dispersivity ratio can be significant for assessing the long-term environmental impacts of large-scale GWHP plants. Therefore, evaluation and reflection of dispersivity magnitude and ratio are necessary in the design stage of GWHP plants for sustainability.

This work describes the significance and role of thermal dispersion when using groundwater as energy resources. The findings of this work can have a significant implication on the heat

transport in saturated porous media as well as the efficient and sustainable use of shallow groundwater.

Keywords: Groundwater heat pump; Thermal dispersion; Thermal plume; Thermal dispersivity; Thermal dispersivity ratio; Environmental impact; Groundwater; Heat transport

Student number: 2013–20331

Contents

Abstract	i
List of Figures	xi
List of Tables	xvii
Chapter 1. Introduction	1
1.1. Motivation	1
1.2. Scope of work.....	5
Chapter 2. Thermal Dispersivity in GWHP Systems	7
2.1. Introduction	7
2.2. Field case study	11
2.2.1. Site description	11

2.2.2. Push-pull test.....	12
2.3. Numerical simulation of groundwater flow and heat transfer	18
2.3.1 Numerical simulation.....	18
2.3.2 Model discretization	19
2.3.3 Initial and boundary conditions	23
2.3.4 Effect of the aquifer thermal properties.....	27
2.3.5 Effect of injection and production rates.....	27
2.4. Results and discussion.....	29
2.4.1 Aquifer thermal properties	29
2.4.2 Injection and production rates	32
2.5. Conclusions	36

Chapter 3. Mechanical Thermal Dispersion as Aquifer

Properties	39
3.1. Introduction	39
3.2. Numerical simulation for sensitivity analysis.....	42

3.2.1. Modifying the developed model	42
3.2.2. Initial and boundary conditions.....	44
3.2.3. Sensitivity analysis	48
3.3. Results	50
3.3.1. Hydrogeological and thermal characteristics of the aquifer	50
3.3.2. Groundwater flow velocity	50
3.3.3. Injection/production rates	51
3.3.4. Arrival time	51
3.4. Discussion	57
3.5. Conclusions	59

Chapter 4. Thermal Dispersion Under Forced Flow Field by

Injection	61
4.1. Introduction	61
4.2. Laboratory experimental system.....	65
4.2.1. Experimental design	65

4.2.2. Heat sources	67
4.2.3. Data acquisition (DAQ) system	70
4.2.4. Physical properties of porous media	71
4.2.5. Temperature calibration.....	73
4.3. Heat transport experiments	78
4.3.1. Laboratory-scale heat transport experiments	78
4.3.2. Analytical model for the resistor tests	79
4.3.3. Numerical model for the injection tests.....	82
4.3.4. Parameter estimation	86
4.4. Results	90
4.4.1. Analytical modeling for heat tracer tests with a resistor	90
4.4.2. Numerical modeling for heat tracer tests with injected water	96
4.5. Discussions.....	103
4.5.1. Relationship between thermal dispersion coefficients and flow velocities ..	103
4.5.2. Impacts of injected water on flow and heat transport	104
4.6. Conclusions	108

Chapter 5. Anisotropy Ratio of Longitudinal to Transverse

Thermal Dispersivity	111
5.1. Introduction	111
5.2. Materials and methods	114
5.2.1. Experimental setup	114
5.2.2. Laboratory-scale heat tracer tests	119
5.2.3. Estimation of thermal properties	119
5.2.4. Heat transport modeling	120
5.2.5. Parameter estimation.....	123
5.3. Results	124
5.3.1. Heat transport experiments with a resistor	124
5.3.2. Heat transport experiments with injected water	134
5.4. Discussions.....	140
5.4.1. Thermal dispersion and flow velocity	140
5.4.2. Effects of thermal dispersivity ratio on thermal plume propagation	145

5.5. Conclusions	152
Chapter 6. Concluding Remarks	155
Bibliography	161
A. Uncertainty Analysis	177
Research Outcomes	179
Abstract in Korean	183

List of Figures

1.1. Factors causing pore-scale mechanical thermal dispersion	5
2.1. Location of the study area	13
2.2. Climatic data of Yangpyeong-gun for 10 years from 2004 to 2013	14
2.3. Comparison between observed temperature measurements and simulation results during the pull phase of the push–pull test	17
2.4. Finite element model domain and boundary conditions for the analysis of groundwater flow and heat transfer	20
2.5. Results of grid convergence study to determine an adequate spatial discretization	21
2.6. Simulation results to determine the maximum time-step length.....	21
2.7. Groundwater level and hydraulic gradient measured for 96 h before the push–pull test.....	25
2.8. Subsurface temperature logs with depth measured at well YSO-1	26

2.9. Thermal breakthrough curves at different observation points after injecting warm water	
.....	31
2.10. Effect of injection and production rates	34
3.1. Finite element model domain extended to groundwater flow direction and its	
boundary conditions for hydraulic head and temperature	43
3.2. Direction and velocity of groundwater measured at well YSO-1 (15 m bls) on August	
and November, 2014	46
3.3. Monthly mean surface air temperature measured at the study area and weather station	
of Yangpyeong-gun	47
3.4. Subsurface temperature logs with depth measured at well YSO-1	47
3.5. Groundwater temperature at pumping well according to case A ($i = 0.01$, $Q = 25$	
m^3/d)	53
3.6. Groundwater temperature at pumping well according to case B ($i = 0.005$, $Q = 25$	
m^3/d)	53
3.7. Groundwater temperature at pumping well according to case C ($i = 0.01$, $Q = 50$	
m^3/d)	54
3.8. Groundwater temperature at pumping well according to case D ($i = 0.005$, $Q = 50$	
m^3/d)	54

3.9. Arrival time of thermal plume observed at the pumping well according to four	
different cases	55
4.1. Schematic diagram of a laboratory experimental system for heat transport experiments	
in porous media	66
4.2. Illustration of an acrylic glass tank	68
4.3. Horizontal location of RTD sensors and heat sources at a height of 30 cm.....	71
4.4. The grain size distributions and images of sand grains for sands S3, S4, and S5.....	73
4.5. A temperature calibration procedure for RTD sensors	77
4.6. A 3-D model domain with the same dimensions as the laboratory experiments and	
boundary conditions for flow and heat transport.....	83
4.7. An example of the step-wise parameter estimation procedure.....	87
4.8. Temperature breakthrough curves observed at center and off-center locations (cross	
symbol), and CPS model results (solid line)	91
4.9. Two examples of the observed breakthrough curves and the best-fitted MCPS models	
for three observation points at two Darcy velocities	94
4.10. Relationships between the thermal dispersion coefficients and the thermal front	
velocities estimated from the best-fitted models	95
4.11. Comparison of numerical models with and without dispersion effects	97

4.12. Temperature breakthrough curves for two different heat source types of injected water and heat flux observed at three points	98
4.13. Influence of injected water on the flow field	100
4.14. Effect of injected water on thermal dispersion coefficients at various background flow velocities	101
4.15. Temperature breakthrough curves for different dispersivity values observed at two observation points.....	102
4.16. Up-scaled modeling results performed at a regional groundwater flow velocity of 3.64 m/d with various injection rates.....	106
5.1. Laboratory experimental system for thermal tracer tests	115
5.2. Injection rate of new tubing estimated at various rotational speeds	116
5.3. Images of experimental preparation.....	117
5.4. Hydrodynamic properties of coarse sands	118
5.5. The 3-D finite element model developed in the previous work and its boundary conditions for the simulations of flow and heat transport	122
5.6. Thermal plume dimensions defined by the plume lengths L1 and L2, and the plume width	124
5.7. Temperature–time series data observed at the center and off-center locations (cross	

symbol), and the corresponding best-fitted CPS model results (solid line)	126
5.8. Observed and calculated ranges of thermal conductivity	129
5.9. Observed temperature–time series data and their best-fitted MCPS models for three observation points at two Darcy velocities.....	130
5.10. The relationship between the thermal dispersion coefficients and the thermal front velocities for sand S5.....	132
5.11. The relationship between the thermal dispersion coefficients and the thermal front velocities for sand S4.....	133
5.12. Temperature–time series for the observed data (green circle) and the numerical model (grey solid line).....	135
5.13. Thermal plume extensions for steady-state simulations performed with different thermal dispersivity ratios at two Darcy velocities	136
5.14. Temporal variation of the thermal plume lengths with different thermal dispersivity ratios	138
5.15. Temporal variation of the thermal plume widths with different thermal dispersivity ratios at two Darcy velocities	139
5.16. Relative contribution of thermal diffusion and mechanical dispersion to the longitudinal dispersion coefficient for (a) S5 and (b) S4 sands.	143

5.17. Variation of thermal front velocity with increasing background flow velocity for coarse sands (a) S5 and (b) S4.....	144
5.18. Impact of injection rate on thermal plume dimensions with different thermal dispersivity ratios at a Darcy velocity of 29.47 m/d.....	149
5.19. Independent influence of longitudinal thermal dispersivity on thermal plume dimensions with an injection rate of 50 ml/min at a Darcy velocity of 29.47 m/d	150

List of Tables

2.1. Description of experimental devices used in this study	15
2.2. Model input parameters.....	22
2.3. Range of thermal properties for sensitivity analysis	28
2.4. Arrival time with distance from the injection well showing the effect of the aquifer thermal properties	35
3.1. Cases of the sensitivity analysis	49
3.2. Final temperature at pumping well according to pre-set cases	52
3.3. Change in arrival time of thermal plume observed in the pumping well, depending on four different cases	56
4.1. Calibration coefficients of 32 RTD sensors used for heat transport experiments with sand S3 in Chapter 5	75
4.2. Calibration coefficients of 32 RTD sensors used for heat transport experiments with	

sands S4 and S5 in Chapter 6	76
4.3. Hydrogeological and thermal parameters used for 3-D model simulation	85
4.4. Cases for different heat source types, background flow velocities, and injection rates.....	85
4.5. Thermal properties of porous medium and sensor locations derived from the best fit between the observations and CPS model.....	92
5.1. Hydrogeological and thermal parameters used for the developed numerical model .	121
5.2. Thermal properties of sand S5 and sensor locations estimated from the best-fitted CPS model	127
5.3. Thermal properties of sand S4 and sensor locations estimated from the best-fitted CPS model	128

Chapter 1

Introduction

1.1. Motivation

The Ground Source Heat Pump (GSHP) system is a space heating and cooling system that uses the ground or groundwater as a heat source in the winter and a heat sink in the summer because the temperature several tens of meters below the ground surface remains relatively stable throughout the year (e.g. more than 15 m depth in Florides & Kalogirou, 2005). As the GSHP system has a higher efficiency than conventional heating and cooling systems, it can contribute to reducing CO₂ emissions and saving energy costs (Bayer et al., 2012; Michopoulos et al., 2007; Ozlu et al., 2012; Park et al., 2013). In particular, buildings are responsible for about 40% of global energy consumption and corresponding CO₂ emissions (Mourshed, 2011). Recent studies also indicate that the energy demand for heating and cooling of buildings has an increasing trend in 21st century, mainly due to the growing demand in the developing countries and to climate change (Isaac & Van Vuuren, 2009; De Rosa et al., 2014). In this context, the GSHP system can have a significant role in coping with global climate change and ensuring energy security.

The GSHP systems are generally classified into closed-loop and open-loop systems. The GWHP system is an open-loop GSHP system that draws groundwater from one or more wells with relatively stable temperatures throughout the year, exchanges heat energy with the water, and generally discharges it through another well(s). This direct use of groundwater makes the GWHP system more efficient and suitable for large-scale heating and cooling facilities, but there are two thermal risks (Banks, 2009) because the groundwater is usually reinjected into the aquifer to avoid a hydraulic risk (e.g. water level decline, groundwater depletion, and sea water intrusion). One of the thermal risks is the thermal interference between pumping and injection wells which is called various names such as thermal short-circuit, thermal feedback, or thermal recycling (see Casasso & Sethi, 2015), and can degrade the system efficiency. The other risk is the environmental impacts that can adversely affect the sustainable use of groundwater in downstream regions. Therefore, the design of the GWHP system aims to predict the thermal anomalies originated from the injected water, minimize the thermal risks, and thus ensure the efficiency and sustainability of the system.

In recent years, some studies have been conducted to reduce thermal impacts of GWHP systems and to meet the heating and cooling demand of buildings (Gao et al., 2013; Lo Russo et al., 2011; Nam & Ooka, 2010; Zhou et al., 2013). Their results show that the groundwater flow condition is of great importance on the design of GWHP systems, confirming that the heat transport process in open-loop systems occurs mainly by advection rather than conduction, differently from closed-loop systems. These studies, however, have focused on the efficient system design to avoid or reduce the thermal interference between the wells. As the shallow geothermal installation for space heating and cooling is increasing (Bayer et al., 2012), there is a growing concern on assessing and managing the environmental impact of thermal plumes

which may conflict with the potential use of adjacent facilities.

Thermal plumes from the injection wells of GWHP systems propagate in saturated porous media by three physical mechanisms of conduction, advection, and mechanical dispersion, which is closely related to the physical properties of the media. The prediction of thermal plumes and the design of GWHP systems are therefore highly dependent on the hydrogeological and thermal properties of aquifers (Casasso & Sethi, 2015; Lo Russo & Civita, 2009; Lo Russo et al., 2012; Nam & Ooka, 2010; Zhou et al., 2013). Mechanical thermal dispersion, however, has often been neglected or underestimated in the simulation of flow and heat transport in porous media because thermal diffusion is dominant (Molina-Giraldo et al., 2011 and references therein). This is evident from the fact that the magnitude of molecular diffusion is 10^{-9} m²/s, while that of thermal diffusion is 10^{-7} m²/s (de Marsily, 1986). As a consequence, the thermal dispersivity values of numerical studies for predicting the thermal plume propagation has been assumed to be default values in the numerical simulator or solute dispersivity values without any field-based evaluation (Lo Russo & Civita, 2009; Lo Russo et al., 2011; Lo Russo et al., 2012; Nam & Ooka, 2010; Zhou et al., 2013).

Mechanical thermal dispersion is a physical process that represents the heat spreading due to the velocity discrepancy. As shown in Figure 1.1, the actual velocities are not uniform and deviate from the mean flow velocity because of friction, pore size, and flow path at the pore level (Freeze & Cherry, 1979). This spatial variability of flow velocity at the small scale causes the heat spreading in longitudinal and transverse directions. At the field scale, the spatial heterogeneity of hydraulic conductivity and porosity results in the heterogeneous flow field, and thus macroscopic dispersion (Freeze & Cherry, 1979). As a groundwater flow equation is based on a Darcian continuum where the flow over a control volume is averaged (Yeh et al.,

2015), mechanical thermal dispersion is required to represent the influence of spatially variable velocity on heat transport in a porous medium. Therefore, ignoring dispersion process can lead to incorrect predictions of thermal behavior in the subsurface. For example, Alcaraz et al. (2016) quantified the shallow geothermal potential and related environmental impacts at a regional scale with a GIS methodology that considers the advection, dispersion, and transient thermal state. The analysis results suggest that, for high Darcy velocities ($> 10^{-6}$ m/s), neglecting dispersion effects can overestimate the thermal plume length by up to 3 times, while it can lead to the underestimation for the velocities of 10^{-7} to 10^{-6} m/s.

In particular, the assumption on thermal dispersivity values is highly likely to be violated in the GWHP environment. First of all, field-scale thermal dispersivity has a wide range of values (0.1–100 m) in the literatures (Molina-Giraldo et al., 2011; Stauffer et al., 2013). Moreover, large volume of groundwater which is pumped and re-injected in GWHP systems can increase the magnitude of thermal dispersion because it depends on the flow velocity (Rau et al., 2012a and references therein). However, thermal dispersion behavior in such disturbed flow field has not been fully investigated so far.

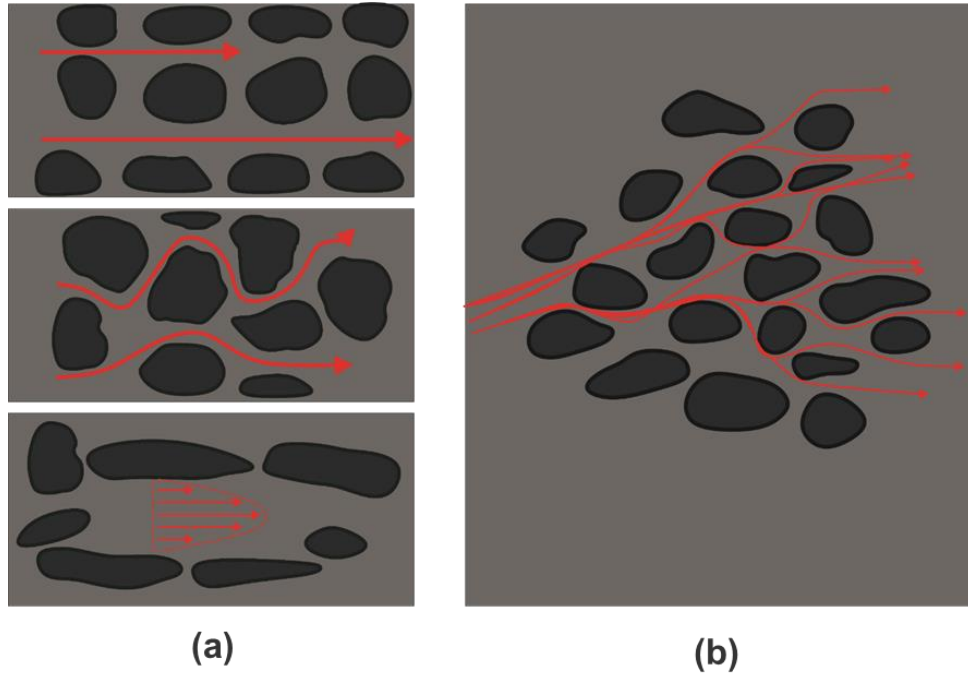


Figure 1.1. Factors causing pore-scale mechanical thermal dispersion in (a) longitudinal and (b) transverse directions

1.2. Scope of work

This work investigates the validity of general assumption on thermal dispersion under forced flow field of GWHP environment. For these purposes, the site thermal dispersivity is estimated by a field push-pull test, and its role on the subsurface heat transport process is analyzed by numerical modeling for GWHP systems (see Chapter 2). In Chapter 3, mechanical dispersion is evaluated in terms of aquifer properties. Field-based numerical model is further extended to perform the sensitivity analysis of aquifer properties under different flow and transport boundary conditions, and evaluate their influences in designing GWHP systems. To overcome the limitations of the complexity of the research area, in Chapter 4, a laboratory experimental

system is designed and developed for precise investigation of dispersion behavior through thermal tracer tests in a saturated porous medium under controlled boundary conditions. Transport experiments on the laboratory scale using two heat sources as tracers are conducted, and temperature–time series data are analyzed by analytical and numerical modeling to identify the effect of injected water on flow field, thermal dispersion coefficients, and the relevant heat transport processes (Chapter 4). In Chapter 5, the validity of the commonly used thermal dispersivity ratio is investigated and its spatiotemporal impacts on thermal plume propagation are discussed for sustainable design of GWHP systems. Therefore, this dissertation examines the significance and role of thermal dispersion through laboratory and field experiments, analytical modeling, and numerical simulations, and discusses its implications for using groundwater as a renewable and sustainable energy resource.

Chapter 2

Thermal Dispersivity in GWHP Systems

This chapter is based on the publication:

Park, B. H., Bae, G. O., & Lee, K. K. (2015a). Importance of thermal dispersivity in designing groundwater heat pump (GWHP) system: Field and numerical study. *Renewable Energy* 83, 270–279.

2.1. Introduction

Since the “Promotional Law of New and Renewable Energy Development, Use and Dissemination” was enacted in 2004, the use of ground source heat pump (GSHP) systems in Korea has steadily increased in recent years because of their benefits and governmental support (Kwon et al., 2012; KEMCO, 2013; Lee, 2009). GSHP systems can be classified into closed- and open-loop systems depending on the types of subsurface heat exchangers used. In the Republic of Korea, closed-loop systems and standing column wells (SCWs) comprise 96.4% of installed GSHP systems (Kwon et al., 2012). The application of open-loop systems using more than two wells is rare.

An open-loop system is generally characterized by a higher coefficient of performance

(COP), lower initial cost, and flexible system size. The hydrogeological conditions of the groundwater in Korea have the potential to facilitate the use of groundwater heat pump (GWHP) systems because a large number of monitoring wells show stable groundwater temperatures, shallow water levels, and high well yields (Lee et al., 2006).

The heat transfer process in open-loop systems differs from that in closed-loop systems. In closed-loop systems, heat transfer between the subsurface and borehole heat exchangers takes place through conduction and the thermal conductivity of the subsurface medium has a great effect on the COP of the GSHP system (Casasso & Sethi, 2014; Kim et al., 2008). For example, Kim et al. (2008) developed a numerical model to simulate the subsurface heat transport and performed the sensitivity analysis on the design parameters of a closed-loop GSHP system. The analysis results showed that thermal conductivity of the aquifer has a great impact on the performance of GSHP systems. For this reason, thermal response tests are performed to estimate thermal conductivity before designing a closed-loop GSHP system. Heat transfer in open-loop systems, however, occurs mainly through advection rather than conduction. A different test method is necessary for an efficient design of a GWHP system.

In recent years, studies have been conducted to minimize the environmental effects resulting from pumping and injection and to enhance the efficiency of GWHP systems. Lo Russo & Civita (2009) investigated site characteristics and performed numerical simulations to assess the applicability of a GWHP system for a new building complex near Turin, Italy. This study demonstrated that the hydrogeological conditions of the IKEA (the world's largest furniture retailer) site could supply the heating and cooling needs of the buildings with limited environmental impact. Nam & Ooka (2010) conducted three-dimensional (3-D) ground heat and water transfer simulation and cooling and heating experiments using full-scale equipment.

The results confirmed that the groundwater condition and well position should be taken into account to design an efficient GWHP system. Zhou et al. (2013) believed that thermal breakthrough is a very important aspect in the design of a GWHP system and analyzed the thermal behaviors in pumping and injecting well groups through numerical simulation and experiments on heat–water transfer. They also confirmed that the groundwater flow condition has an important role in the design of a GWHP system. Lo Russo et al. (2011) examined alternative designs using two storage tanks associated with an open-loop GWHP system. The results showed that the use of storage systems provides environmental benefits as well as a reduction in energy consumption. Casasso & Sethi (2015) thought that the thermal recycling phenomenon impairing the performance of GWHP systems should be taken into account in the design process (or design stage). They developed an open-source numerical code called TRS, which deals with thermal recycling in the presence of a regional groundwater flow, for preliminary and sensitivity analyses.

However, previous studies on the efficiency of a GWHP system have been focused on groundwater hydraulic conditions and well configurations, and many of these studies used the solute dispersivity or relevant default values as the site thermal dispersivity in numerical simulations without any field-based evaluation. Studies that consider thermal dispersivity, especially with an experimental investigation, are relatively rare. Even though there are controversial points of view on whether the relationship between thermal dispersivity and fluid velocity is linear (Anderson, 2005; de Marsily, 1986; Hatch et al., 2006; Keery et al., 2007; Rau et al., 2010; Vandenbohede et al., 2009; Vandenbohede et al., 2010) or not (Green et al., 1964; Levec et al., 1985; Metzger et al., 2004; Rau et al., 2012; Testu et al., 2007), the effect of thermal dispersion on heat transport increases with the increase in fluid velocity. Because

the process of groundwater pumping and injection can cause the flow velocity around wells to be faster than natural groundwater velocity, thermal dispersion will have a greater effect on the heat transport process in a GWHP system. Lo Russo et al. (2009) confirmed that the dimensions and geometry of a thermal plume particularly depend on the thermal dispersivity values of subsurface formations. Therefore, in this chapter, a field push–pull test using heat as a tracer was performed to estimate the site thermal dispersivity. The measured temperature data from the test were compared with the result of groundwater and heat transfer simulations based upon the site characteristics. This paper also describes a sensitivity analysis of aquifer thermal properties and discusses the effect of increased pumping and injection rates.

2.2. Field case study

2.2.1. Site description

The study area is located at the Han River Environment Research Center, a branch of the National Institute of Environmental Research (NIER), Yangpyeong-gun, Gyeonggi-do, Korea (Figure 2.1). The research center studies contaminants, water quality, and ecological system in Han River, and has three buildings of the Main Building, the Test Building, and the Exhibition Hall, located within 100 m from the Han River. An open-loop GWHP system is designed for space heating and cooling of the Test Building.

Figure 2.2 illustrates the climatic data of Yangpyeong-gun for the range of 10 years from 2004 to 2013 (KMA, 2014). The mean annual air temperature is 11.7 °C, and the mean monthly air temperatures for the hottest August and the coldest January are 25.5 °C and -3.9 °C, respectively. The mean annual precipitation for this range of 10 years is 1,646.9 mm; the precipitation in summer (June–August) and that in winter (December–February) is approximately 65% and 4% of the total annual precipitation, respectively.

Three wells used for studying the hydrogeological and thermal conditions of the alluvial aquifer were installed in the test site (see Figure 2.1). Wells YSO-1 and YSO-2 are 150 mm in diameter and 50 m in depth, while well YSP is 200 mm in diameter and 32 m in depth. Downhole log data in the study area indicate the presence of three distinct layers. There is a silty sand layer down to a depth of 13 m, a gravel layer below 13 m down to a depth of 16 m, and a gneiss body below a depth of 16 m. The unconfined aquifer formed in the silty sand layer is hydraulically connected to the Han River. The mean hydraulic conductivity of the layer, based on laboratory experiments, is 3.926×10^{-5} m/s. The hydrogeological properties of the

gravel layer were estimated using a pumping test. The test data yielded the hydraulic conductivity of 4.434×10^{-3} m/s. Thermal properties such as thermal conductivity, volumetric heat capacity, and thermal diffusivity were measured by the Korea Institute of Geoscience and Mineral Resources (KIGAM).

2.2.2. Push–pull test

To generate experimental data to estimate the site thermal dispersivity, a push–pull test using heat as a tracer was designed. The test consists of two phases. During the push phase, chilled or warm water (compared with the undisturbed groundwater) is injected into a screened well. During the consequent pull phase, water is extracted from the same well. The fluid temperature is measured at regular intervals during the test. To perform the test, well YSP screened over the gravel layer was used as an injection/extraction well. The undisturbed groundwater temperature measured 15 m below the surface was approximately 12.79°C. Warm water of approximately 30°C was injected for 64 min at a mean rate of 21.6 m³/d. During the pull phase, water was extracted for 91 min at a mean rate of 24.0 m³/d. The groundwater temperature was measured once every 2 s during the test. The specifications of experimental devices used for the push–pull test are shown in Table 2.1.

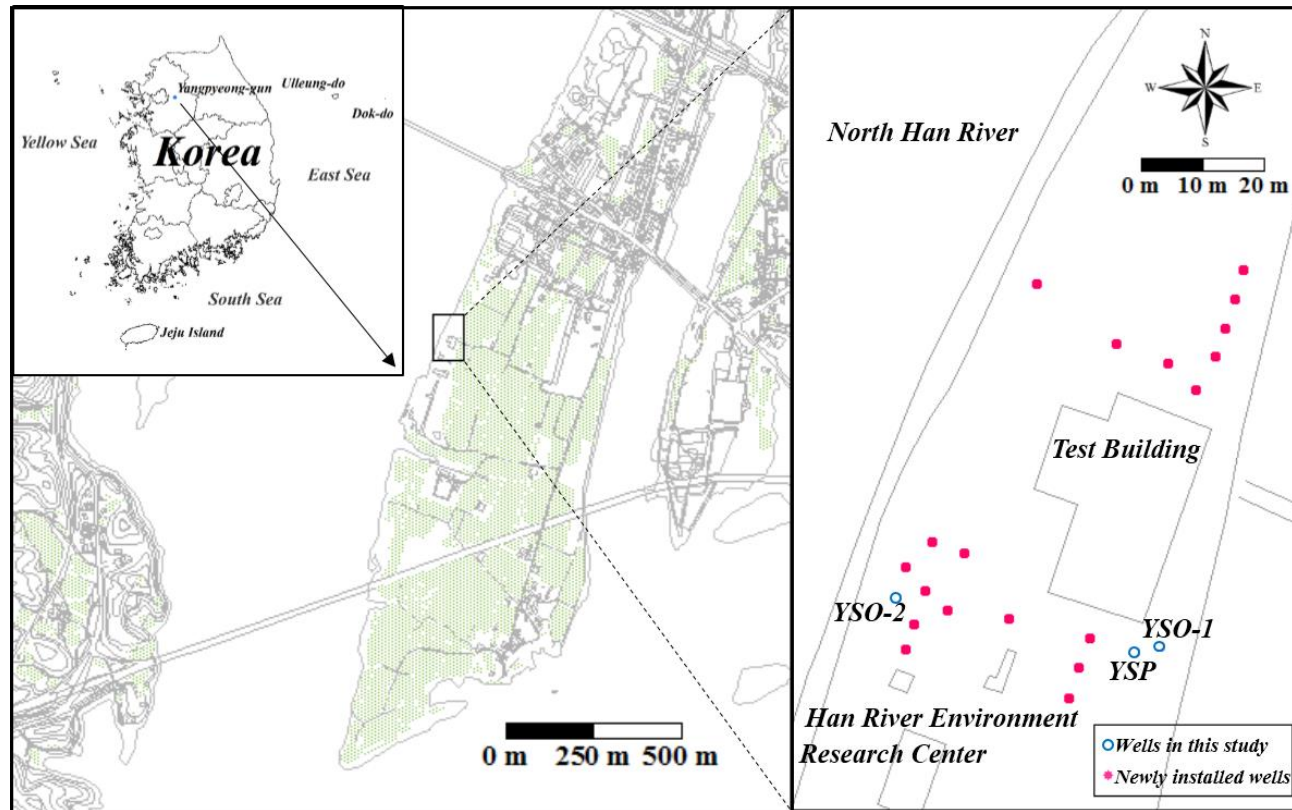


Figure 2.1. Location of the study area. The site is located at Han River Environmental Research Center, adjacent to north Han River, where there are three buildings. GWHP system is designed for Test building among them, a total of 22 wells for monitoring and heat exchange were installed around the building.

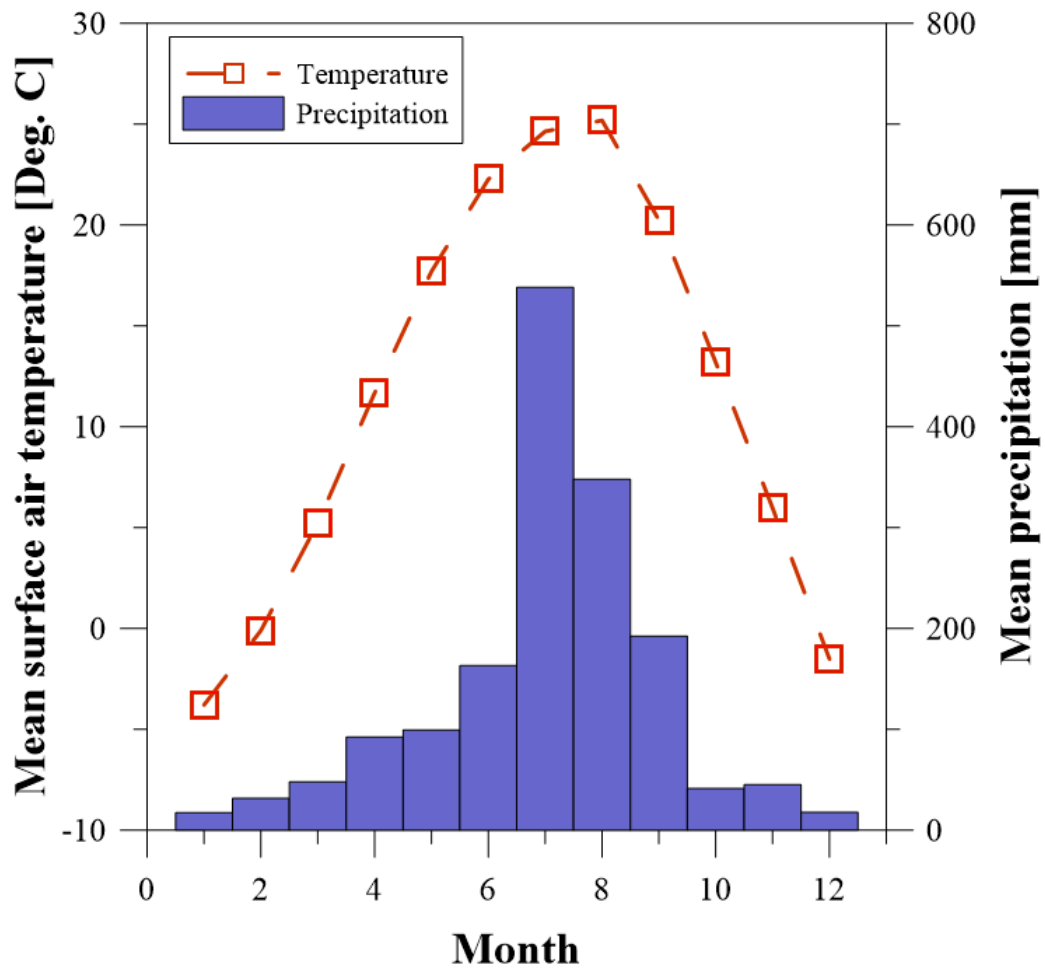


Figure 2.2. Climatic data of Yangpyeong-gun for 10 years from 2004 to 2013 (KMA, 2014).

Table 2.1. Description of experimental devices used in this study.

	Measurements	Specifications	Manufacturer
MP1 pump	Pumping injection	Power input	1.3 kW
		Voltage	3 × 220 V, 400 Hz
		Maximum current	5.5 A
		Motor protection	Built-in thermal switch
		Water temperature	0°C to 35°C
		Discharge port	Rp 3/4
		Continuous operation	Max. 500 h
	Net weight	2.5 kg	
BaroDiver	Air temperature	Measuring range	-20°C up to 80°C
		Accuracy	± 0.1°C
		Resolution	0.01°C
	Air pressure	Measuring range	1.5 mH ₂ O
		Accuracy	± 0.5 cmH ₂ O
		Resolution	0.25 cmH ₂ O
CTD-Diver	Temperature	Measuring range	-20°C up to 80°C
		Accuracy	± 0.1°C
		Resolution	0.01°C
	Conductivity	Measuring range	0 up to 120 mS/cm
		Accuracy	± 10 µS/cm
		Resolution	1 µS/cm
	Pressure	Measuring range	10 mH ₂ O
		Accuracy	± 0.5 cmH ₂ O
		Resolution	0.25 cmH ₂ O
TLC Meter (Model 107)	Temperature	Measuring range	-15°C up to 50°C
		Accuracy	± 0.2°C
		Resolution	0.1°C
	Level	Length	60 m
		Resolution	1 mm
	Conductivity	Measuring range	0 up to 80 mS/cm
		Accuracy	± 100 µS/cm
		Resolution	1 µS/cm
	Water Level Meter (Model 101)	Level	Length
Resolution			1 mm
AquaVISION Colloidal Borescope	Groundwater flow rates and directions	Max. operating depth	305 m
		Max. water pressure	843.7 mH ₂ O
		Operating temperature range	-10°C up to 45°C
		Camera Field of View	2.7 to 2 mm
		Depth of focus	0.2 mm

The blue circle and solid line in Figure 2.3 represent the measured temperature during the pull phase of the push–pull test. To estimate the site thermal dispersivity, 3-D numerical simulations using FEFLOW® were performed. In the simulations for the analysis of the push–pull test, the injection/production well was assumed to be at the center of the model domain. Details about the numerical model will be explained in the next section. Breakthrough curves from the simulation results were fitted to the measured data by varying the thermal dispersivity and the hydraulic gradient. To estimate the quality of fit, the root mean square error (RMSE) was used as a fitness criterion:

$$RMSE = \left[\sum_{i=1}^n \frac{(M_i - S_i)^2}{n} \right]^{0.5} \quad (2.1)$$

where M_i are the measured values and S_i are the simulated values. From the best fit, which minimizes the RMSE (see Figure 2.3), the site thermal dispersivity (0.4 m) and the hydraulic gradient (0.0095) were determined. The region has complicated groundwater velocity fields mainly caused by river stage fluctuation. Thus, the estimated hydraulic gradient denotes the gradient during the test period.

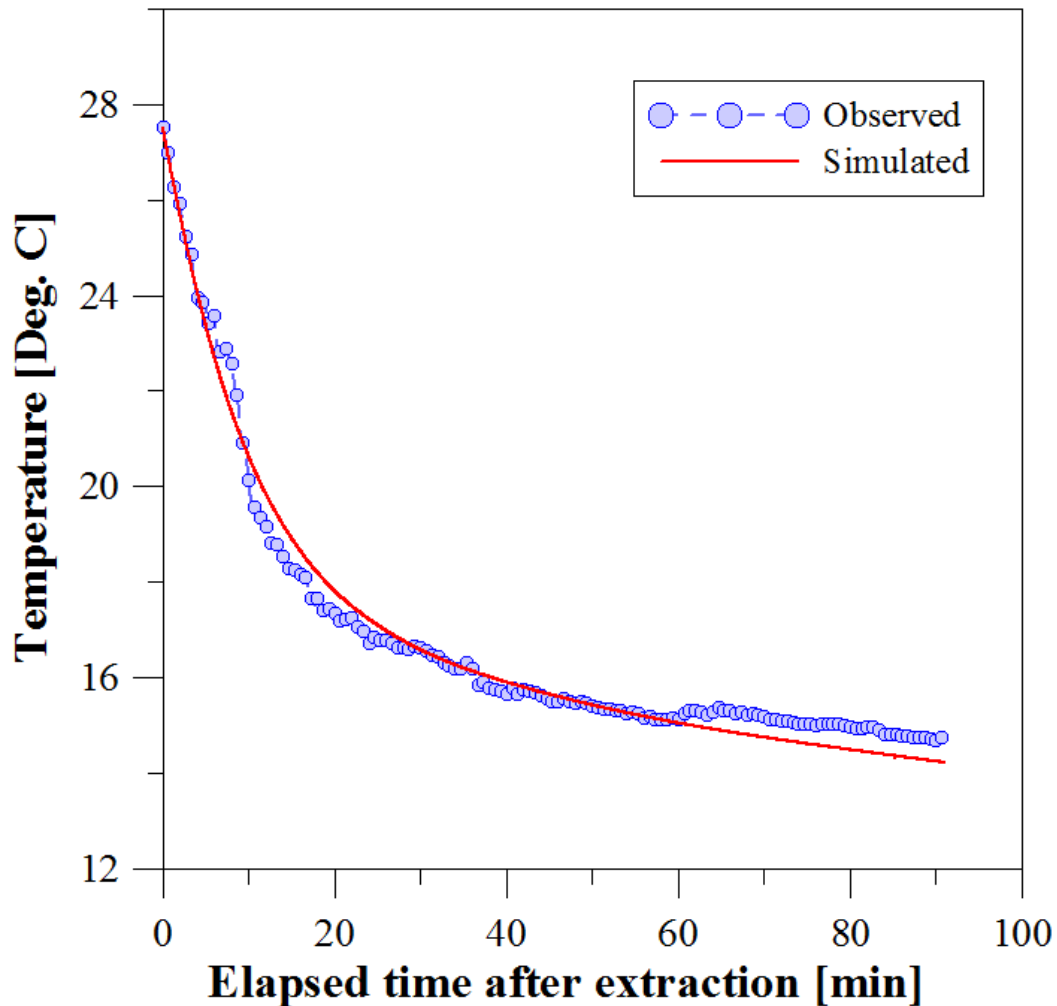


Figure 2.3. Comparison between observed temperature measurements and simulation results during the pull phase of the push–pull test. The difference between numerical models for the push–pull test and case simulation is the number of wells and its locations. The well for the push–pull test is located at the center of the numerical model ($x = y = 50$ m). The hydraulic head and ground temperature distributions were calculated by setting the measured data as initial and boundary conditions (Section 2.3.3). The injection/production rates and injection temperature during the experiment were assigned over the screened interval of the well (see Sections 2.2.2 and 2.3.3).

2.3. Numerical simulation of groundwater flow and heat transfer

2.3.1. Numerical simulation

A numerical model was used to analyze the push–pull test data and to estimate the site thermal dispersivity. It was also used to estimate the effect of the aquifer thermal properties and the increased pumping and injection rates on the subsurface thermal plume evolution. There are a variety of numerical codes that can deal with hydraulic, thermal, and chemical processes. In this study, numerical modeling of the groundwater flow and heat transfer was conducted using the FEFLOW finite element code. The fundamental mathematical basis of the code is formed by the principles of conservation for mass, momentum, and energy for solid, liquid, and gas phases (Diersch, 2005a).

Mass conservation of a phase:

$$\frac{\partial}{\partial t} (\varepsilon_\alpha \rho^\alpha) + \frac{\partial}{\partial x_i} (\varepsilon_\alpha \rho^\alpha v_i^\alpha) = \varepsilon_\alpha \rho^\alpha Q_\rho^\alpha \quad (2.2)$$

Momentum conservation of a phase:

$$v_i^\alpha + \frac{k_{ij}^\alpha}{\varepsilon_\alpha \mu^\alpha} \left(\frac{\partial p^\alpha}{\partial x_j} - \rho^\alpha g_j \right) = 0 \quad (2.3)$$

Energy conservation of a phase:

$$\frac{\partial}{\partial t} (\varepsilon_\alpha \rho^\alpha E^\alpha) + \frac{\partial}{\partial x_i} (\varepsilon_\alpha \rho^\alpha v_i^\alpha E^\alpha) + \frac{\partial}{\partial x_i} (j_{iT}^\alpha) = \varepsilon_\alpha \rho^\alpha Q_T^\alpha \quad (2.4)$$

where α is the phase indicator, such as the liquid water, vapor water, and soil solid particles, ε_α is the volume fraction of α phase ($0 \leq \varepsilon_\alpha \leq 1$ and $\sum_\alpha \varepsilon_\alpha = 1$), ρ [kg/m³] is the density, v_i [m/s] is the average linear velocity vector, Q_ρ and Q_T are the mass and heat supply, k_{ij} [m²] is the permeability tensor, μ [kg/m-s] is the viscosity of α phase, P is the pressure, g_j is the gravity

vector, E is the internal (thermal) energy, and j_{iT} is the Fourierian heat flux vector.

2.3.2. Model discretization

A 3-D finite element grid (686,817 nodes and 640,000 elements) was constructed for a 3-D model domain with dimensions of 100 m \times 100 m \times 50 m (Figure 2.4). The model domain, which has four wells located 20 m apart, was discretized into square elements ($\Delta x = \Delta y = 0.5$ m). This mesh spacing was determined after a grid convergence study to calculate the arrival time of the thermal plume at three observation points located 20, 40, and 60 m downstream from the injection well (Figure 2.5). The distribution of the layers in the model was determined from the downhole log data. Thus, the model domain consists of three layers with distinct hydrogeological and thermal properties, and each layer is divided into several sublayers. The hydrodynamic and thermal parameters used for FEFLOW simulation are listed in Table 2.2. The aquifer properties, which could not be estimated from the experiments, are based on the values from the literature (Anderson & Woessner, 1992; Cha et al., 2007; Fetter, 2001; Freeze & Cherry, 1979; Johnson, 1967).

Simulations were performed under transient flow and transient transport conditions using the forward Adams–Bashforth/backward trapezoidal predictor–corrector scheme for automatic time-step control. The initial time step was set to be 10^{-6} d with a maximum time step of 0.2 d. The maximum time step was determined from the result of simulations to verify that the temporal discretization was adequate. As shown in Figure 2.6, the numerical calculation stabilized when the time step was smaller than 0.2 d

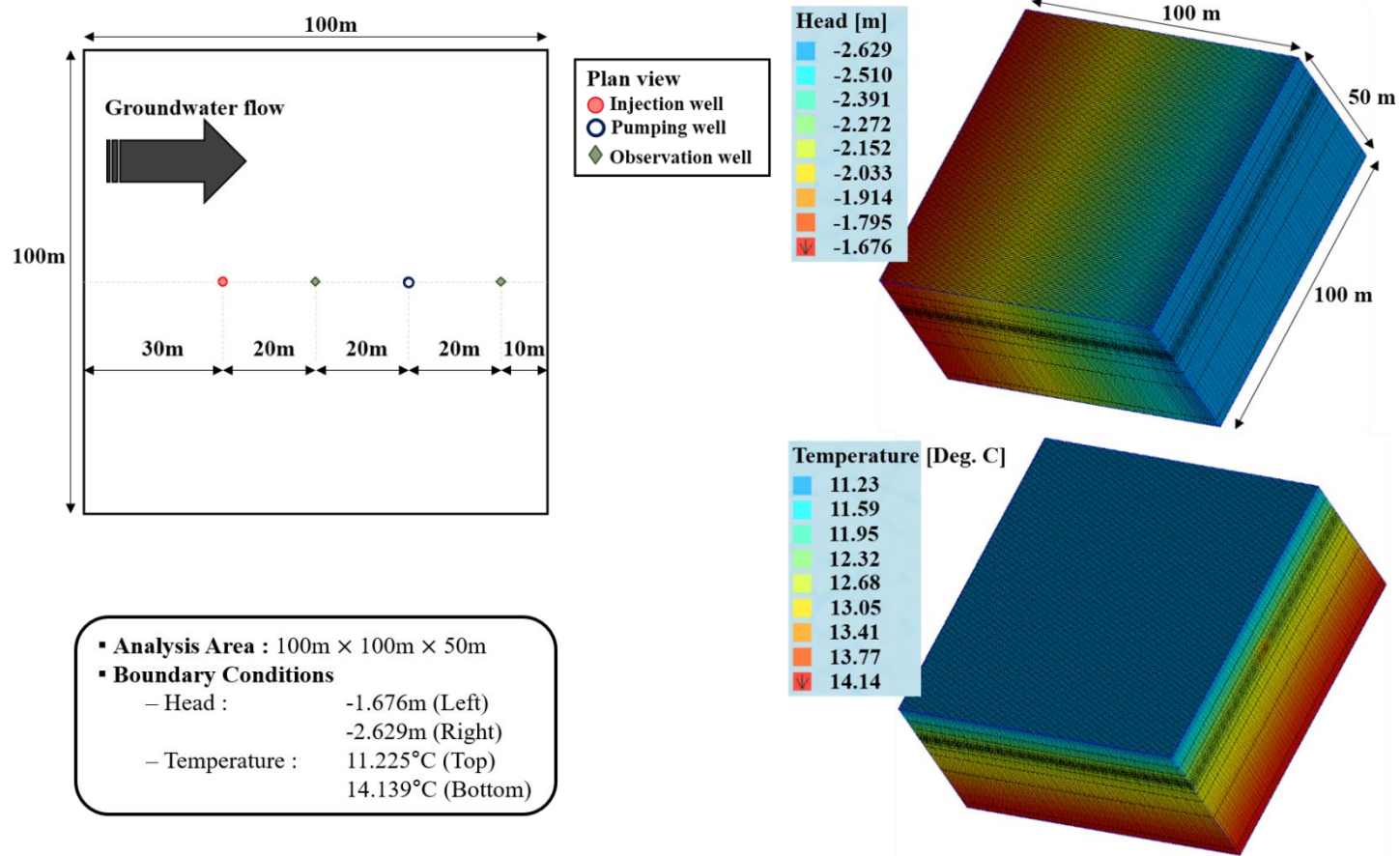


Figure 2.4. Finite element model domain and boundary conditions for the analysis of groundwater flow and heat transfer.

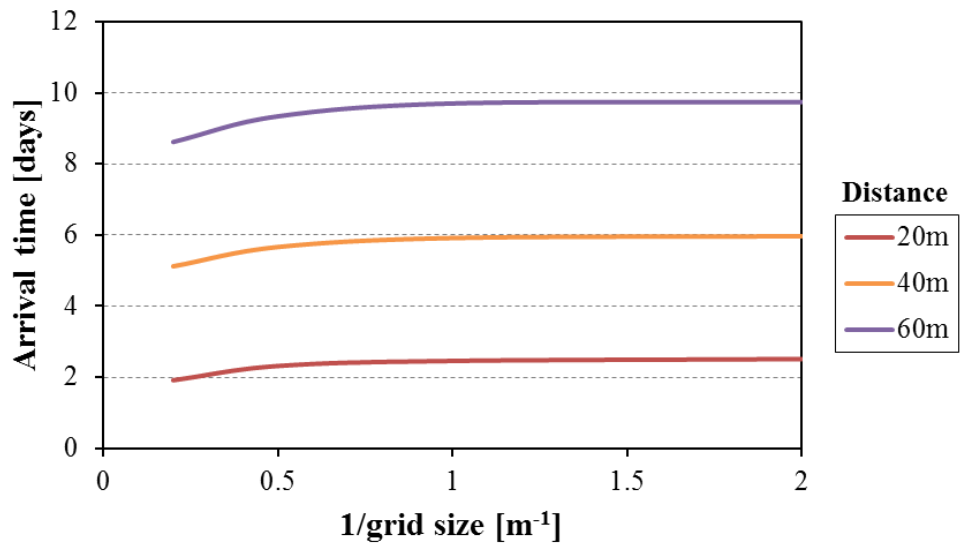


Figure 2.5. Results of grid convergence study to determine an adequate spatial discretization.

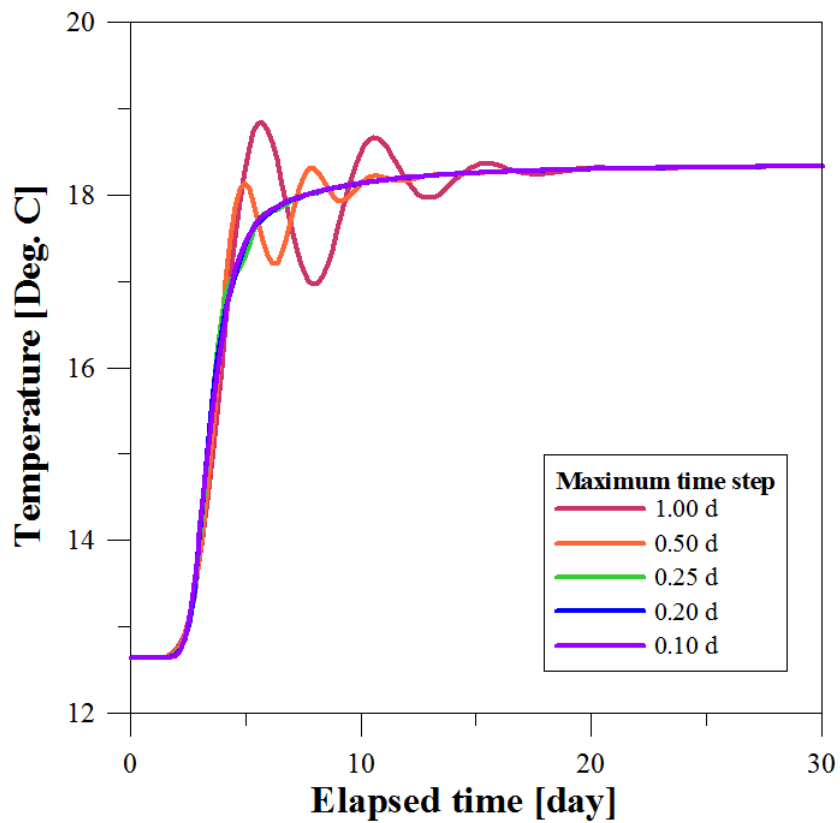


Figure 2.6. Simulation results to determine the maximum time-step length.

Table 2.2. Model input parameters.

Parameter	Symbol	Unit	Value		
			Layer 1 (Silty sand)	Layer 2 (Gravel)	Layer 3 (Gneiss)
Horizontal hydraulic conductivity	$K_{xx} =$ K_{yy}	10^{-4} m/s	0.3926	44.34	0.0001
Vertical hydraulic conductivity	K_{zz}	10^{-4} m/s	0.03926	4.434	0.00001
Specific yield	S_y	—	0.2	0.2	0.02
Specific storage	S_s	1/m	0.0001	0.0001	0.000001
Porosity	n	—	0.35	0.25	0.025
Thermal conductivity of the solid	λ^s	$\text{W m}^{-1}\text{K}^{-1}$	1.28	2.9	2.9
Thermal conductivity of the fluid	λ^f	$\text{W m}^{-1}\text{K}^{-1}$	0.65	0.65	0.65
Volumetric heat capacity of the solid	$\rho^s C^s$	$10^6 \text{ J m}^{-3}\text{K}^{-1}$	2.14	2.1	2.1
Volumetric heat capacity of the fluid	$\rho^f C^f$	$10^6 \text{ J m}^{-3}\text{K}^{-1}$	4.2	4.2	4.2
Longitudinal thermal dispersivity	β_L	m	0.4	0.4	0.4
Transverse thermal dispersivity	β_T	m	0.04	0.04	0.04

2.3.3. Initial and boundary conditions

Figure 2.7 shows the groundwater level and hydraulic gradient that were measured for 96 h before the push–pull test. Because the groundwater level fluctuates over time, it is difficult to derive a realistic areal groundwater head distribution. Therefore, the head distribution was calculated through a 3-D steady-state flow simulation where the measured groundwater level right before the test was set as the initial condition and the measured hydraulic gradient was reflected as the Dirichlet boundary condition by specifying the heads along the left and right sides of the model domain. The resulting hydraulic head distribution was obtained through model calibration with the measured data, and then a transient simulation was performed. Injection and production rates were assigned at the specific nodes of well locations in the gravel layer. All nodes representing the injection/production well were connected with highly conductive discrete feature elements to simulate the fully penetrating borehole (Diersch, 2005b). This approach was also used in aquifer storage and recovery (ASR) experiments (Ward et al., 2007; Miotliński et al., 2011).

Since the air temperature in the study area has just started to be monitored, there was not enough data to draw annual mean air temperature. Hence, the air temperature data at the Yangpyeong weather station of the Korea Meteorological Administration (KMA), about 17 km away from the study area, were used. Based on the data from the weather station, the surface temperature was set at 11.225°C as the boundary condition on the top of the model. To determine the boundary condition at the bottom of the model, the regression analysis was performed using the temperature logs at well YSO-1 (Figure 2.8). Thus, the subsurface temperature distribution was computed. The calculated temperature of 12.639 °C at a depth of 15 m below the surface closely matched the measured undisturbed groundwater temperature of

12.79°C at the same depth. The injected water temperature was set to the injection well. The temperature dependence of the fluid density and viscosity is not considered in this study.

The dimensions of the model domain were determined to be large enough in consideration of the effect of boundary conditions. Because the radius of hydraulic influence is larger than that of thermal influence, drawdown caused by pumping was used as a criterion. From the Theis equation (Theis, 1935) dealing with hydraulics of aquifers under transient conditions, drawdown 30 m apart from a pumping well was estimated to be about 22 mm even under no flow condition. Therefore, the effect of boundary conditions will be negligible.

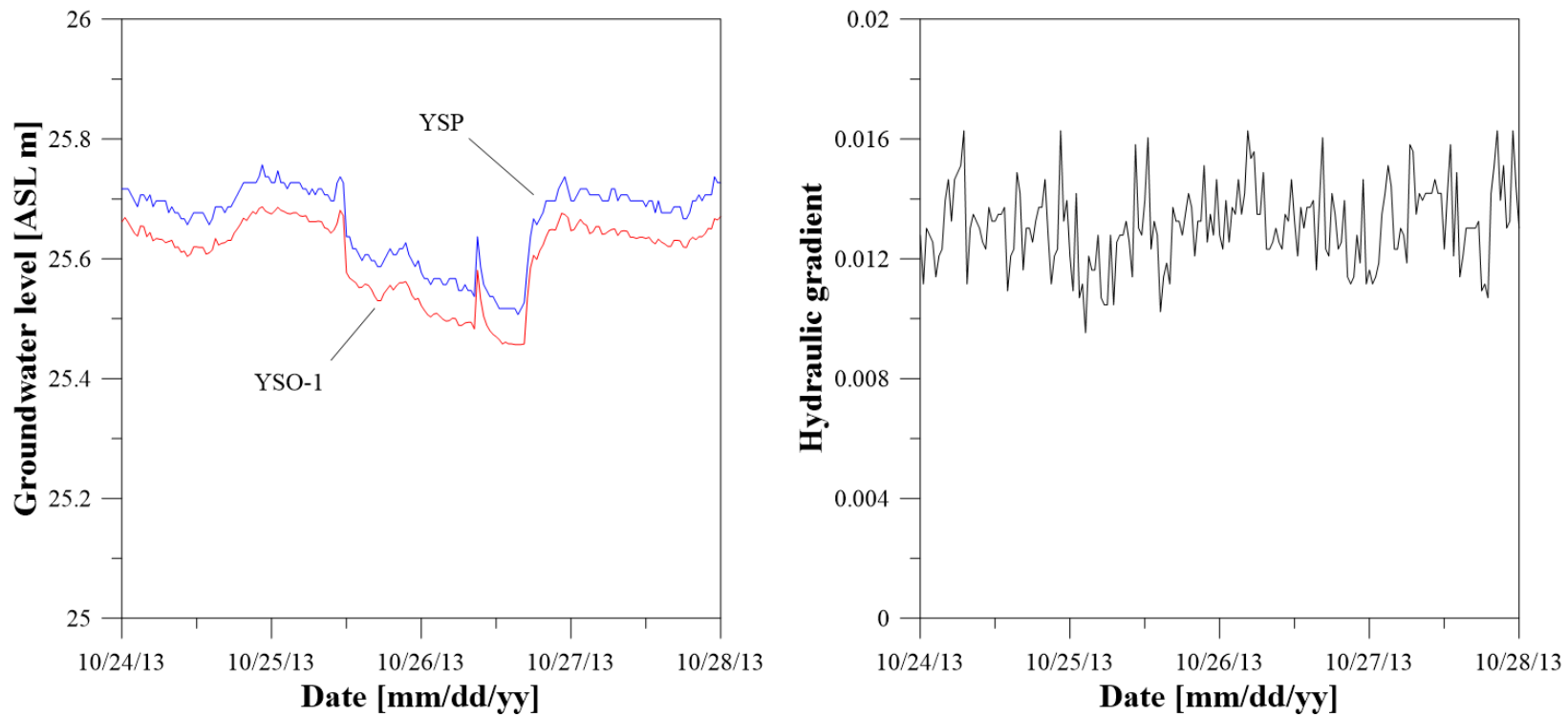


Figure 2.7. Groundwater level and hydraulic gradient measured for 96 h before the push-pull test.

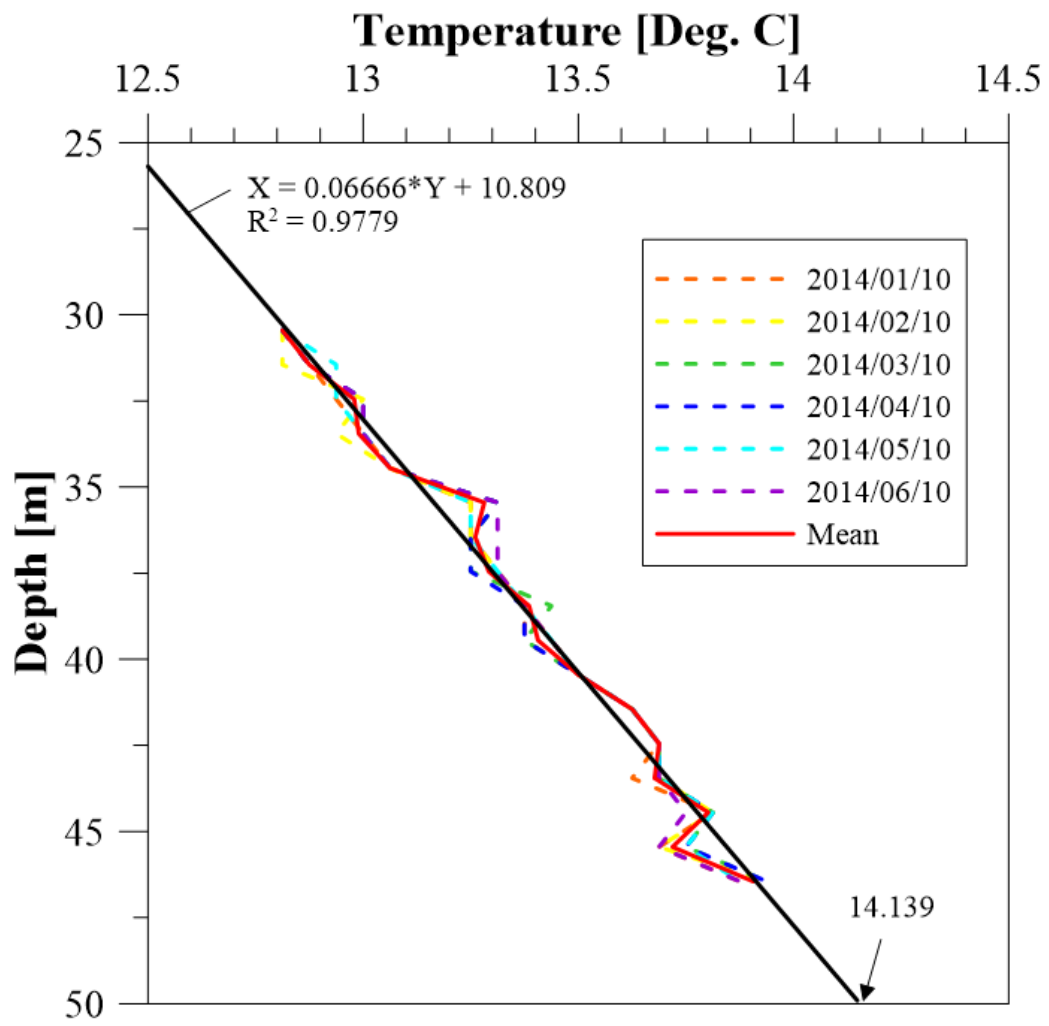


Figure 2.8. Subsurface temperature logs with depth measured at well YSO-1.

2.3.4. Effect of the aquifer thermal properties

To evaluate the impacts of the thermal properties, especially thermal dispersivity, on the subsurface thermal plume evolution associated with the GWHP system, a sensitivity analysis was performed. The range of parameters for the analysis is listed in Table 2.3. In general, it is desirable to locate the injection well downstream to minimize thermal interference if it is not intended to enhance the aquifer thermal storage. The injection well in this analysis was assumed to be upstream to analyze the influence of the parameters. The injected water temperature was set to be 5°C higher than the undisturbed groundwater temperature. The numerical simulations were performed for 30 d with constant pumping and injecting rates of 25 m³/d, which are close to those of the push–pull test.

2.3.5. Effect of injection and production rates

The thermal dispersion coefficient D is given by (de Marsily, 1986):

$$D = \frac{\lambda}{\rho c} + \beta \cdot \left| \frac{\rho_w c_w}{\rho c} \cdot q \right|, \quad (2.5)$$

where β [m] is the longitudinal or transverse thermal dispersivity, λ [W m⁻¹K⁻¹] is the bulk thermal conductivity, ρc and $\rho_w c_w$ [J m⁻³K⁻¹] are the volumetric heat capacity of the bulk volume and water, and q [m/s] is the specific discharge. As shown in equation (2.5), thermal dispersion is related to fluid velocity. Studies in the literature describe the increase of thermal dispersion with the increase of flow velocity (Anderson, 2005; de Marsily, 1986; Green et al., 1964; Hatch et al., 2006; Keery et al., 2007; Levec et al., 1985; Metzger et al., 2004; Rau et al., 2010; Rau et al., 2012; Testu et al., 2007; Vandenbohede et al., 2009; Vandenbohede et al., 2010).

Because GWHPs are flexible in terms of system size and have been applied to large buildings in recent years, injection and production rates can be increased. For example, Al-Zyoued et al. (2014) studied a geothermal utilization of groundwater for the cooling of four different buildings. In their study, each well has extraction and injection rates in the range of 100 to 200 m³/d. To estimate the effect of thermal dispersivity with a different fluid velocity, numerical simulations were performed with different injection and extraction rates ranging from 25 to 200 m³/d. Thermal dispersivity was changed from 0.4 to 1.2 m, as listed in Table 2.3.

Table 2.3. Range of thermal properties for sensitivity analysis.

Parameter	Symbol	Unit	Value
Thermal conductivity of the solid	λ^s	W m ⁻¹ K ⁻¹	1.9, 2.9, 3.9, 4.9
Volumetric heat capacity of the solid	$\rho^s C^s$	10 ⁶ J m ⁻³ K ⁻¹	1.7, 2.1, 2.5, 2.9
Longitudinal thermal dispersivity	β_L	m	0.4, 0.8, 1.2

2.4. Results and discussion

2.4.1. Aquifer thermal properties

Figure 2.9 shows the thermal breakthrough curves at different observation points after injecting warm water under various aquifer thermal properties. It is clear that the thermal properties of the aquifer have different influences on the thermal plume evolution. In this study, the arrival time of the thermal plume means the time when the groundwater temperature observed at each well reaches 12.7°C ($\Delta T = 0.1^{\circ}\text{C}$). Because the results from numerical simulations are discontinuous, the time series of groundwater temperature were interpolated using a cubic spline as an interpolant. The results are given in Table 2.4. Variations in the thermal conductivities of the aquifer did not affect the arrival time of the thermal plume, while the volumetric heat capacity (1.8 d) and the thermal dispersivity (0.48 d) of the aquifer were found to affect the arrival time. The arrival time is associated with the extent of the thermal plume. These changes in the arrival time correspond to the previous results (Lo Russo et al., 2012), indicating that the volumetric heat capacity and thermal dispersivity have an influence on the size of the thermally affected zone.

The simulation results show that the temperature change is most sensitive to variations in the thermal dispersivity (Figure 2.9). The thermal conductivity also affected the temperature change in the observation points, but the effect of this was relatively small, even though the possible range of thermal conductivity was included in this study (see Cha et al., 2007; Banks, 2012). Despite small changes based on the estimated value, the thermal dispersivity of the aquifer had a great influence on the temperature distribution as well as the extent of the plume. It is difficult to compare with the previous studies in terms of different hydrogeological and thermal characteristics. Because many of previous studies used the solute dispersivity or

relevant default values in their model, additional modeling was performed with the default values in FEFLOW[®]. The results confirmed that the effect of the thermal dispersivity on both temperature distribution and arrival time of thermal plume becomes greater (Figure 2.9c and Table 2.4). The experimental and measured thermal longitudinal dispersivity values reported in the literature have a wide range of 0.1 to 100 m (Stauffer et al., 2013). Therefore, to predict the environmental effects of GWHPs, it is necessary to estimate the site thermal dispersivity, such as the solute dispersivity, to predict solute transport.

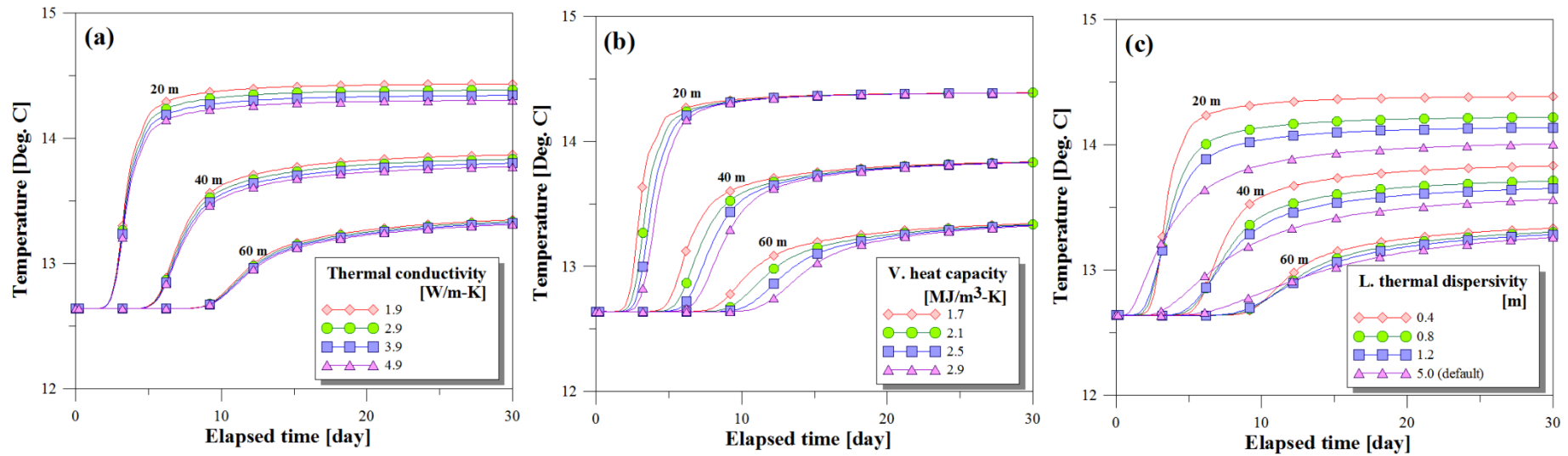


Figure 2.9. Thermal breakthrough curves at different observation points after injecting warm water under various values of (a) Thermal conductivity, (b) Volumetric heat capacity, and (c) Thermal dispersivity.

2.4.2. Injection and production rates

Previous studies have described the relationship between natural groundwater flow and thermal dispersivity (Anderson, 2005; de Marsily, 1986; Green et al., 1964; Hatch et al., 2006; Keery et al., 2007; Levec et al., 1985; Metzger et al., 2004; Rau et al., 2010; Rau et al., 2012a; Testu et al., 2007; Vandenbohede et al., 2009; Vandenbohede et al., 2010). In GWHP systems, however, natural groundwater flow is largely disturbed by the operation of injection and production wells. Figure 2.10a shows groundwater velocity distribution along the flow direction 15 m below the surface. To evaluate the effect of production and injection on the velocity field, the relative velocity discrepancy was defined as follows:

$$RVD = \frac{q - q_u}{q_u} \quad (2.6)$$

where q and q_u [m/d] are the Darcy velocity of disturbed and undisturbed groundwater. Even though natural groundwater flow in the study area is fast, relatively low injection and production rates of 25 m³/d have a great influence on groundwater flow, especially around the wells.

Figure 2.10b shows the groundwater velocity and the effect of dispersivity on groundwater temperature according to the increase in injection and production rates. As injection and production rates increase, the groundwater velocity increases proportionally. The effect of dispersivity on the subsurface heat transport is expressed as the peak temperature difference according to the variations in dispersivity:

$$\Delta T_{peak} = T_{0.4} - T_{1.2} \quad (2.7)$$

where $T_{0.4}$ and $T_{1.2}$ indicate the peak temperature at the pumping well under dispersivity of 0.4 and 1.2, respectively. Similarly to groundwater velocity, the temperature difference shows an

increasing trend. These results suggest that the dispersivity values have a greater influence on the temperature distribution related to GWHP systems with higher injection and production rates.

The thermal dispersion coefficient, as shown in equation (2.5), includes heat transport by conduction through both the matrix and the fluid as well as that by thermal dispersion. Because thermal dispersion is a function of groundwater flow velocity, the relative importance of both two terms on the right-hand side depends on the flow velocity. That is, the thermal dispersivity term is not significant at the low flow velocity because the effective diffusivity is relatively large in magnitude. However, as the flow velocity increases and exceeds a specific point, this term becomes significant (Rau et al., 2012a). From the hydrogeological and thermal conditions of the field site as listed in Table 2.1, two terms in equation (2.5) were calculated. The first term representing the effect of heat conduction is $\lambda/\rho C = 0.76 \times 10^{-6} \text{ m}^2/\text{s}$ and the second term representing the effect of thermal dispersion is $\beta \cdot q \cdot \rho_w C_w / \rho C = q \times 0.64 \text{ m}^2/\text{s}$. When the specific discharge (or Darcy velocity) is $1.19 \times 10^{-6} \text{ m/s}$, the effect of thermal dispersion becomes the same as that of heat conduction. Based upon the groundwater level and hydraulic gradient measured before the push–pull test, the specific discharge of the study area is $42.12 \times 10^{-6} \text{ m/s}$, which is faster than the aforementioned velocity of $1.19 \times 10^{-6} \text{ m/s}$. As the groundwater pumping and injection with the GWHP system will greatly increase the specific discharge, thermal dispersion in this site imposes a great importance for the heat transport process.

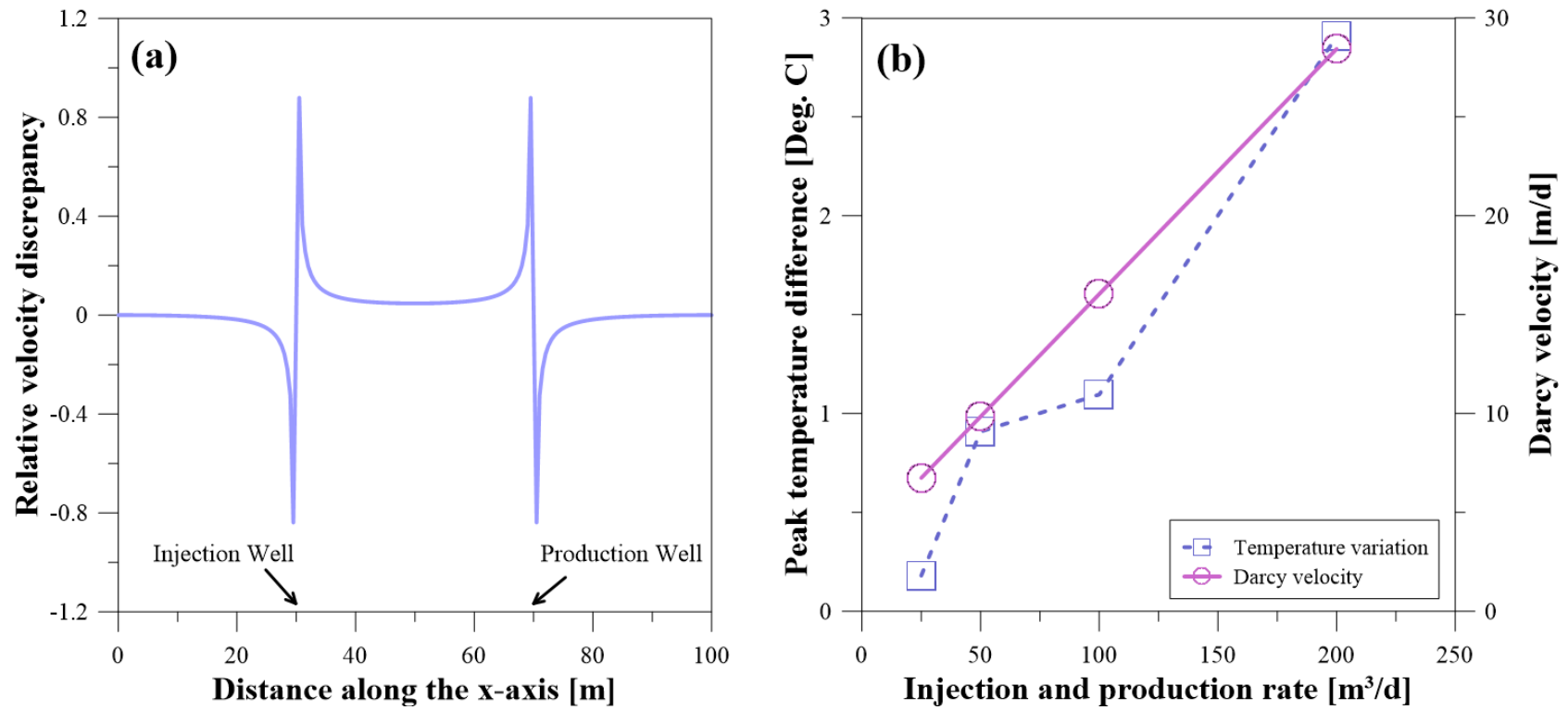


Figure 2.10. Effect of injection and production rates. (a) Relative velocity discrepancy along the flow direction (at a depth of 15 m) and (b) Variations of temperature and Darcy velocity according to injection/production rates.

Table 2.4. Arrival time with distance from the injection well showing the effect of the aquifer thermal properties.

Displacement [m]		Thermal conductivity of the solid λ^s [W m ⁻¹ K ⁻¹]				Δt [d]
		1.9	2.9	3.9	4.9	
t [d]	20 m	2.30	2.31	2.33	2.34	0.04
	40 m	5.42	5.46	5.50	5.53	0.11
	60 m	9.47	9.56	9.62	9.68	0.21
Δt [d]		7.17	7.25	7.29	7.34	
Displacement [m]		Volumetric heat capacity of the solid $\rho^s C^s$ [10 ⁶ J m ⁻³ K ⁻¹]				Δt [d]
		1.7	2.1	2.5	2.9	
t [d]	20 m	2.05	2.31	2.58	2.84	0.79
	40 m	4.84	5.46	6.06	6.64	1.80
	60 m	8.48	9.56	10.58	11.62	3.14
Δt [d]		6.43	7.25	8.00	8.78	
Displacement [m]		Longitudinal thermal dispersivity β_L [m]				Δt [d]
		0.4	0.8	1.2	5.0 (default)	
t [d]	20 m	2.31	2.10	1.93	1.15	0.38 (1.16)
	40 m	5.46	5.20	4.98	3.50	0.48 (1.96)
	60 m	9.56	9.43	9.23	7.30	0.33 (2.26)
Δt [d]		7.25	7.33	7.30	6.15	

Values in parentheses include the results from the default thermal dispersivity provided by FEFLOW®.

2.5. Conclusions

To estimate the site thermal dispersivity, the push–pull test using heat as a tracer was conducted in the alluvial aquifer of a shallow-depth geothermal field in Yangpyeong-gun, Gyeonggi-do, Korea. The measured data from the test were compared to the results of 3-D groundwater flow and heat transport simulations. From the best fit between the measured and computed temperature data, the site longitudinal thermal dispersivity was determined to be 0.4 m under a hydraulic gradient of 0.0095.

The thermal dispersion coefficient includes the effect by heat conduction as well as that by thermal dispersion. The relative importance of thermal dispersivity term depends on the flow velocity. Two terms in equation (2.5) were computed using the hydrogeological and thermal conditions of the study area. The results indicate that, in the alluvial aquifer of this study, thermal dispersivity has an important role in the heat transport process even under the natural groundwater flow.

Sensitivity analysis was also performed to evaluate the effect of aquifer thermal properties, especially thermal dispersivity, on the subsurface heat transport processes related to GWHP systems. The sensitivity analysis shows that the thermal dispersivity and volumetric heat capacity have a significant influence on the arrival time. These results are in agreement with the previous study, indicating that the volumetric heat capacity and thermal dispersivity affect the development of the thermally affected zone (Lo Russo et al., 2012). In particular, it is noteworthy that the thermal dispersivity had a great effect on the temperature distribution as well as the extent of the thermal plume, although the change in the thermal dispersivity was studied in a small range. A variety of recent studies on the applicability of GWHP systems, however, used the solute dispersivity or relevant

default values as the site thermal dispersivity in their numerical models without any field-based estimation. Longitudinal thermal dispersivity values reported in the literature indicate that the thermal dispersivity of aquifers can vary in wide ranges of 0.1 to 100 m (Stauffer et al., 2013). There is dissimilarity as well as similarity between the mechanism of heat and solute transport in saturated porous media (Rau et al., 2012a). Therefore, it will be necessary to estimate the site thermal dispersivity via field-based experiments for better prediction of the subsurface heat transport process and the estimation of the geothermal potential associated with GWHP systems.

Experimental studies reported in the literature have described an empirical relationship between flow velocity and thermal dispersion. In open-loop GWHP systems, however, the velocity itself is greatly modified because of the artificial injection and production of water. Although ambient groundwater flow in the study area is fast, even very low injection and production rates of 25 m³/d can have a great influence on the groundwater flow system, especially around the wells. As injection and production rates increase, the groundwater velocity increases proportionally and the effect of thermal dispersivity also increases. Considering the application of GWHP systems to large facilities, which requires high pumping and injection rates, the thermal dispersivity of the aquifer can become a more important factor in the design of GWHP systems.

An open-loop GWHP system is not always sustainable. There exist hydraulic and thermal risks threatening its sustainability. The phenomena called thermal feedback or thermal recycling can make the GWHP system unrenewable as reported in the case from Winnipeg, Canada (Ferguson, 2005). To minimize the environmental impacts and maximize the sustainability of the system, a thermogeological risk assessment have been

performed. Analytical approaches, not considering dispersion effects, have the possibility to underestimate the travel time of the thermal breakthrough (Banks, 2009). The consideration of the thermal dispersivity in the design of GWHP system will contribute to better prediction of such risks.

Chapter 3

Mechanical Thermal Dispersion as Aquifer Properties

This chapter is based on the publication:

Park, B. H., Joun, W. T., Lee, B. H., & Lee, K. K. (2015b). A study on significant parameters for efficient design of open-loop groundwater heat pump (GWHP) systems. *Journal of Soil and Groundwater Environment* 20(4), 41–50.

3.1. Introduction

Open-loop GWHP systems use groundwater as renewable and sustainable energy resources for the heating and cooling of buildings. Since GWHP systems directly pump/inject groundwater from/into an aquifer, their efficiency highly depends on the hydrogeological and thermal properties of the aquifer (Lo Russo et al., 2012; Park et al., 2015a). Recently, a variety of studies have been conducted to efficiently fulfill the energy needs for buildings while reducing the thermal risks of GWHP systems (Al-Zyoud et al., 2014; Beretta et al., 2014; Lo Russo et al., 2011; Nam & Ooka, 2010; Zhou et al., 2013). For example, Lo Russo et al. (2011) considered two storage tanks as alternative designs

for cooling demand of large university buildings in Turin, Italy, and their analysis showed that using storage systems can provide environmental benefits. Beretta et al. (2014), based on the similarity between solute and heat transport, evaluated different injection scenarios for sustainable geothermal heating in Canavese power stations, Italy. Most studies, however, have focused on the efficient and stable GWHP design under specific site conditions, and there is still a lack of knowledge about the role and importance of aquifer properties on the relevant flow and heat transport processes of GWHP systems.

Numerical modeling of subsurface flow and transport, which can ensure the long-term sustainability of GWHP systems, requires a wide range of input parameters representing the hydrogeological and thermal properties of aquifers. Field experiments for aquifer characterization, however, are affordable only for large-scale facilities because they are expensive in terms of time and cost. In this context, recent studies have developed and evaluated simplified models for thermal impact assessment of GWHP systems (see Casasso & Sethi, 2015; Pophillat et al., 2018). These simplified models can be helpful for initial impact assessments, small applications, and groundwater management, but they are valid only within assumed conditions (see Banks, 2009) and also need information on aquifer properties. Therefore, it is necessary to understand the effects of aquifer properties to clarify the coverage of the model and alleviate the burden of field experiments.

In this Chapter, mechanical thermal dispersion was evaluated in terms of aquifer properties for GWHP systems. The 3-D finite element model developed in Chapter 2 was modified, and the sensitivity analysis was performed to investigate the influences of aquifer properties on the heat transport processes in a saturated porous medium. Additional field data were obtained on air temperature, groundwater temperature, and

groundwater flow, and they were reflected on initial and boundary conditions of the numerical model. Four different conditions considering the changes in groundwater flow velocities and pumping/injection rates were also included in the analysis.

3.2. Numerical simulation for sensitivity analysis

3.2.1. Modifying the developed model

Numerical modeling of the groundwater flow and heat transfer was conducted on the basis of the finite element model developed in Chapter 2. The model domain was extended to 150 m in groundwater flow direction to minimize the effect of boundary conditions and to consider hydrodynamic parameters and pumping/injection rates in the sensitivity analysis. The hydraulic influence at the boundary was evaluated using drawdown as a criterion, and its maximum was calculated to be 42 mm at 50 m away from a pumping well by Cooper-Jacob method (Cooper & Jacob, 1946). The extended model domain has five wells at 25 m intervals, and its dimensions are 100 m × 150 m × 50 m (Figure 3.1). The spatial and temporal discretization of the modified model was performed using the determined values for grid size and time stepping (see Chapter 2). Table 2.2 shows the hydrodynamic and thermal parameters used for numerical simulations.

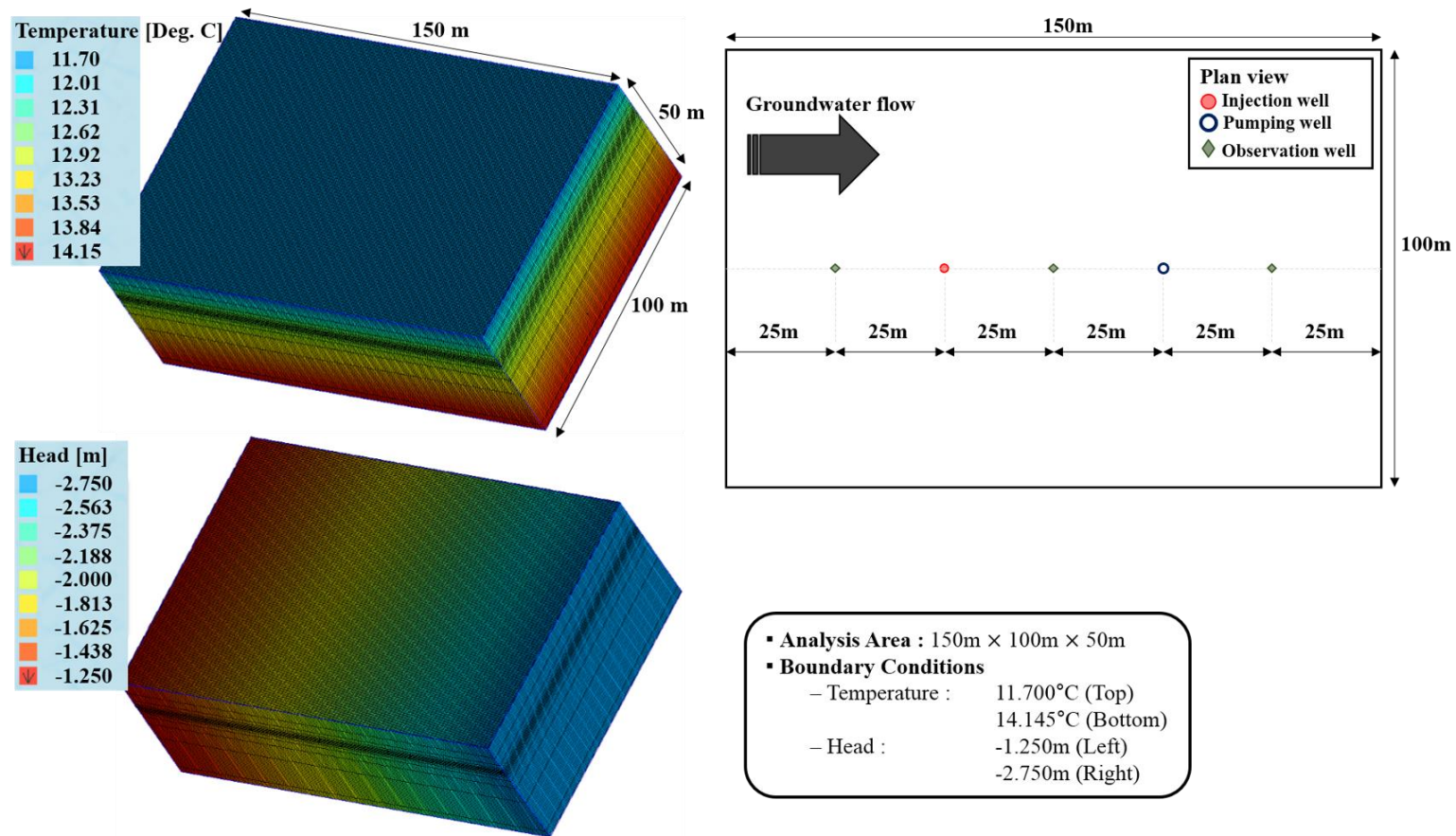


Figure 3.1. Finite element model domain extended to groundwater flow direction and its boundary conditions for hydraulic head and temperature.

3.2.2. Initial and boundary conditions

As it is explained in detail in Section 2.3.3 how to set the initial and boundary conditions for flow and transport modeling, this section focuses on additional data on groundwater flow, air temperature, and subsurface temperature. The study area has a very complicated groundwater flow pattern mainly due to the river stage fluctuation (see Figure 2.7). To quantify the seasonal variation in groundwater flow, a colloidal borescope system (AquaVISION, Geotech, USA), which can measure groundwater flow velocity and direction in real time, was installed at a depth of 15 m in well YSO-1 on August and November, 2014. The measured data indicate that, in summer with heavy rainfall, groundwater discharges at low flow velocities to the river, while surface water exfiltrates at high flow velocities to the aquifer in a dry winter season (Figure 3.2). To consider these seasonal changes in groundwater flow velocity, two different hydraulic gradients were used as a boundary condition in the numerical modeling.

The subsurface temperature distribution in Chapter 2 was computed using the air temperature at Yangpyeong weather station as a boundary condition. The study area, however, is located about 17 km away from the weather station. To confirm that air temperature data from the weather station can be representative, they were compared with the monitoring data at study area. As shown in Figure 3.3, the air temperature data at the weather station were in good agreement with the irregularly measured data in the study area, and thus they can represent the air temperature of the study area. Based on the data from the Yangpyeong weather station for 10 years from 2004 to 2013, the surface temperature was set at 11.7°C as the boundary condition on the top of the model (KMA, 2014).

The temperature logging system, which were installed at 1 m intervals from 2 to 45 m below land surface in well YSO-1, have measured the subsurface temperature every 30 minutes since January, 2014 (see Figure 3.4). The regression analysis was performed including the temperature logs for additional six months to estimate the temperature at the depth of 50 m. The estimated temperature is 14.145°C, comparable to the value evaluated from six-month data, and it was used as a boundary condition at the bottom of the numerical model.

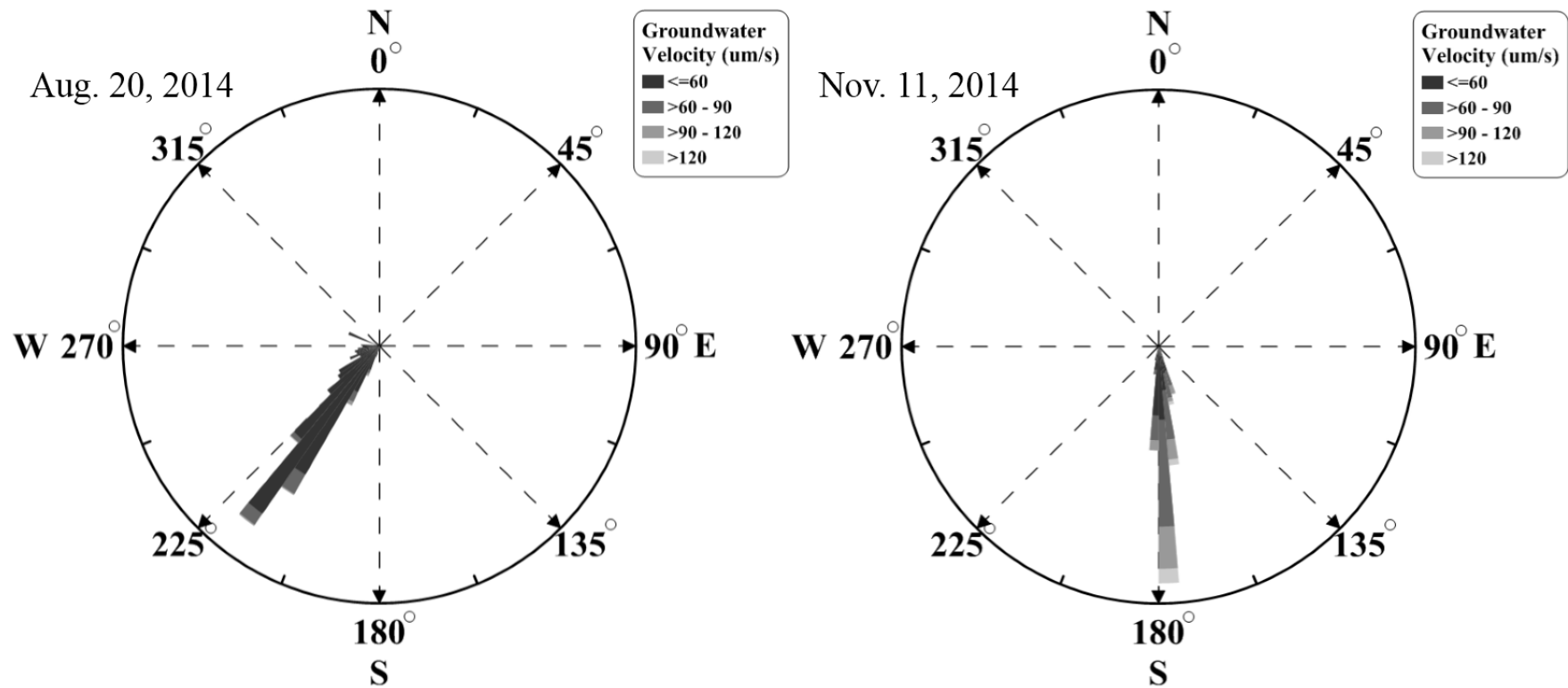


Figure 3.2. Direction and velocity of groundwater measured at well YSO-1 (15 m bls) on August and November, 2014. The flow velocities estimated from colloidal borescope indicate overestimated values due to well bore effects and preferential flow zones in the surrounding aquifer (see Kearnl, 1997). Hence, they need to be compensated by correction factors of 1–4 to represent the average linear or seepage velocities.

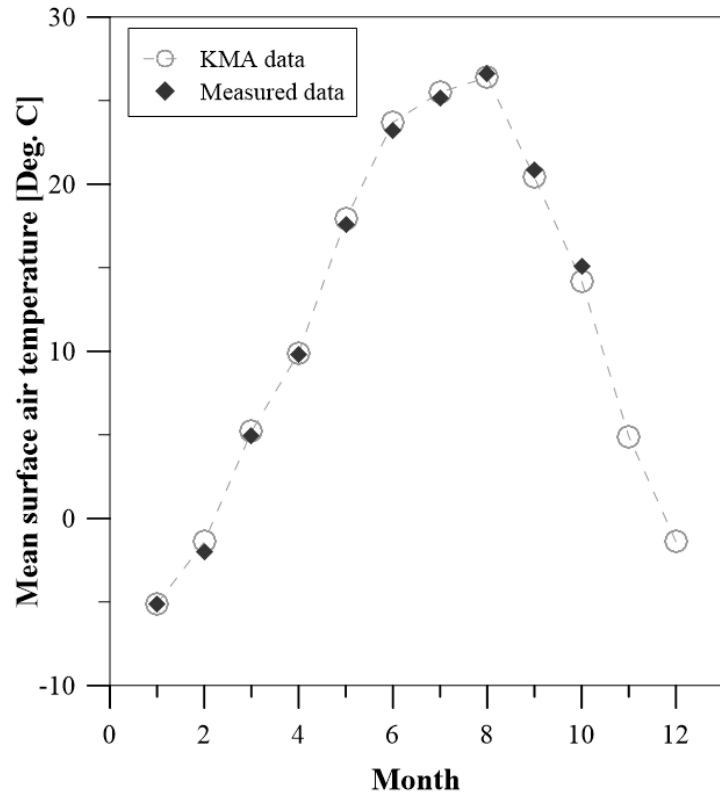


Figure 3.3. Monthly mean surface air temperature measured at the study area and weather station of Yangpyeong-gun.

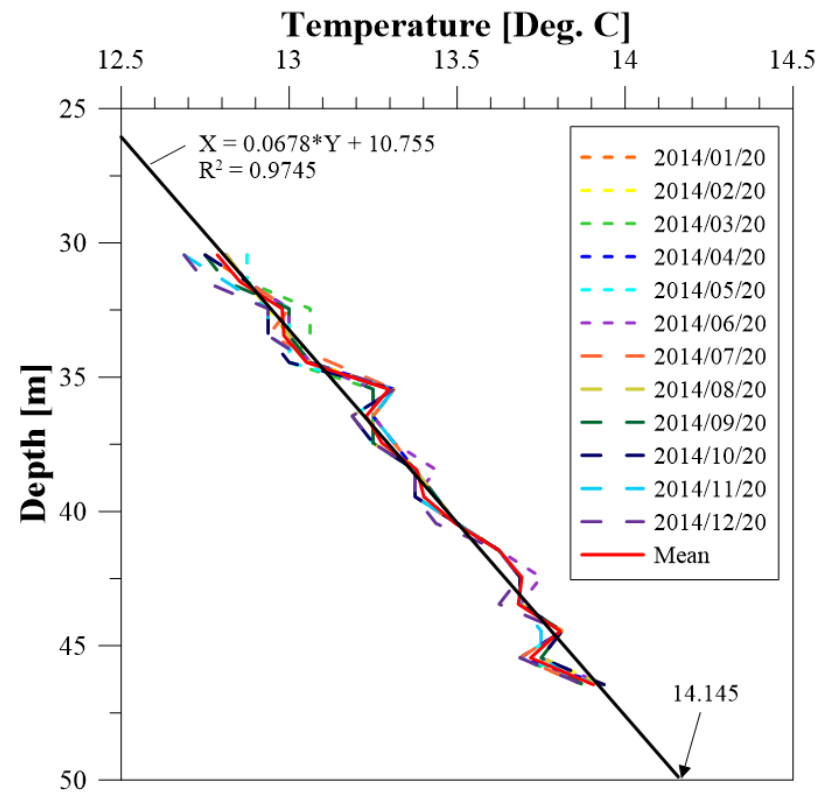


Figure 3.4. Subsurface temperature logs with depth measured at well YSO-1.

3.2.3. Sensitivity analysis

To evaluate the effects of the aquifer properties, groundwater flow, and pumping/injection rates on the subsurface thermal plume propagation, a sensitivity analysis was conducted. In the open-loop GWHP systems using more than two wells, it is desirable to install a pumping well upstream to avoid or reduce the thermal interferences between the pumping and injection wells. The injection well in this analysis was assumed to be upstream to analyze the influence of the parameters. The well separation between the pumping and injection wells is 50 m, and pumping/injection rates were assigned at the specific nodes of well locations in the gravel layer (see Section 2.3.3). The injected water temperature was assumed to be 22.7°C, which is 10°C higher than the undisturbed groundwater temperature.

The aquifer characteristics considered in the analysis are hydraulic conductivity (K), thermal dispersivity (β), volumetric heat capacity (ρc), thermal conductivity (λ), porosity (n), specific storage (S_s), and specific yield (S_y), and the sensitivity analysis can be divided into four cases according to hydraulic gradient (i) and pumping/injection rates (Q) (Table 3.1). Based upon the values listed in Table 2.2, the aquifer properties were changed by 20%. The longitudinal thermal dispersivity was reported to have a wide range of values in the literature (Molina-Giraldo et al., 2011; Stauffer et al., 2013). However, there is not enough data available, and this leads to the general use of default values in a numerical analysis software (see Lo Russo et al., 2011; Lo Russo et al., 2012). Therefore, additional analysis was performed with the default values ($\beta_L = 5$ m and $\beta_T = 0.5$ m) in FEFLOW® simulator. Because cooling load is concentrated on the period from July to August in Korea, the operation period for GWHP systems was set to be 60 days. In cases A and C

with relatively high groundwater flow velocity, however, the operation period was reduced to 30 days because temperatures at observation wells remained nearly unchanged after 30 days. After cases A and B were analyzed, some parameters (n , S_s , and S_y), which were estimated to be insignificant, were excluded in the subsequent analysis.

Table 3.1. Cases of the sensitivity analysis.

Cases	Parameter									
	ΔT	i	Q	K	β	$\rho^s c^s$	λ^s	n	S_s	S_y
A-1	10	0.01	25	$\pm 20\%$	-	-	-	-	-	-
A-2	10	0.01	25	-	$\pm 20\%$	-	-	-	-	-
A-3	10	0.01	25	-	-	$\pm 20\%$	-	-	-	-
A-4	10	0.01	25	-	-	-	$\pm 20\%$	-	-	-
A-5	10	0.01	25	-	-	-	-	$\pm 20\%$	-	-
A-6	10	0.01	25	-	-	-	-	-	$\pm 20\%$	-
A-7	10	0.01	25	-	-	-	-	-	-	$\pm 20\%$
B-1	10	0.005	25	$\pm 20\%$	-	-	-	-	-	-
B-2	10	0.005	25	-	$\pm 20\%$	-	-	-	-	-
B-3	10	0.005	25	-	-	$\pm 20\%$	-	-	-	-
B-4	10	0.005	25	-	-	-	$\pm 20\%$	-	-	-
B-5	10	0.005	25	-	-	-	-	$\pm 20\%$	-	-
B-6	10	0.005	25	-	-	-	-	-	$\pm 20\%$	-
B-7	10	0.005	25	-	-	-	-	-	-	$\pm 20\%$
C-1	10	0.01	50	$\pm 20\%$	-	-	-	-	-	-
C-2	10	0.01	50	-	$\pm 20\%$	-	-	-	-	-
C-3	10	0.01	50	-	-	$\pm 20\%$	-	-	-	-
C-4	10	0.01	50	-	-	-	$\pm 20\%$	-	-	-
D-1	10	0.005	50	$\pm 20\%$	-	-	-	-	-	-
D-2	10	0.005	50	-	$\pm 20\%$	-	-	-	-	-
D-3	10	0.005	50	-	-	$\pm 20\%$	-	-	-	-
D-4	10	0.005	50	-	-	-	$\pm 20\%$	-	-	-

3.3. Results

Figures 3.5–3.8 show the temperature variation observed in the pumping well when the parameters were changed by 20%, and Figure 3.9 shows the arrival time when the temperature change in the pumping well is detected or the thermal plume arrives at the pumping well. The criterion of temperature change is 12.8°C, which is 0.1°C higher than the undisturbed groundwater temperature. Because the results from numerical simulations are discontinuous, the time series data were interpolated using a cubic spline as an interpolant. The estimated change in final temperature and arrival time are listed in Tables 3.2 and 3.3 as well.

3.3.1. Hydrogeological and thermal characteristics of the aquifer

When the groundwater flow velocity is fast and the pumping/injection rate is low (case A), the temperature at pumping well does not increase much on the whole (Figure 3.5 and Table 3.2). The analysis results indicate that hydraulic conductivity of the aquifer (A-1) has the greatest impact on observed temperatures ($\Delta T = 0.479^\circ\text{C}$), and thermal dispersivity (A-2) also have an influence. Considering the default values in FEFLOW[®] simulator, thermal dispersivity has a greater impact on temperature.

3.3.2. Groundwater flow velocity

To investigate the effect of parameters under different groundwater flow velocities, cooling operations for 60 days were simulated with decreased hydraulic gradient of 0.005

(case B). The temperatures at the pumping well were observed to increase for all parameters with the decrease in groundwater flow velocity (Figure 3.6). Even in low flow velocity, hydraulic conductivity (B-1) and thermal dispersivity (B-2) play a crucial role on temperature change. The effect of thermal conductivity can vary depending on flow conditions (see Figures 3.5 and 3.6). It is negligible at fast flow velocity (A-4) but is important at slow flow velocity (B-4).

3.3.3. Injection/production rates

To examine the influence of injection/production rates on the sensitivity of parameters, cases C and D were performed with an increased rate of 50 m³/d. As injection/production rates increase, the temperature in the pumping well also increases (see Figures. 3.7 and 3.8). At high groundwater flow, hydraulic conductivity (C-1) and thermal dispersivity (C-2) are the most influential factors similarly to cases A and B. When the groundwater flow is relatively slow, the effect of hydraulic conductivity (D-1) decreases ($\Delta T = 0.439^{\circ}\text{C}$), while that of thermal dispersivity (D-2) increases with increasing injection/production rates ($\Delta T = 3.175^{\circ}\text{C}$). Regardless of groundwater flow velocity, the influence of thermal conductivity is negligible under high injection/production rates.

3.3.4 Arrival time

Figure 3.9 and Table 3.3 show that volumetric heat capacity does not affect the temperature in the pumping well, but have a great impact on the arrival time of thermal plume ($\Delta t = 1.43\text{--}2.53$ d). Porosity has a little influence on the arrival time, compared to

other parameters (K , β , and ρc). It was confirmed that hydraulic conductivity and thermal dispersivity have a significant effect on arrival time as well as temperature distribution.

Table 3.2. Final temperature at pumping well according to pre-set cases.

Case	A-1	A-2	A-3	A-4	A-5	A-6	A-7
T	-20%	14.880	14.654	14.598	14.625	14.589	14.595
[°C]	-	14.595	14.595	14.595	14.595	14.595	14.595
	+20%	14.400	14.546	14.591	14.567	14.601	14.595
	(default)		(14.197)				
ΔT		0.479	0.108	0.007	0.058	0.013	0.000
[°C]			(0.456)				
Case	B-1	B-2	B-3	B-4	B-5	B-6	B-7
T	-20%	16.832	16.413	16.215	16.323	16.181	16.206
[°C]	-	16.206	16.206	16.206	16.206	16.206	16.206
	+20%	15.666	16.042	16.197	15.529	16.232	16.206
	(default)		14.741				
ΔT		1.167	0.371	0.018	0.794	0.051	0.000
[°C]			(1.672)				
Case	C-1	C-2	C-3	C-4			
T	-20%	17.923	17.273	16.937			
[°C]	-	16.929	16.929	16.929			
	+20%	16.148	16.672	16.921			
	(default)		14.888				
ΔT		1.776	0.600	0.016			
[°C]			(2.385)	0.168			
Case	D-1	D-2	D-3	D-4			
T	-20%	19.183	19.322	19.074			
[°C]	-	19.059	19.059	19.059			
	+20%	18.743	18.825	19.044			
	(default)		16.147				
ΔT		0.439	0.497	0.030			
[°C]			(3.175)	0.226			

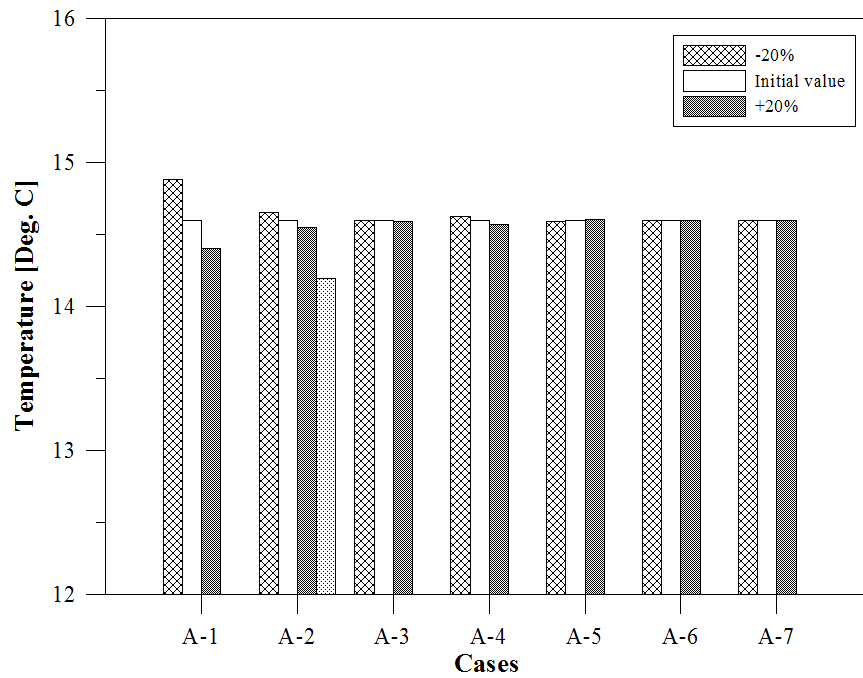


Figure 3.5. Groundwater temperature at pumping well according to case A ($i = 0.01$, $Q = 25 \text{ m}^3/\text{d}$).

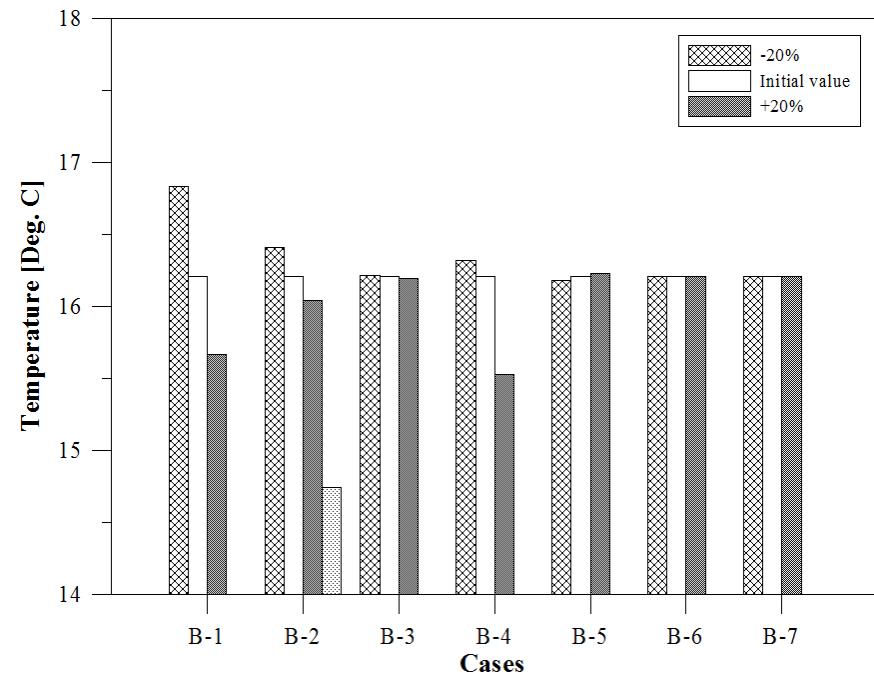


Figure 3.6. Groundwater temperature at pumping well according to case B ($i = 0.005$, $Q = 25 \text{ m}^3/\text{d}$).

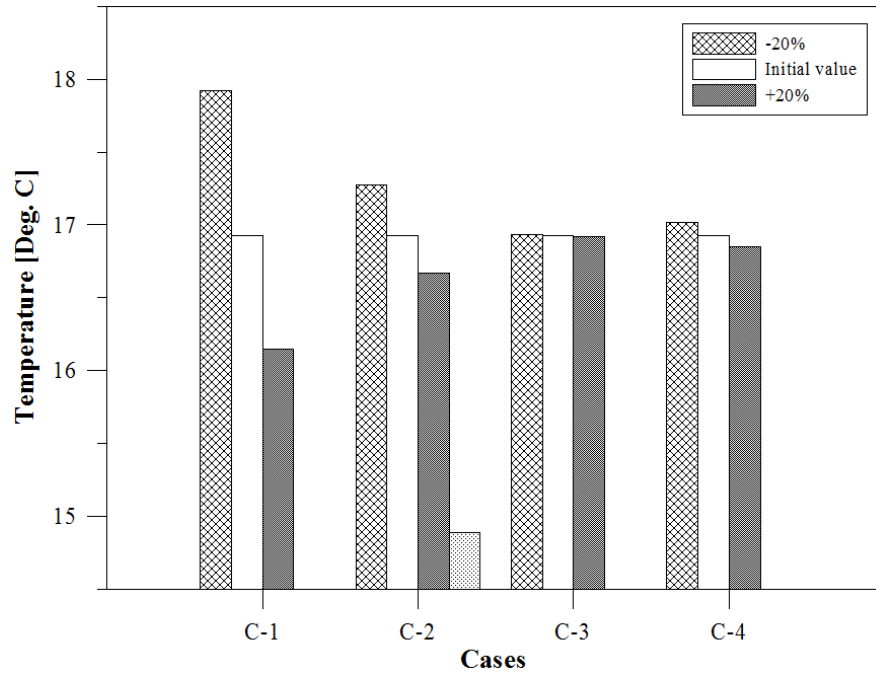


Figure 3.7. Groundwater temperature at pumping well according to case C ($i = 0.01$, $Q = 50 \text{ m}^3/\text{d}$).

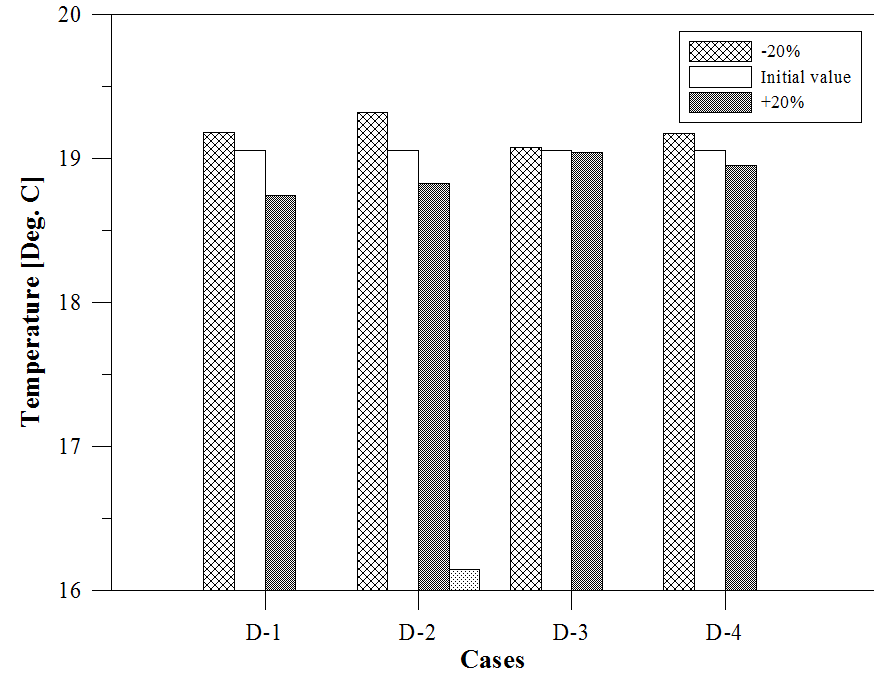


Figure 3.8. Groundwater temperature at pumping well according to case D ($i = 0.005$, $Q = 50 \text{ m}^3/\text{d}$).

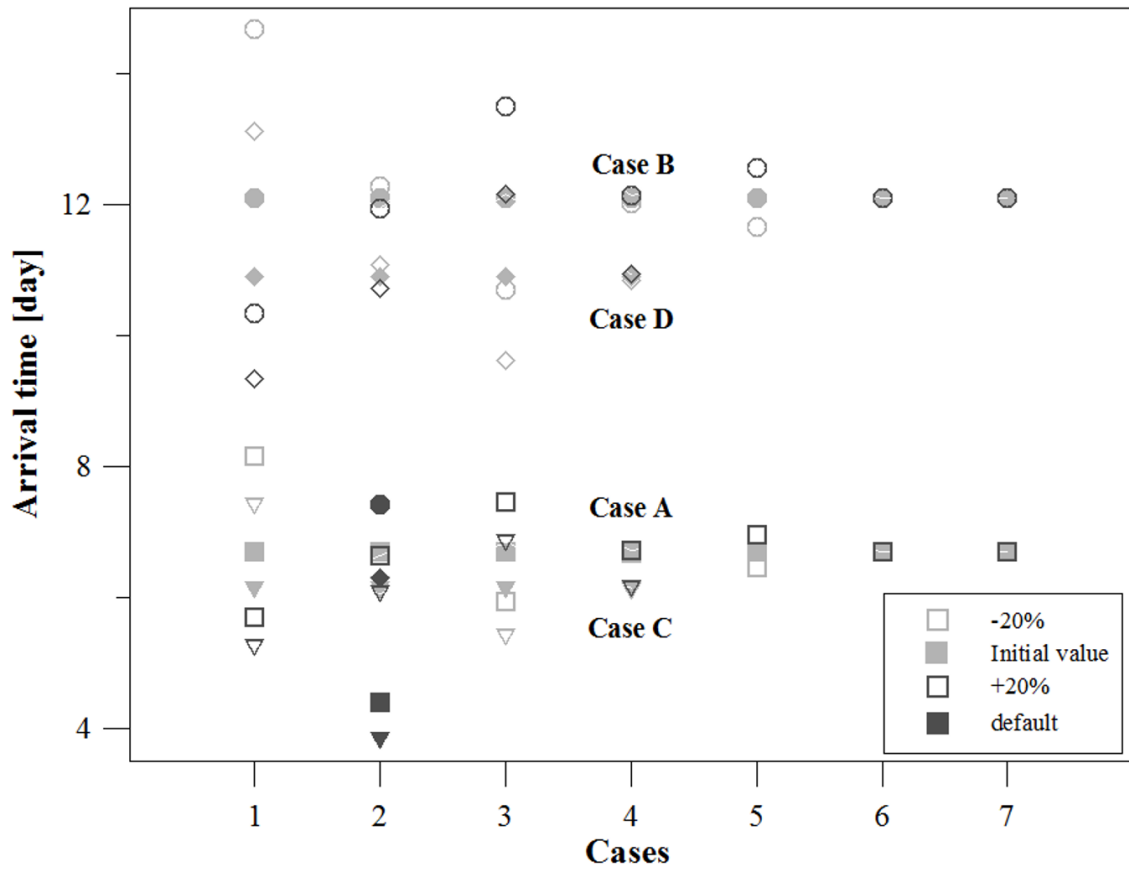


Figure 3.9. Arrival time of thermal plume observed at the pumping well according to four different cases (case A: square, case B: circle, case C: triangle, case D: diamond).

Table 3.3. Change in arrival time of thermal plume observed in the pumping well, depending on four different cases.

Case	A-1	A-2	A-3	A-4	A-5	A-6	A-7	
t	-20%	8.16	6.76	5.93	6.67	6.45	6.70	6.70
	-	6.70	6.70	6.70	6.70	6.70	6.70	6.70
	+20%	5.69	6.64	7.46	6.72	6.95	6.70	6.70
	(default)		(4.40)					
Δt	2.47	0.12 (2.36)	1.53	0.05	0.50	0.00	0.00	

Case	B-1	B-2	B-3	B-4	B-5	B-6	B-7	
t	-20%	14.68	12.28	10.70	12.02	11.65	12.10	12.10
	-	12.10	12.10	12.10	12.10	12.10	12.10	12.10
	+20%	10.34	11.94	13.50	12.14	12.55	12.10	12.10
	(default)		(7.42)					
Δt	4.34	0.34 (4.86)	2.80	0.12	0.90	0.00	0.00	

Case	C-1	C-2	C-3	C-4	
t	-20%	7.40	6.20	5.40	6.10
	-	6.12	6.12	6.12	6.12
	+20%	5.23	6.05	6.83	6.14
	(default)		(3.81)		
Δt	2.17	0.15 (2.39)	1.43	0.04	

Case	D-1	D-2	D-3	D-4	
t	-20%	13.12	11.08	9.62	10.83
	-	10.89	10.89	10.89	10.89
	+20%	9.34	10.71	12.15	10.94
	(default)		6.29		
Δt	3.78	0.37 (4.79)	2.53	0.11	

3.4. Discussion

Figures 3.5–3.9 show that hydraulic conductivity and hydraulic gradient have a great influence on both the temperature observed in the pumping well and the arrival time of thermal plume. This result is consistent with the previous studies indicating that hydrodynamic parameters (Lo Russo et al., 2012) or groundwater flow conditions (Nam & Ooka, 2010; Zhou et al., 2013) are of great importance in designing GWHP systems. Because hydraulic conductivity has a wide range of values even in the same kind of porous media (Freeze & Cherry, 1979), it is required to pay close attention when performing hydraulic tests such as pumping test and analyzing them.

Although thermal dispersivity is known to have a wide range of values from 0.1 to 100 m (Stauffer et al., 2013), there is still a lack of available data based on field experiments (Piga et al., 2017), leading to the general use of default values in numerical simulators. The results of this work, however, indicate that thermal dispersivity plays a significant role on thermal plume propagation even at low groundwater flow velocity (see Figures 3.6 and 3.8). This supports the previous result that, in the increased flow velocity by pumping/injection, thermal dispersion can have a greater impact on the subsurface heat transport (Section 2.4.2; also see Park et al., 2015a). Hence, it is necessary to estimate the site thermal dispersivity through field-based experiments.

Thermal conductivity of the aquifer plays a significant role on the efficiency of close-loop systems (Casasso & Sethi, 2014; Kim et al., 2008), but its effect on thermal plume may be negligible in GWHP systems (Lo Russo et al., 2012). The effect of thermal conductivity can be marginal if the groundwater flow velocity is fast or the pumping/injection rates are high (Figures 3.5 and 3.7–3.9). For large-scale systems where

GWHP systems are advantageous, the influence of thermal conductivity can be neglected regardless of groundwater flow condition (Figures 3.7 and 3.8). The sensitivity analysis results indicate that volumetric heat capacity has little effect on the observed temperature but has a great impact on the arrival time of thermal plume. This is in good agreement with the previous study showing the effect of volumetric heat capacity on the extension of thermal affected zone (Lo Russo et al., 2012). These results can be explained by the fact that the propagation of thermal plumes in porous media depends on thermal front velocity (see Rau et al., 2012a; Piga et al., 2017) instead of seepage velocity. As porosity also constitutes of thermal front velocity, it has an influence on the arrival time of thermal plumes but its effect is small compared to other properties (K , β , and ρc). Since specific storage and specific yield have a negligible influence on thermal plumes developing from GWHP systems, it will be reasonable to refer to the values in the literature (Anderson & Woessner, 1992; Johnson, 1967).

3.5. Conclusions

The prediction of thermal plumes developing from GWHP systems is a matter of great concern in that they can have a negative impact on the system efficiency and the surrounding environment. Aquifer properties are well known to have an influence on designing GWHP systems, but there is not much information on their role because most studies have focused on the sustainable design at site-specific conditions. In this chapter, the finite element model was modified to investigate the sensitivity of seven aquifer properties under four different conditions, based on the estimated values in Chapter 2 and additional monitoring data.

The sensitivity analysis confirms the previous finding that hydrodynamic parameters (i.e. hydraulic conductivity, hydraulic gradient, and porosity) play a crucial role on thermal plume propagation, and reveals that the propagation of thermal plumes depends on thermal front velocity instead of seepage velocity. The results also indicate that aquifer properties composing mechanical thermal dispersion are significant on predicting thermal plumes of GWHP systems because groundwater pumping/injection increase the flow velocity around wells. Therefore, it will be more desirable to concentrate on field experiments to estimate such parameters. This work, however, has limitations that the sensitivity analysis was based on the site-specific values of the study area and the short-term simulation results. Further research will be needed to investigate the effect of extensive aquifer properties on the long-term sustainability of GWHP systems.

Chapter 4

Thermal Dispersion Under Forced Flow Field by Injection

This chapter is based on the publication:

Park, B. H., Lee, B. H., and Lee, K. K. (2018). Experimental investigation of the thermal dispersion coefficient under forced groundwater flow for designing an optimal groundwater heat pump (GWHP) system. *Journal of hydrology* 562, 385–396.

4.1. Introduction

For large-size heating and cooling plants, the GWHP systems are more economical and require a smaller installation area compared to closed-loop GSHP systems. Due to direct use of groundwater, however, their performance is highly dependent on the hydrogeological and thermal properties of aquifer (Lo Russo et al., 2012; Park et al., 2015a; Park et al., 2015b; Piga et al., 2017), which makes it challenging to design an efficient and stable GWHP system. In recent years, various studies have been conducted to enhance the efficiency of GWHP systems in consideration of aquifer properties, but

most of them have focused on the effect of groundwater flow conditions on heat transport in porous media (Gao et al., 2013; Lo Russo et al., 2011; Nam & Ooka, 2010; Zhou et al., 2013). Moreover, unlike the solute dispersivity estimated by a solute tracer test, the thermal dispersivity has often been neglected or underestimated in applications by using solute dispersivity values or default values of numerical models without any field-based evaluation.

However, some studies performed in the field of shallow-depth geothermal applications have reported the influence of thermal dispersion on the relevant heat transport process. For example, Sauty et al. (1982) analyzed the experiments on aquifer thermal energy storage (ATES) with mathematical models and found that the thermal dispersion plays an important role in estimating the energy recovery ratio. Their findings were also observed in the numerical studies on ATES experiments (Dwyer & Eckstein, 1987; Xue et al., 1990). Lo Russo & Civita (2009) and Park et al. (2015a) reported that the thermal plume development from the injection well to the pumping well, degrading the performance of GWHP systems, can depend considerably on thermal properties, especially thermal dispersivity. Most recently, Alcaraz et al. (2016) used a GIS-based methodology to estimate shallow geothermal resources at a regional scale. Analysis results for the geothermal potential and the associated environmental impacts indicate that considering dispersion effects is significant for obtaining reliable results. Therefore, it is needed to examine the importance of thermal dispersion on heat transport processes.

For the last few decades, laboratory experiments have been conducted to investigate thermal dispersion behavior in porous media under natural groundwater flow conditions (Green et al., 1964; Levec & Carbonell, 1985; Metzger et al., 2004; Rau et al., 2012a;

Rau et al., 2014). The experimental results indicated that the thermal dispersion increases with flow velocities, but there was a controversy over the relationship between them. One group of researchers suggested a linear relationship (Anderson, 2005; de Marsily, 1986; Vandenbohede et al., 2009; Yagi et al., 1960), while others proposed various nonlinear forms to describe the relationship (Green et al., 1964; Lu et al., 2009; Metzger et al., 2004; Rau et al., 2012a). Green et al. (1964) first suggested a power law relationship, which was verified later by Metzger et al. (2004) with the same coefficients, and by Lu et al. (2009) with different coefficients. Such disagreements were clarified by Rau et al. (2012a), who showed that the thermal dispersion can be described by a square law, and the importance within natural groundwater flow velocities ($Re < 2.5$).

On the field scale, thermal dispersion is known to occur due to the heterogeneity of aquifer properties (de Marsily, 1986; Ferguson, 2007; Hidalgo et al., 2009; Sauty et al., 1982). This can be the reason why the macroscopic thermal dispersivity has a wide range of values in the literature (see Molina-Giraldo et al., 2011; Stauffer et al., 2013). Sauty et al. (1982) inferred from the experimental results that the macrodispersivity increases with the travel distance and stabilizes after reaching a certain scale of heterogeneity. Their findings correspond with the recent studies on the scaling behavior of macrodispersivity, indicating that the macrodispersivity increases with travel distance to their asymptotic values (Chang & Yeh, 2012; Zech et al., 2015). Therefore, the thermal dispersivity on the field scale can be higher by several orders of magnitude than on the laboratory scale.

In addition to the heterogeneity of aquifer properties, pumping and injection in field applications can further increase the magnitude of thermal dispersion. Because the GWHP system generally utilizes large volumes of groundwater as a heat source (or heat sink), it

can greatly disturb the natural flow field. Under such conditions, the influence of the thermal dispersion on the relevant transport processes can be increased. However, most studies on thermal dispersion have focused on the natural groundwater flow conditions (Green et al., 1964; Levec & Carbonell, 1985; Metzger et al., 2004; Rau et al., 2012a; Rau et al., 2014). In a few studies, water injection at different temperatures were conducted; however, there was too high a contrast in temperature to neglect the change in density and viscosity of water (see Kim et al., 2005; Saeid et al., 2014).

In this context, the laboratory-scale experimental system was designed to control flow and temperature boundary conditions, and investigate the thermal dispersion behavior in forced flow by water injection. The developed system will help to overcome the limitations of the study area in Chapters 2 and 3 that field experiments are subject to the complicated groundwater flow and temperature distributions which fluctuate spatiotemporally by natural and anthropogenic factors (Kaown et al., 2018; Lee et al., 2019). Under the controlled flow and transport conditions, heat tracer tests using two different heat sources were performed with Darcy velocities of 1.94 to 40.38 m/d. First of all, tracer tests using a resistor as a heat source were conducted with/without background flow and analyzed by analytical models to evaluate the thermal properties of a saturated porous medium. Then, using injected water as a heat source, tracer tests were performed under the same flow conditions as the resistor test and analyzed by a numerical model to examine the effect of injected water on the flow fields, thermal dispersion coefficients, and relevant heat transport processes. This chapter also analyzes the impacts of injection on a macroscale through a field-based model and discusses their meanings in field applications.

4.2. Laboratory experimental system

4.2.1. Experimental preparation

A laboratory experimental system for thermal tracer tests were designed to investigate the influence of water injection on flow field, thermal dispersion, and heat transport in fully-saturated porous media. The experimental system is composed of an acrylic glass tank, heat sources, and a data acquisition (DAQ) system (Figure 4.1). The outer dimensions of the rectangular tank are 1.3 m \times 0.6 m \times 0.8 m ($L \times W \times H$), and the thickness of the wall is 15 mm (Figure 4.2). The size was determined by simulating heat transport experiments through finite element numerical model to predict the thermal plume propagation. The simulation results were also used as the basis for sensor locating and duration for each experiment.

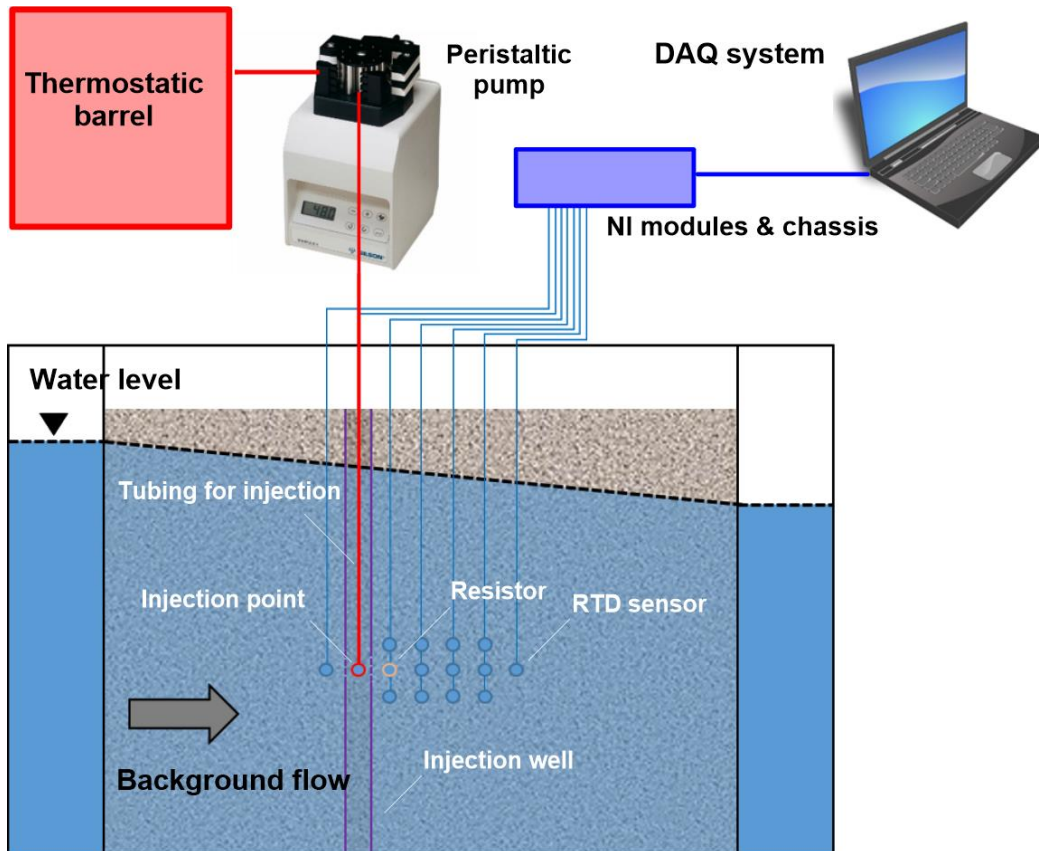


Figure 4.1. Schematic diagram of a laboratory experimental system for heat transport experiments in porous media. It consists of a rectangular acrylic glass tank, heat sources, and a DAQ system.

The tank is divided into three parts (Figure 4.2a). The middle chamber is 1 m in length and filled with a saturated sand as a porous medium. To prevent the rectangular tank from being damaged by the pressure of saturated sand, aluminum frames (DNF 3030, Dongjin, South Korea) were installed at 9 cm intervals in the vertical direction (Figure 4.2b). The two chambers on the side are 0.13 m long and operate as constant hydraulic head tanks. By adjusting water levels in the side chambers and thus hydraulic gradients between them, background water flow velocities passing through the porous media can be changed. These chambers are separated by 1.5 cm thick acrylic plates with many holes, which allow water to flow uniformly from high hydraulic head chamber to low hydraulic head chamber. Fine wire meshes were installed on the plates inside the middle chamber to prevent sand particles from entering the constant head tanks through the small holes (Figure 4.2c). After finishing the experimental setup, the sand tank was thermally insulated with multiple layers of insulation sheet (4 mm thickness) having sealed air bubbles in them.

4.2.2. Heat sources

Two different heat sources—a resistor and injected warm water—were used as tracers in the heat transport experiments. A small wire-wound resistor (7 mm in diameter, resistance of 47 Ω , and power rating of 5 W) was waterproofed with Teflon tape, mounted on an acrylic tube (8 mm in diameter and 0.7 m in height), and installed at a height of 0.3 m (see Figure 4.1). The laboratory DC power supply (AC input: 220 V, DC output: 0–30 V) applies a constant voltage to the resistor, enabling it to act as a constant heat source.



Figure 4.2. Illustration of an acrylic glass tank with (a) Outer dimensions of 1.3 m × 0.6 m × 0.8 m, supported by (b) Aluminum frames to disperse the pressure of saturated sands, and having (c) Fine meshes attached to prevent the infiltration of sand grains.

As shown in Figure 4.1, the peristaltic pump (Minipuls 3, Gilson, USA) transfers the warm water of the thermostatic barrel through the PVC tubing to the injection well with an inner diameter of 14 mm and a height of 0.7 m. The well has the screened section ranging from 0.29 to 0.31 m in height, which allows the injected water to spread radially from the injection point at a height of 0.3 m. The screened section was wrapped in a fine nylon mesh to prevent sand particles from penetrating into the injection well.

The heat flow rate (Q_h) from the injected water was determined using Q_h [W] = Q_w [ml/s] $\times \rho_w c_w$ [J ml⁻¹K⁻¹] $\times \Delta T$ [K]. Prior to the heat tracer test, a pretest was performed to determine the injection rate (Q_w) and temperature increment (ΔT). In the peristaltic pump, the pumping/injection rate depends on the RPM of the pump. When the RPM of the pump is low, the pumping/injection become discontinuous. It was examined if pumping is continuous while changing the RPM of the pump, and then three RPMs (12, 18, and 24) were chosen for the injection tests.

Several critical temperatures have been proposed to ignore the effects of density and viscosity in the literature (see Leaf et al., 2012; Ma & Zheng, 2010; Ma et al., 2012; Rau et al., 2012a). As an example, Ma & Zheng (2010) suggested the temperature difference of 15°C under which the effects of density and viscosity may be neglected for greater computational efficiency without any significant loss of accuracy. Ma et al. (2012), however, observed that the density-driven heat transport occurred even at the temperature difference of 8°C through the field experiment and numerical simulations. Leaf et al. (2012) used 10°C as the threshold for heated water to visualize complex borehole flow patterns. Rau et al. (2012a) determined 3°C as the threshold temperature to avoid the free convection generated by density differences in their experiments. In this study, the

temperature difference between background water and injected water was kept below 5°C to avoid free convection.

4.2.3. Data acquisition (DAQ) system

The DAQ system consists of temperature sensors (Pt100, Hayashi Denko, Japan), analog input modules (NI-9217, National Instruments, USA), compact DAQ chassis (cDAQ-9178, National Instruments, USA), and DAQ software (DAQmx and LabVIEW 2009). The temperature was measured by resistance temperature detectors (RTDs) in that they are more accurate and stable than thermocouples and thermistors. A thin-film type platinum RTD (1/3DIN class) was selected for heat transport experiments due to its highly linear response to temperature change and its small size. In this study, three-wire RTDs were used to detect temperature change because it can compensate for errors caused by lead wire resistance. A RTD element was connected to extension lead wires in a protective sheath of 3.2 mm in diameter and 2 cm in length. A total of 32 RTD sensors were installed to measure the temperature of a porous medium, ambient air, water in the thermostatic, and background water (see Figure 4.3). RTD sensors were mounted on acrylic tubes with a diameter of 8 mm, and arranged to monitor thermal plumes developing from the injection well.

After the experimental setup, the sensors' lead wires were collected and fixed to the top of the rectangular tank. Their terminals were connected to the NI modules for data conditioning and analog-to-digital switching, and were mounted on the eight slot chassis that controls timing, synchronization, and data transfer between the modules and a laptop computer. These DAQ hardware was controlled to sample and log the temperature every

0.1 s in the DAQ software consisting of a hardware driver (NI DAQmx) and a graphical programming environment (LabVIEW 2009).

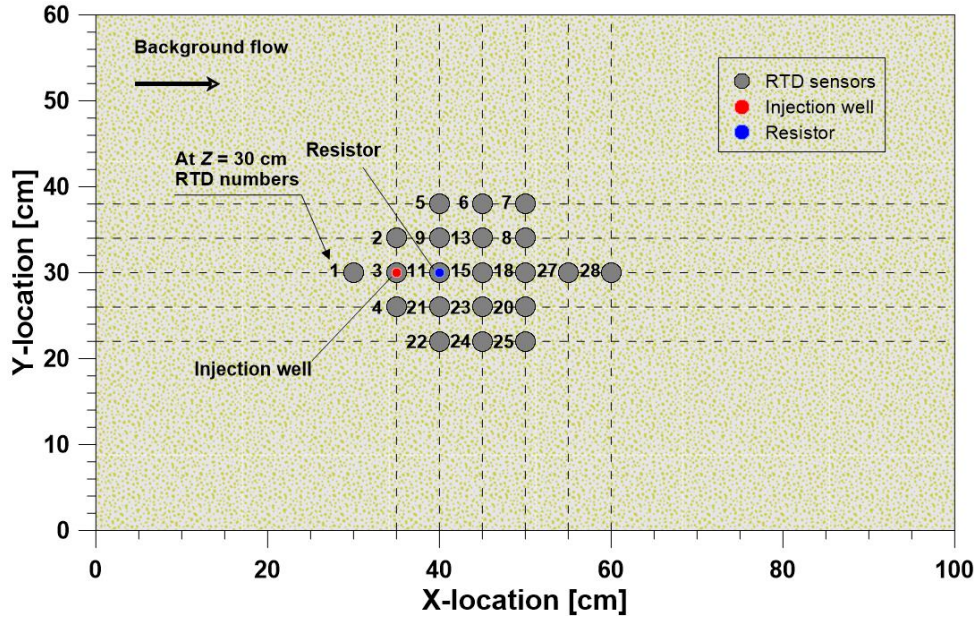


Figure 4.3. Horizontal location of RTD sensors and heat sources at a height of 30 cm.

4.2.4. Physical properties of porous media

The physical properties of porous media are significant because they are the basis for the analytical and numerical modeling. Therefore, they were estimated by repeated measurements and their relative uncertainties were represented as a percentage in parentheses. The uncertainty analysis is presented in Appendix A.

Before the middle chamber was filled with sands (DRY-SAND, Joomoonjin Silica Sand, South Korea), the grain size analysis was conducted using a set of sieves to confirm the average diameter and the uniformity of Joomoonjin #3 SAND (S3), #4 SAND (S4),

and #5 SAND (S5). Three samples were initially analyzed to identify the distribution of the sand particles and determine the appropriate sieves for the analysis, and then the grain size distribution was evaluated for 45 samples of three different sands (Figure 4.4). The mean grain size (d_{50}) was estimated to be 1.28 mm (0.4%) for sand S3, 0.76 mm (1.3%) for sand S4, and 0.52 mm (0.5%) for sand S5, which are within the range of coarse sand (Friedman & Sanders, 1978) but smaller than those used in previous studies (see Metzger et al., 2004; Rau et al., 2012a). The uniformity value (U) is 1.36 (0.5%), 1.50 (1.7%), and 1.41 (0.8%) for sands S3, S4 and S5, indicating very well sorted materials. Laboratory XRD analyses of sand samples were also conducted to quantify the proportion of different minerals present, and the results indicated a quartz content of 75.7%, 75.6%, and 68.3% for sands S3, S4 and S5. In addition, constant-head permeability tests were repeated 54 times to estimate the hydraulic conductivity of the saturated porous media. The average hydraulic conductivity values were estimated to be 2.34×10^{-3} m/s (2.5%), 1.70×10^{-3} m/s (2.7%), and 1.31×10^{-3} m/s (1.0%) for sands S3, S4, and S5.

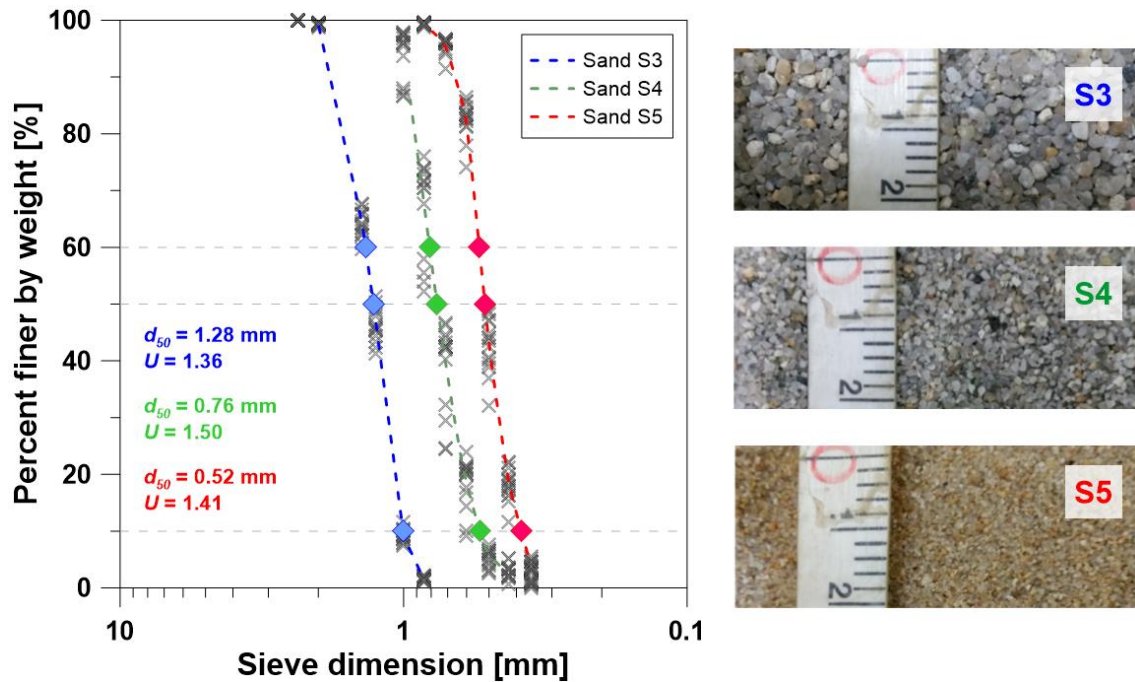


Figure 4.4. The grain size distributions and images of sand grains for sands S3, S4, and S5.

4.2.5. Temperature calibration

Although RTD sensors are known to have a highly linear response to temperature change, there is some nonlinearity between resistance and temperature. To compensate for this nonlinear relationship, another experiments were performed twice right before starting the experimental setup. A total of 32 RTD sensors for each experiment were placed at the center of the temperature control barrel with Levelogger[®] Edge (M3001, Solinst, Canada) which has the accuracy of $\pm 0.05^{\circ}\text{C}$ and the resolution of 0.003°C , and then their resistances were measured at various background temperatures of 9 to 40°C (Figure 4.5a). A regression method was applied to the relations between resistance and temperature based on the Callendar–Van Dusen equation defined as:

$$R(T) = R_0(1 + AT + BT^2), \text{ for } T > 0 \quad (4.1)$$

where R_0 is the resistance of 100Ω at 0°C (Pt100), A and B are the calibration coefficients for RTD sensors. From the regression analysis, the coefficients for 64 RTD sensors were determined with $R^2 > 0.9998$ (see Figure 4.5b), and are listed in Tables 4.1 and 4.2. The temperatures for RTD sensors were calibrated by substituting the estimated coefficients into the solution of equation (4.1) given below:

$$T(R) = \frac{-R_0A + \sqrt{R_0^2A^2 - 4BR_0(R_0 - R)}}{2BR_0} \quad (4.2)$$

As RTD sensors are also resistors, they can generate thermal energy and thus affect the temperature measurement. This self-heating effect can be expressed as follows:

$$\Delta T = \frac{P}{EK} \quad (4.3)$$

where ΔT [K] represents the self-heating effect and EK [mW/K] the self-heating coefficient. P [mW] is the electrical power input to RTD sensor given as:

$$P = \frac{I^2R}{1000} \quad (4.4)$$

where I [mA] is the excitation current. As $I = 1 \text{ mA}$, $R = 100 \Omega$, and $EK = 12 \text{ mW/K}$ for still water, ΔT is less than 0.01 K . Hence, the self-heating effect of RTD sensors are negligible in this study.

Table 4.1. Calibration coefficients of 32 RTD sensors used for heat transport experiments with sand S3 in Chapter 4.

Sensor	Coefficient A [$\times 10^{-3}$]	Coefficient B [$\times 10^{-7}$]	Quality of fitness (R^2)	Range [$^{\circ}\text{C}$]
RTD1	3.91360	-7.0312120	0.99989	9-39
RTD2	3.92900	-9.2305860	0.99985	9-39
RTD3	3.93320	-1.0492490	0.99985	9-39
RTD4	3.93420	-1.0653400	0.99987	9-39
RTD5	3.90420	-3.3664400	0.99986	9-39
RTD6	3.92810	-8.0880700	0.99985	9-39
RTD7	3.89120	1.6525720	0.99981	9-39
RTD8	3.89310	-8.6331400	0.99984	9-39
RTD9	3.91270	-6.3923780	0.99986	9-39
RTD10	3.90450	-2.8756510	0.99985	9-39
RTD11	3.92620	-6.3192690	0.99984	9-39
RTD12	3.91490	-2.1259100	0.99981	9-39
RTD13	3.91300	-3.9333190	0.99983	9-39
RTD14	3.90930	-4.5993740	0.99987	9-39
RTD15	3.91110	-3.2136160	0.99983	9-39
RTD16	3.91920	-5.6995200	0.99984	9-39
RTD17	3.91560	-3.7822650	0.99983	9-39
RTD18	3.91050	-2.3196450	0.99983	9-39
RTD19	3.90730	-2.2129000	0.99980	9-39
RTD20	3.93280	-9.4864470	0.99986	9-39
RTD21	3.99450	-2.8878490	0.99998	9-39
RTD22	3.99780	-2.7557570	0.99998	9-39
RTD23	4.00840	-3.0192710	0.99997	9-39
RTD24	4.00910	2.9654510	0.99996	9-39
RTD25	3.92960	-1.0088370	0.99985	9-39
RTD26	3.93340	-8.2533900	0.99985	9-39
RTD27	3.92300	-5.6262610	0.99983	9-39
RTD28	3.94940	-1.3636360	0.99988	9-39
RTD29	3.96440	-1.8362400	0.99988	9-39
RTD30	3.91440	-5.1949420	0.99988	9-39
RTD31	3.90720	-4.9461000	0.99989	9-39
RTD32	3.92300	-8.8474470	0.99988	9-39

Table 4.2. Calibration coefficients of 32 RTD sensors used for heat transport experiments with sands S4 and S5 in Chapter 5.

Sensor	Coefficient A [$\times 10^{-3}$]	Coefficient B [$\times 10^{-7}$]	Quality of fitness (R^2)	Range [$^{\circ}\text{C}$]
RTD1	3.88800	1.4310133	0.99983	10–40
RTD2	3.89370	5.2723539	0.99983	10–40
RTD3	3.91590	-4.1983190	0.99982	10–40
RTD4	3.91300	-2.9021630	0.99982	10–40
RTD5	3.91510	-5.4024260	0.99986	10–40
RTD6	3.92820	-9.4310300	0.99984	10–40
RTD7	3.91560	-7.0878670	0.99988	10–40
RTD8	3.86920	5.1461985	0.99987	10–40
RTD9	3.89700	-1.4634750	0.99984	10–40
RTD10	3.90790	-5.2686380	0.99979	10–40
RTD11	3.90350	-8.8860940	0.99983	10–40
RTD12	3.88260	1.8567227	0.99983	10–40
RTD13	3.92320	-7.1242570	0.99984	10–40
RTD14	3.90360	3.2913678	0.99983	10–40
RTD15	3.90230	4.5089781	0.99981	10–40
RTD16	3.87000	5.5185615	0.99982	10–40
RTD17	3.89580	-1.4353370	0.99982	10–40
RTD18	3.87030	6.4573517	0.99985	10–40
RTD19	3.89880	7.8512684	0.99981	10–40
RTD20	3.87930	2.3219822	0.99985	10–40
RTD21	3.89250	3.4705013	0.99980	10–40
RTD22	3.91880	-6.4691200	0.99986	10–40
RTD23	3.89420	2.2070986	0.99981	10–40
RTD24	3.89010	1.3507405	0.99984	10–40
RTD25	3.88790	-3.7436070	0.99985	10–40
RTD26	3.90640	-4.1288140	0.99984	10–40
RTD27	3.90280	-2.2473680	0.99982	10–40
RTD28	3.89640	-4.0120600	0.99990	10–40
RTD29	3.92410	-4.0059020	0.99980	10–40
RTD30	3.89960	-2.2135840	0.99983	10–40
RTD31	3.90140	-1.4396370	0.99984	10–40
RTD32	3.88510	2.7775140	0.99981	10–40

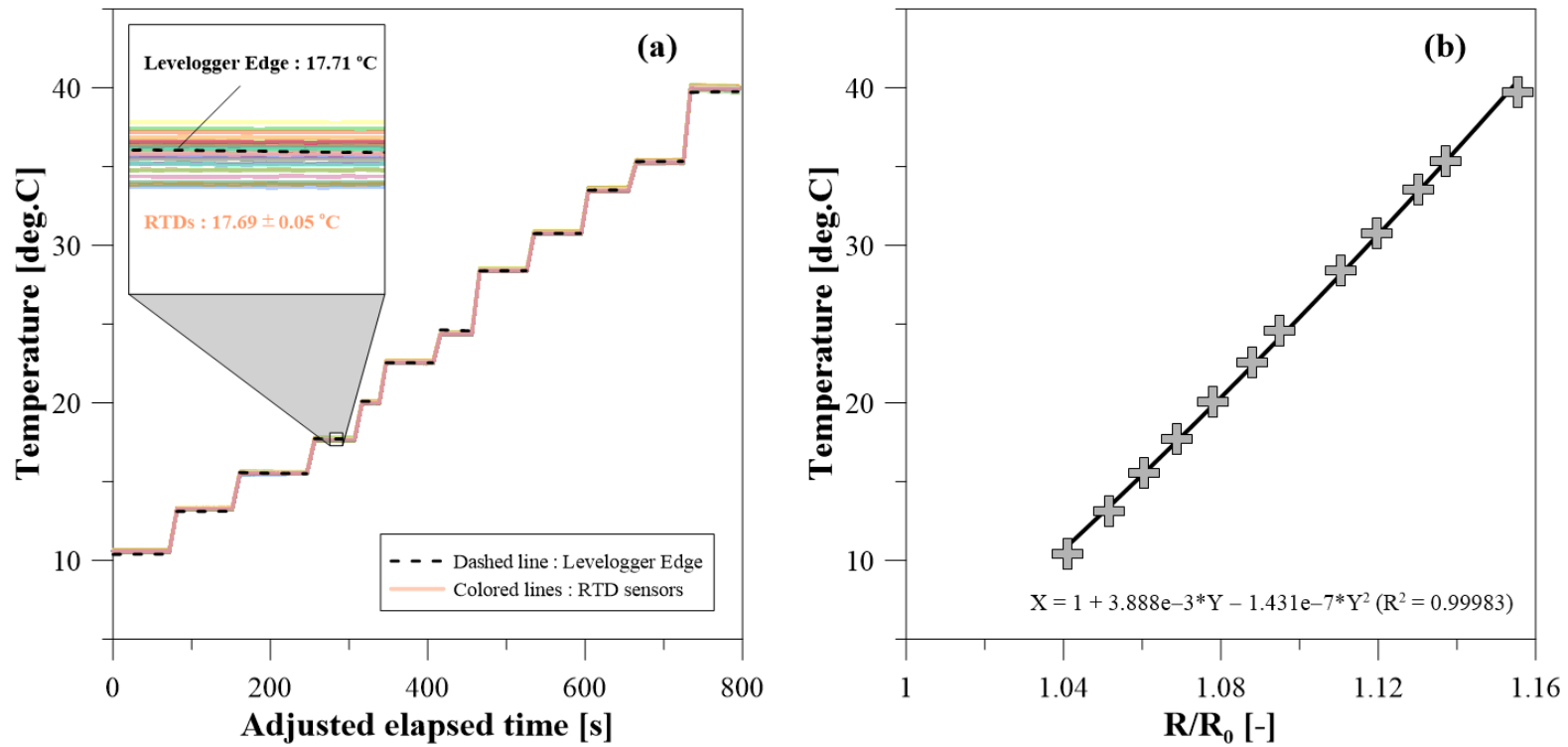


Figure 4.5. A temperature calibration procedure for RTD sensors. (a) Experimental results at 12 step changes in the range of 10 to 40°C and (b) Regression analysis of the relationship between normalized resistance and temperature based on observed data and Callendar–Van Dusen equation.

4.3. Heat transport experiments

Before the middle chamber was filled with sand, the top of the injection well and acrylic tubes with the resistor and RTD sensors mounted were strapped in place to minimize the possibility of movement during the experimental setup. The middle chamber was packed with coarse sand S3 while taking care not to trap air inside the saturated porous medium. After the sand packing process, the hydraulic conductivity was estimated to 4.494×10^{-3} m/s from the Darcy velocity (or specific discharge) and hydraulic gradient measured in a sand tank experiment. The porosity of sand S3 was derived by measuring the dry sand volume and the bulk volume with mass cylinder and burette. The average porosity value of 6 repeated measurements was 0.338 (1.6%), and crosschecked by measuring the moisture content of 33.1% (3%) in the experimental setup with a soil moisture sensor (5TE, Decagon, USA) which was buried at 45 cm above the bottom.

4.3.1. Laboratory-scale heat tracer tests

As shown in Figure 4.3, two different heat sources were installed at a height of 30 cm, and 35–40 cm apart from the higher constant-head tank. One is a small resistor acting as a point heat source, and the other is warm water passing through the well screen, disturbing the background flow field. First, heat tracer tests using a resistor were performed without background flow to estimate the thermal conductivity and the volumetric heat capacity of the saturated porous medium. A constant power of 4.712 W was applied to the resistor for all the tests, and the changes in temperature were measured at 28 RTDs inside the middle chamber. Then, heat tracer tests using a resistor with various background flow were conducted to

estimate the thermal dispersion coefficients of the medium under natural flow conditions. Background flow rates were changed by controlling the water level of the lower constant-head tank. Up to 40.38 m/d with 10 different background flow velocities were applied to the heat tracer tests.

To investigate the effect of water injection, warm water as a heat tracer was injected through the well screen into the porous medium. The injection rates were adjusted by the rotation rates of the peristaltic pump. Three rotation rates (12, 18, and 24 rpm) were selected for the tests, and the corresponding injection rates were about 32, 48, and 65 ml/min (see Section 4.2.2). To ensure the same background flow velocities as the heat tracer tests using a resistor, the injection tests were performed right after the background temperature in the porous medium had recovered from the disturbance by the resistor tests. Due to the sensitivity of the thermostat, the temperature difference (ΔT) between injected water and background water were not consistent in all the injection tests, but all the differences were maintained within 3°C to prevent the density effect from taking place (see Section 4.2.2).

4.3.2. Analytical model for the resistor tests

Assuming that the mean temperatures of solid and liquid phases are in equilibrium (i.e., local thermal equilibrium), the general form of heat transport equation (HTE) considering both convective and conductive transport can be expressed as (see Stauffer et al., 2013):

$$D^t \nabla^2 T - v^t \cdot \nabla T + \frac{P^t}{\rho c} = \frac{\partial T}{\partial t}, \quad (4.5)$$

where T [K] is the temperature of the porous medium, D^t [m²/s] is the thermal dispersion coefficient, v^t [m/s] is the thermal front velocity, and P^t [W/m³] is the heat production rate. The

resistor tests were analyzed by analytical models, which can be derived from the following differential HTE without internal heat sources or sinks (de Marsily, 1986; Rau et al., 2012a):

$$D^t \nabla^2 T - v^t \cdot \nabla T = \frac{\partial T}{\partial t} \quad (4.6)$$

The thermal dispersion coefficient consists of the thermal diffusion and mechanical thermal dispersion terms and can be generally described as:

$$D^t = \frac{\lambda}{\rho c} + \beta \cdot (v^t)^m, \quad (4.7)$$

where λ [$\text{W m}^{-1}\text{K}^{-1}$] represents the bulk thermal conductivity, ρc [$\text{J m}^{-3}\text{K}^{-1}$] is the bulk volumetric heat capacity, β is the thermal dispersivity, and m is the coefficient to express the relationship between the thermal dispersion coefficient and the flow velocity. There was a controversy on whether the relationship is linear ($m = 1$) or not ($m \neq 1$). Most recently, Rau et al. (2012a) found that the relationship can be approximated by a square law ($m = 2$) within natural groundwater flow velocities ($Re < 2.5$) as follows:

$$D^t = \frac{\lambda}{\rho c} + \beta \cdot (v^t)^2. \quad (4.8)$$

The differential HTE in equation (4.6) has been solved for an infinite three-dimensional porous medium with a uniform flow in one direction by Carslaw & Jaeger (1959). The initial condition $T(x, y, z, t = 0) = T_0$ for $-\infty < (x, y, z) < \infty$, and the boundary conditions $Q(0, 0, 0, t > 0) = J$ and $\lim_{x,y,z \rightarrow \pm\infty} Q(x, y, z, t) = 0$ were taken while assuming that Q [W] is the strength of a continuous point heat source moving from the origin of the coordinate system ($x, y, z = 0$) in the x -direction. The resulting analytical solution is described in a modified form as (Rau et al., 2012a):

$$T(x, y, z, t) = T_0 + \frac{Q}{8\pi D_T^t \rho c R} \exp\left(\frac{xv^t}{2D_L^t}\right) \cdot \left[\exp\left(-\frac{Rv^t}{2D_L^t}\right) \operatorname{erfc}\left(\frac{R-v^t t}{2\sqrt{D_L^t t}}\right) + \exp\left(\frac{Rv^t}{2D_L^t}\right) \operatorname{erfc}\left(\frac{R+v^t t}{2\sqrt{D_L^t t}}\right) \right], \quad (4.9)$$

$$R = \sqrt{x^2 + \frac{D_L^t}{D_T^t}(y^2 + z^2)}, \quad (4.10)$$

where D_L^t and D_T^t are the longitudinal and transverse thermal dispersion coefficients. This analytical solution is also known as the moving continuous point source (MCPS) model, which was used to analyze the resistor tests performed with various background flows.

In the case of the resistor tests without background flow, the HTE in equation (4.6) can be reduced to the following equation because heat is transferred only by conduction.

$$D^t \nabla^2 T = \frac{\partial T}{\partial t} \quad (4.11)$$

This equation has also been solved by Carslaw & Jaeger (1959) for an infinite three-dimensional aquitard with a continuous heat source Q [W] at the origin of the coordinate system ($x, y, z = 0$). The following solution is the modified form by Stauffer et al. (2013).

$$T(x, y, z, t) = T_0 + \frac{Q}{4\pi\lambda r'} \operatorname{erfc}\left(\frac{r'}{\sqrt{4D^t t}}\right), \quad (4.12)$$

where $r' = \sqrt{x^2 + y^2 + z^2}$ [m] and D' is the bulk thermal diffusivity [m^2/s] because there is no flow. This analytical solution is called the continuous point source (CPS) model, which was used to interpret the resistor tests without flow. The details on the analysis procedure will be explained in Section 4.3.4.

4.3.3. Numerical model for the injection tests

The experiments using injected water as a tracer were analyzed by a numerical model. In the present chapter, FEFLOW[®] was used to investigate the thermal plume propagation in the saturated porous medium. It is based upon a finite element method and can deal with solute and heat transport as well as groundwater flow in porous media. Essentially, the numerical code is governed by the conservation laws of mass, momentum, and energy for solid and liquid phases (see Diersch, 2005a). The dispersion model used in FEFLOW[®] is a linear model, which can be expressed as follows (Bear, 1972; de Marsily, 1986; Rau et al., 2012a):

$$D^t = \frac{\lambda}{\rho c} + \beta \cdot \left| \frac{\rho_w c_w}{\rho c} \cdot q \right| \quad (4.13)$$

A 3-D finite element grid was constructed for a 3-D model domain with the same dimensions of 1.0 m × 0.6 m × 0.6 m ($L \times W \times H$) as the laboratory experiments. The entire model domain was discretized into square elements ($\Delta x = \Delta y = 0.004$ m) except the zones around an injection point and observation points where the mesh spacing was refined ($\Delta x = \Delta y = 0.002$ m) (Figure 4.6). The initial time step was set to be 10^{-9} d with a maximum time step of 10^{-4} d.

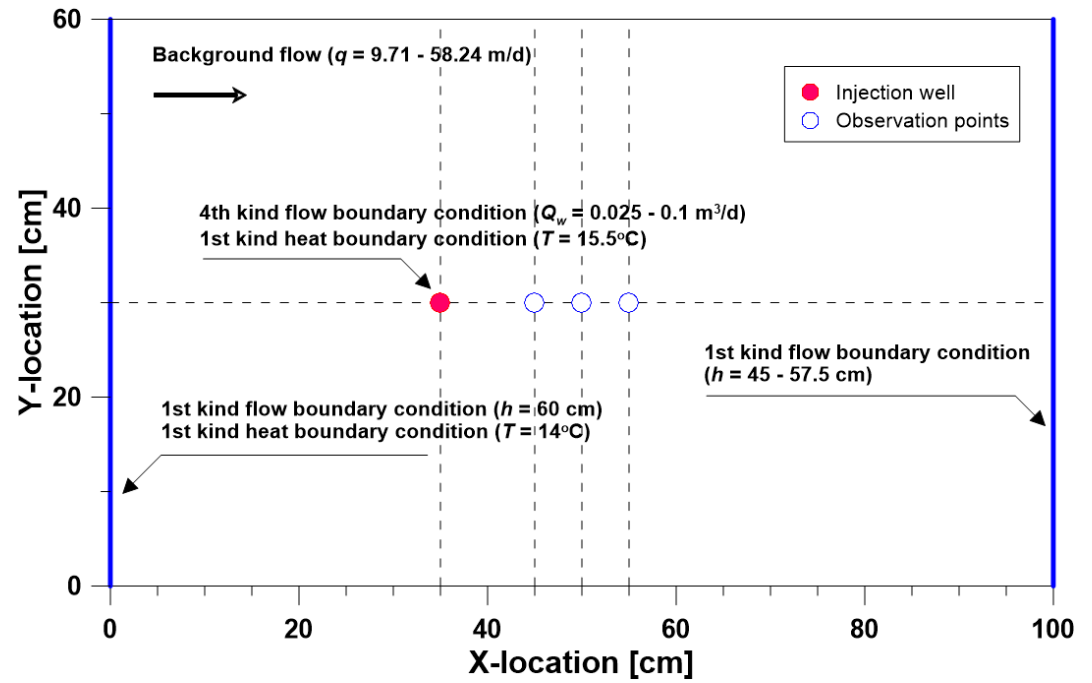
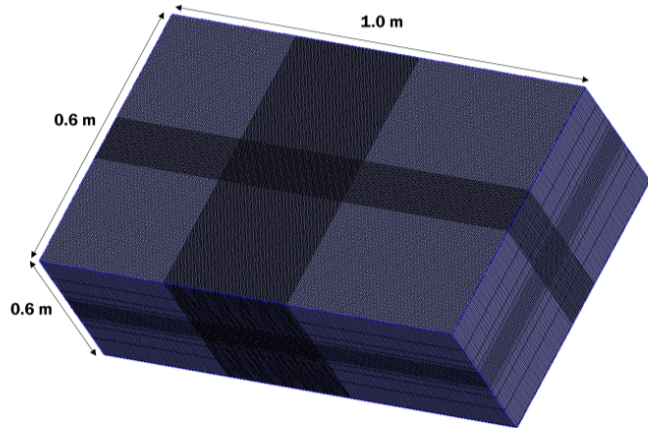


Figure 4.6. A 3-D model domain with the same dimensions as the laboratory experiments and boundary conditions for flow and heat transport.

Figure 4.6 shows the location of the heat source and observation points, and boundary conditions applied to the numerical model. The initial water level was assumed to be 0.6 m all over the model domain. The constant-head boundary conditions reflecting the observed water level were set on both sides of the model domain, and the spatial distribution of the hydraulic head was calculated by performing steady-state simulations. The corresponding hydraulic gradient values had a range from 0.005 to 0.081, based on the experimental conditions.

The initial temperature of the model was set to the background temperature measured before the warm water injection. In the left side of the domain where the background water flows in, the temperature of the background water was used as a constant boundary condition. To represent the injection of warm water, the average injection rates of 32–65 ml/min (depending on the rotational rate of the peristaltic pump) and the temperature observed at the injection well were set to the injection point as boundary conditions. Then, transient simulations were performed to validate the designed model by comparing the modeling results with the observed temperature data. The model input parameters such as the hydrogeological and thermal properties of the porous medium are listed in Table 4.3.

In most of the laboratory-scale experiments on thermal dispersion, only heat was injected into the porous medium, while in the field-scale experiments, injected water with different temperatures has been used as a tracer. Such difference in the type of heat source can also be found between closed-loop and open-loop geothermal systems. In this context, numerical simulations using the validated model were conducted for 48 cases with different heat source type, background flow velocities, and injection rates (see Table 4.4). The case simulation aims to compare the heat transport under the forced flow conditions with that under the natural flow conditions, and to investigate the effect of injection on the flow field, thermal dispersion

coefficient, and relevant heat transport processes.

Table 4.3. Hydrogeological and thermal parameters used for 3-D model simulation.

Parameters	Symbol	Unit	Value	Comment
Horizontal hydraulic conductivity	$K_{xx} = K_{yy}$	10^{-4} m/s	44.94	Experiments
Vertical hydraulic conductivity	K_{zz}	10^{-4} m/s	4.494	Assumption
Specific yield	S_y	–	0.2	default in FEFLOW; Johnson (1967)
Specific storage	S_s	1/m	0.0001	Default in FEFLOW; Anderson & Woessner (1992)
Porosity	n	–	0.331	Experiments
Volumetric heat capacity of water*	$\rho_w c_w$	10^6 J m ⁻³ K ⁻¹	4.203– 4.186	NIST (2019)
Thermal conductivity of water*	λ_w	W m ⁻¹ K ⁻¹	0.572– 0.588	NIST (2019)
Volumetric heat capacity of solid	$\rho_s c_s$	10^6 J m ⁻³ K ⁻¹	2.085	Experiments
Thermal conductivity of solid	λ_s	W m ⁻¹ K ⁻¹	3.567	Experiments
Longitudinal thermal dispersivity	β_L	10^{-3} m	1.232	Experiments
Transverse thermal dispersivity	β_T	10^{-4} m	5.782	Experiments

*Thermal properties of water depend on the temperature conditions (6–14°C) of the experiment, and they are referenced to NIST (2019).

Table 4.4. Cases for different heat source types, background flow velocities, and injection rates.

Case	A	B	C	D	E	F
Hydraulic gradient	0.025	0.050	0.075	0.010	0.125	0.150
(Flow velocity, m/d)	(9.71)	(19.41)	(29.12)	(38.83)	(48.54)	(58.24)
1	$Q_w = 0.100$ m ³ /d, $\Delta T = 1.5$ K, $Q_h = 7.30$ W					
2	$Q_w = 0.075$ m ³ /d, $\Delta T = 1.5$ K, $Q_h = 5.47$ W					
3	$Q_w = 0.050$ m ³ /d, $\Delta T = 1.5$ K, $Q_h = 3.65$ W					
4	$Q_w = 0.025$ m ³ /d, $\Delta T = 1.5$ K, $Q_h = 1.82$ W					

4.3.4. Parameter estimation

As explained in Sections 4.3.2 and 4.3.3, heat tracer tests using a resistor were analyzed by analytical models, while heat tracer tests with warm water injection were interpreted with a numerical model. The thermal breakthrough curves from the models were fitted to the observed data by changing the parameters of interest. Thermal properties and background flow velocities were determined from the best fit between the observations and the model results, which minimizes the root mean square error (RMSE):

$$\text{RMSE} = \left[\sum_{i=1}^n \frac{(M_i - S_i)^2}{n} \right]^{1/2}, \quad (4.14)$$

where M_i and S_i represent the measured and simulated values, respectively. To compare the quality of fit among different experimental conditions, the normalized root mean square error (NRMSE) was defined as follows:

$$\text{NRMSE} = \text{RMSE} / (T_{\max} - T_{\min}), \quad (4.15)$$

where T_{\max} and T_{\min} are the maximum and minimum temperatures in each thermal breakthrough curve, respectively. Figure 4.7 shows an example of the analysis procedure performed in MATLAB code. As shown in Figure 4.7, the RMSE values were calculated by changing variables within the established reference range, and parameters satisfying the least RMSE were determined in each step. This process was repeated in the reduced range including the determined parameters until the estimated values are almost constant (less than 0.1% change).

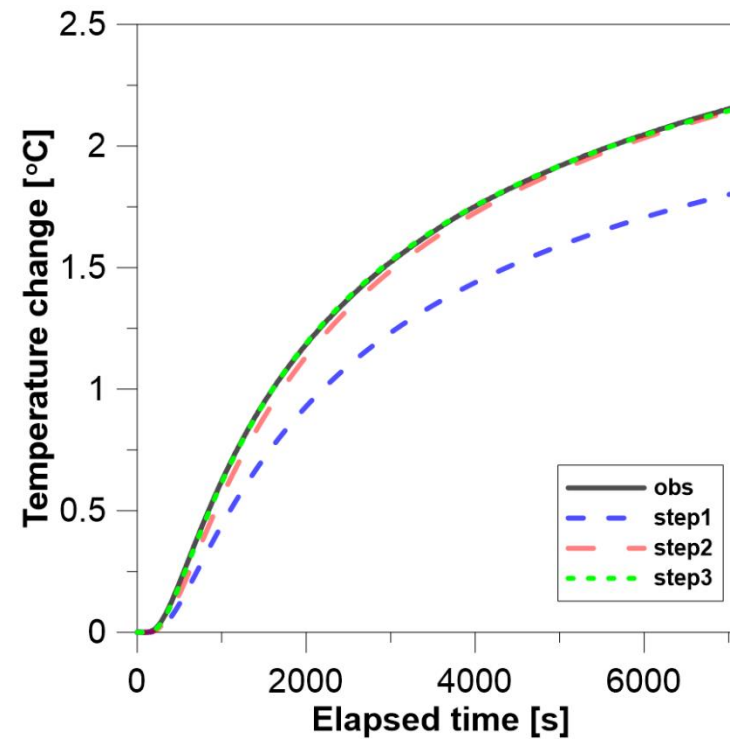
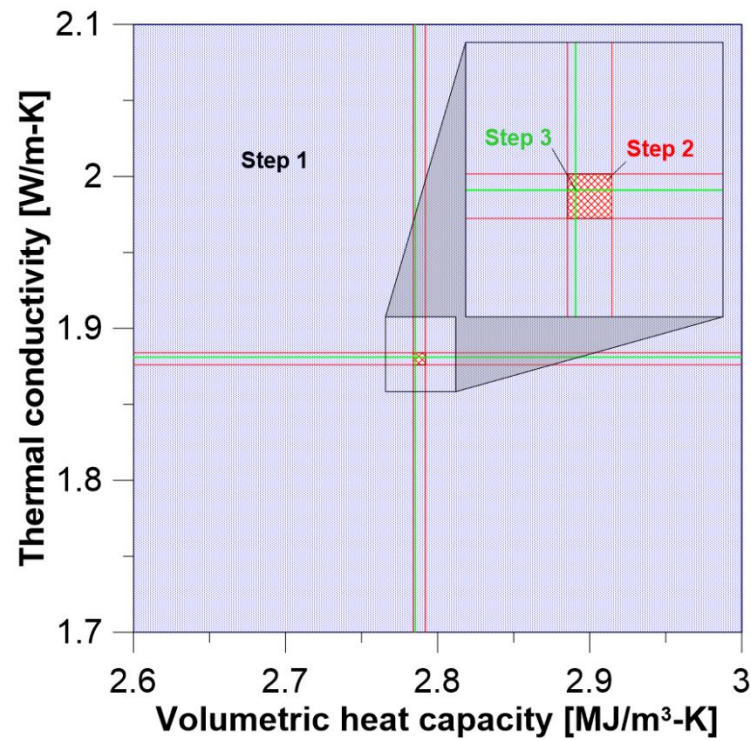


Figure 4.7. An example of the step-wise parameter estimation procedure showing the reference range established in each step and the consequential breakthrough curves. As the number of steps increases, the estimated breakthrough curves approach the observed temperature data.

First, the heat tracer tests using a resistor without background flow were analyzed by the CPS model (equation (4.12)), and the thermal conductivity and volumetric heat capacity of the saturated sand were derived from the analysis results. The thermal conductivity and volumetric heat capacity of solids were estimated by the following relationships between two phases (Buntebarth & Schopper, 1998; Schärli & Rybach, 2001; Woodside & Messmer, 1961):

$$\rho c = n\rho_w c_w + (1 - n)\rho_s c_s, \quad (4.16)$$

$$\lambda = \lambda_w^n \cdot \lambda_s^{1-n}, \quad (4.17)$$

where n is the porosity of the medium, and the subscripts w and s indicate water and solid, respectively. A variety of methods have been proposed to offer the better estimation of the bulk thermal conductivity (see Stauffer et al., 2013). Among the developed techniques, the weighted geometric mean model in equation (4.17) was experimentally evaluated for saturated standard sands in recent years (Tarnawski et al., 2011), and was also demonstrated to offer good estimates for $\lambda_s/\lambda_w \leq 20$ with various sands and silts from Southern Germany (Menberg et al., 2013). In this sense, the weighted geometric mean model was used to calculate the thermal conductivity of the solids (Tables 4.3 and 4.5) and its possible range from materials composition (see Figure 5.8). RTD sensors were mounted on the acrylic tubes and the bottom of each tube was fixed at the predetermined location. However, the upper part of the tubes cannot be perfectly fixed because of sand packing and the RTD lead lines. Although it was tried to avoid unwanted dislocation of sensors, dislocation was found to occur in the course of sand packing and organizing lines. In the locations of the injection well and resistor, RTD sensors cannot be placed at the exact position due to the tubing of the peristaltic pump and resistor. In addition, RTD sensors, tubing, and resistor have volume. For these reasons, the location of sensors was included as a parameter in the fitting procedure, like the previous study (Rau et al.,

2012a), and the resistor tests were repeatedly performed under no flow condition.

In the case of the resistor experiments performed under various background flow conditions, the MCPS model in equation (4.9) was used to derive the parameters such as thermal dispersion coefficients and thermal front velocities. Based on equation (4.13), the regression method was applied to analyze the relationships between the dispersion coefficients and the thermal front velocities estimated with the MCPS model. The statistical models were evaluated by R^2 , F -, and t -statistics. From the analysis results, longitudinal and transverse dispersivity values, which are the coefficients of the velocity term in equation (4.13), were determined.

In this study, two dimensionless numbers were used to quantify the flow and transport regimes. The thermal Peclet number (Pe^t), characterizing the relative contribution of convective and conductive heat transport, is given by (Anderson, 2005; de Marsily, 1986; Rau et al., 2014):

$$Pe^t = \frac{\rho_w c_w q L}{\lambda}, \quad (4.18)$$

where L is a characteristic length [m] that is usually replaced with the mean grain size (d_{50}) of the porous medium. The Reynolds number (Re), representing the ratio of inertia force to viscous force, is defined as (de Marsily, 1986):

$$Re = \frac{\rho_w q d}{\mu}, \quad (4.19)$$

where ρ_w is fluid density [kg/m^3], d is mean grain size (d_{50}) or effective grain size (d_{10}) [m], and μ is fluid viscosity [$\text{kg m}^{-1}\text{s}^{-1}$]. In this study, the mean grain size was used to calculate the dimensionless numbers.

4.4. Results

4.4.1. Analytical modeling for heat tracer tests with a resistor

Heat tracer tests using a resistor as a heat source were performed first under no flow condition to estimate the thermal properties of the porous medium. Figure 4.8 displays the temperature breakthrough curves observed at center and off-center locations (cross symbol), and the CPS model results (solid line). As explained in Section 4.3.4, curve fitting was repeatedly performed by reducing the range of variables until the estimated values were almost constant. The model results agree well with the observed breakthrough curves (Figure 4.8). From the best fit between observations and the model, the thermal conductivity and the volumetric heat capacity of the saturated sand, and the corrected locations were determined (see Table 4.5). The thermal properties of solids were derived from the relationships in equations (4.16) and (4.17), and the thermal conductivity and the volumetric heat capacity of solids were estimated to be on average $3.567 \text{ W m}^{-1}\text{K}^{-1}$ and $2.085 \times 10^6 \text{ J m}^{-3}\text{K}^{-1}$, respectively. Such high values of thermal properties can be explained by the high quartz content of 75.7%, and are within the acceptable range when compared with the reference values in Table 4.5.

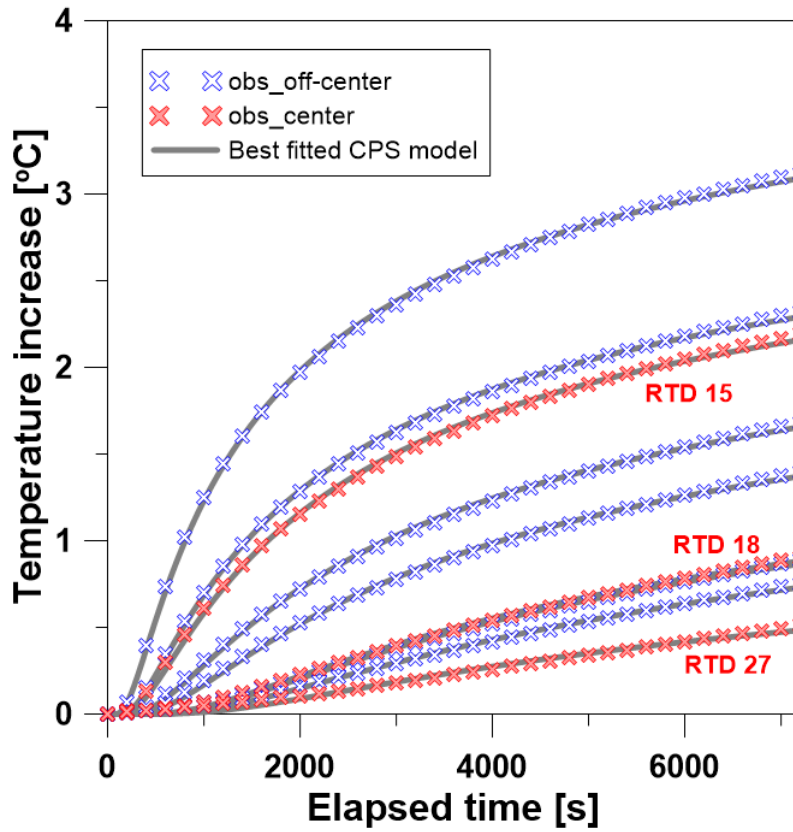


Figure 4.8. Temperature breakthrough curves observed at center and off-center locations (cross symbol), and CPS model results (solid line).

Table 4.5. Thermal properties of porous medium and sensor locations derived from the best fit between the observations and CPS model.

Parameters	RTD 8	RTD 9	RTD 13	RTD 15	RTD 18	RTD 20	RTD 21	RTD 23	RTD 27
r' [m]	0.089	0.041	0.063	0.054	0.088	0.094	0.050	0.070	0.111
$\rho_s c_s$ [J m ⁻³ K ⁻¹]*	2,054,751	2,243,503	2,109,992	1,956,445	2,084,196	2,065,733	2,168,286	2,107,381	1,977,042
λ_s [W m ⁻¹ K ⁻¹ **	3.225	3.855	3.530	3.703	3.265	3.222	3.858	3.488	3.960
RMSE	0.013	0.019	0.015	0.020	0.013	0.013	0.016	0.013	0.015
NRMSE	0.015	0.006	0.009	0.009	0.015	0.017	0.007	0.009	0.030

* Reference range for volumetric heat capacity of dry sand/quartz (mineral): $1.3\text{--}1.6 \times 10^6$ J m⁻³K⁻¹ (Stauffer et al., 2013)/ 2.01×10^6 J m⁻³K⁻¹ (Balland & Arp, 2005)

** Reference range for thermal conductivity of dry sand/quartz (mineral): $0.3\text{--}0.8$ W m⁻¹K⁻¹ (Stauffer et al., 2013)/ $7.2\text{--}8.4$ W m⁻¹K⁻¹ (Balland & Arp, 2005)

Heat tracer tests using a resistor were also performed with various background flow velocities to estimate the thermal dispersion coefficients and the thermal front velocities. Figure 4.9 shows two examples of the observed breakthrough curves and the best-fitted MCPS models for three observation points ($r' = 0.0538, 0.0876, \text{ and } 0.1113 \text{ m}$) at Darcy velocities of 1.94 m/d and 21.35 m/d. Although a deviation at the beginning of the plateau was found in Figure 4.9b, which has high NRMSE values, the analytical models successfully reproduced the observed temperatures in terms of $R^2 > 0.9932$ for all the experiments.

Figure 4.10 illustrates the relationship between the thermal dispersion coefficients and the thermal front velocities estimated from the best-fitted models. Although the heat tracer tests in this study were performed in the conduction dominant regime ($Pe' < 1$), it was observed that both longitudinal and transverse thermal dispersion coefficients increase with the flow velocities. To quantify their relations and to derive thermal dispersivity values, a simple linear regression analysis was conducted. The linear regression equations, estimated by the least square method, showed an increasing trend with R^2 values of 0.7981 in longitudinal and 0.2535 in transverse directions (see black solid lines in Figure 4.10). F - and t -statistics for the regression models indicated that the models and their coefficients are meaningful at the significance level of 0.001 (longitudinal) and 0.005 (transverse). From the analysis results, longitudinal and transverse thermal dispersivities were estimated to be 1.232×10^{-3} and 5.782×10^{-4} m, respectively. However, data scatter was also found in the relationships between the thermal dispersion coefficients and the thermal front velocities. This will be discussed in Section 4.5.1.

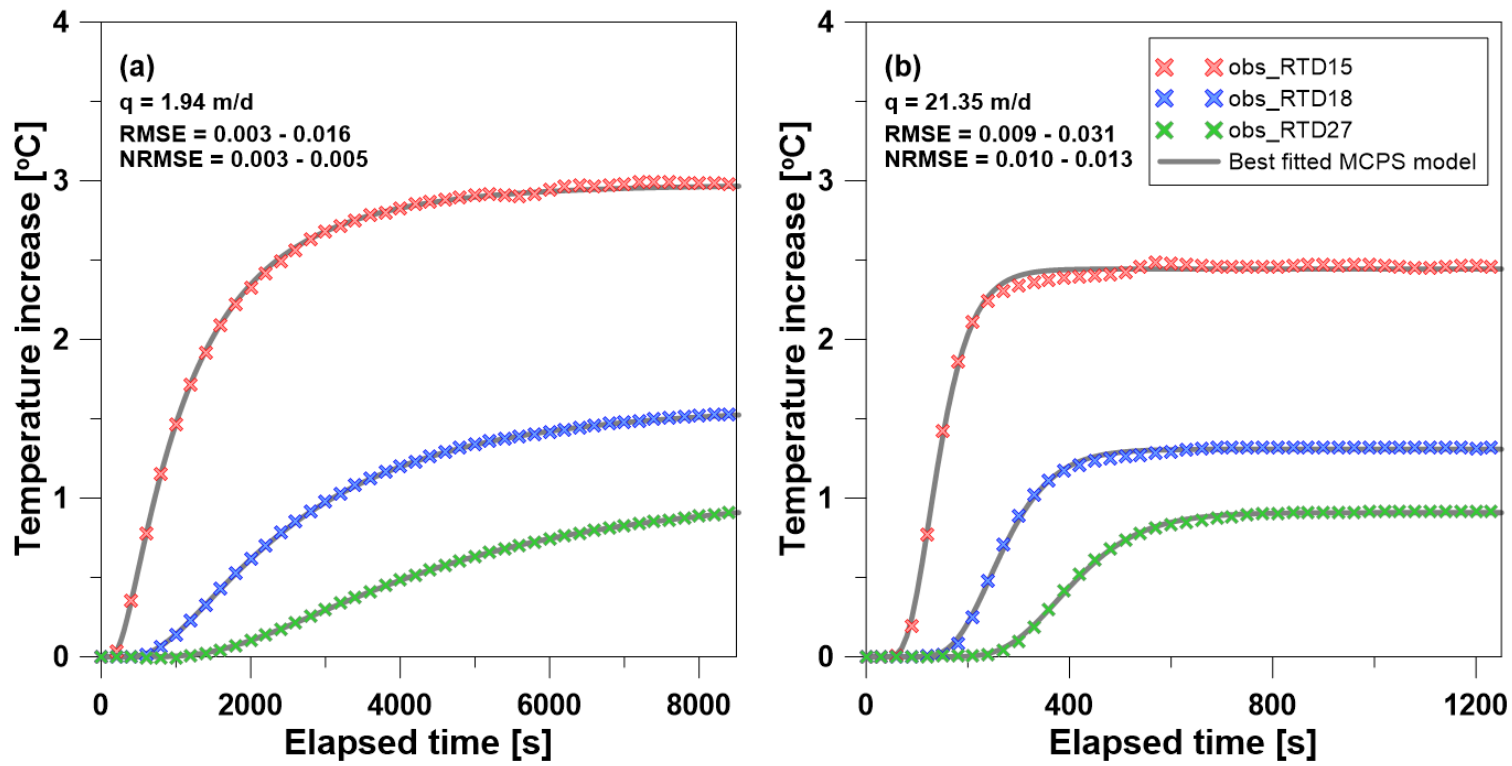


Figure 4.9. Two examples of the observed breakthrough curves and the best-fitted MCPS models for three observation points ($r' = 0.0538$, 0.0876, and 0.1113 m) at Darcy velocities of (a) 1.94 m/d and (b) 21.35 m/d.

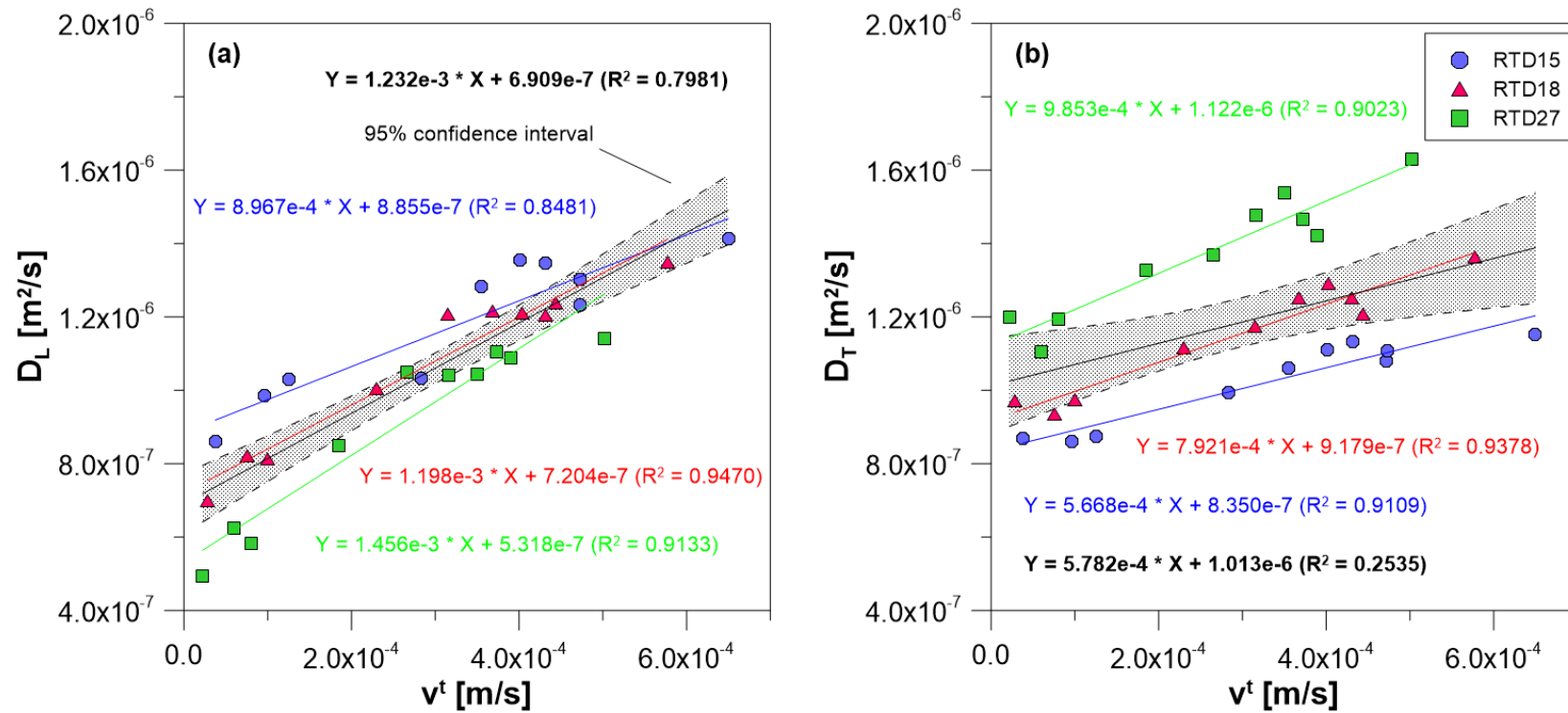


Figure 4.10. Relationships between the thermal dispersion coefficients and the thermal front velocities estimated from the best-fitted models: (a) Longitudinal and (b) Transverse directions. The black lines indicate the regression lines for the relationships and the shaded areas represent their 95% confidence interval.

4.4.2. Numerical modeling for heat tracer tests with injected water

Injection tests were conducted to investigate the influence of water injection on the flow field, thermal dispersion coefficients, and relevant heat transport processes. Figure 4.11 shows the temperature breakthrough curves for the observed data (red circle) and the developed model (yellow square), and their relative errors at $r' = 10.135$ cm with a Darcy velocity of 7.57 m/d. Although a deviation was observed, especially at the beginning and near the plateau of the breakthrough curves, the developed model was found to match well with the observations ($R^2 = 0.9946$). The numerical model used in this study (FEFLOW[®]) cannot simulate the heat transport processes without dispersion effect. Therefore, the numerical simulations were performed with thermal dispersivity values that are small enough to be neglected ($\beta \times 10^{-2}$ and $\beta \times 10^{-4}$), and their results were compared. The solid and dashed lines in Figure 4.11 denote the simulation results when neglecting the thermal dispersivity values. Although the dispersivity values estimated in this study are very small ($\beta_L = 1.232 \times 10^{-3}$ and $\beta_T = 5.782 \times 10^{-4}$), it was found that the RMSE values of the simulations not considering dispersivity are twice that of the simulation considering dispersivity.

Figure 4.12 represents the temperature–time series for two different heat source types of injected water and heat flux, observed at three points ($r' = 5, 10,$ and 30 cm) with Darcy velocities of 9.71 and 58.24 m/d. As shown in Figure 4.12, the results can vary greatly depending on the heat source type even if the same amount of heat is injected. In particular, when the background flow velocity is slow and the injection rate is large, there is a great deal of difference in the temperature breakthrough curves (see Figure 4.12a).

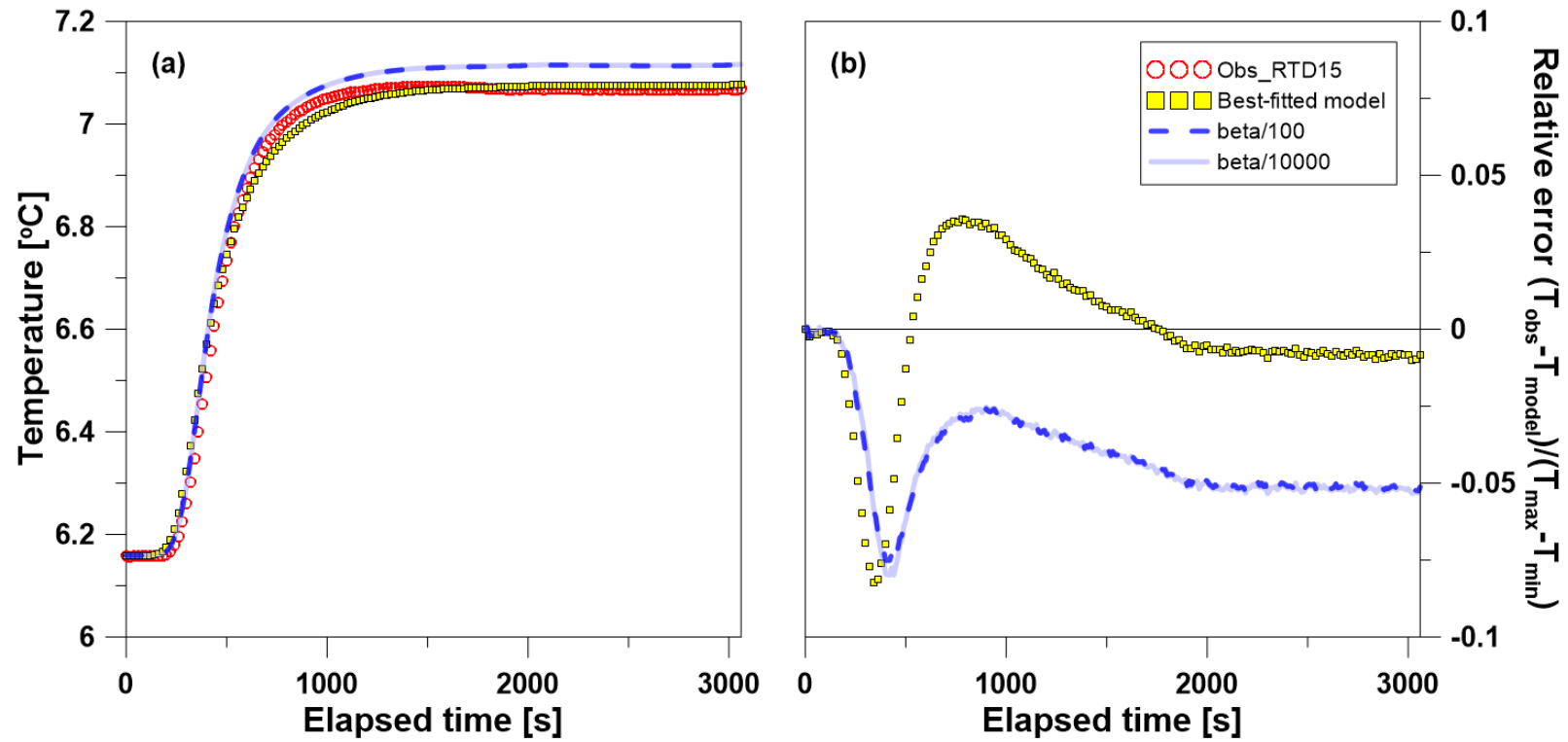


Figure 4.11. Comparison of numerical models with and without dispersion effects. (a) Temperature breakthrough curves for the observed data and the developed model, and (b) Their relative errors at $r' = 10.135$ cm with a Darcy velocity of 7.57 m/d.

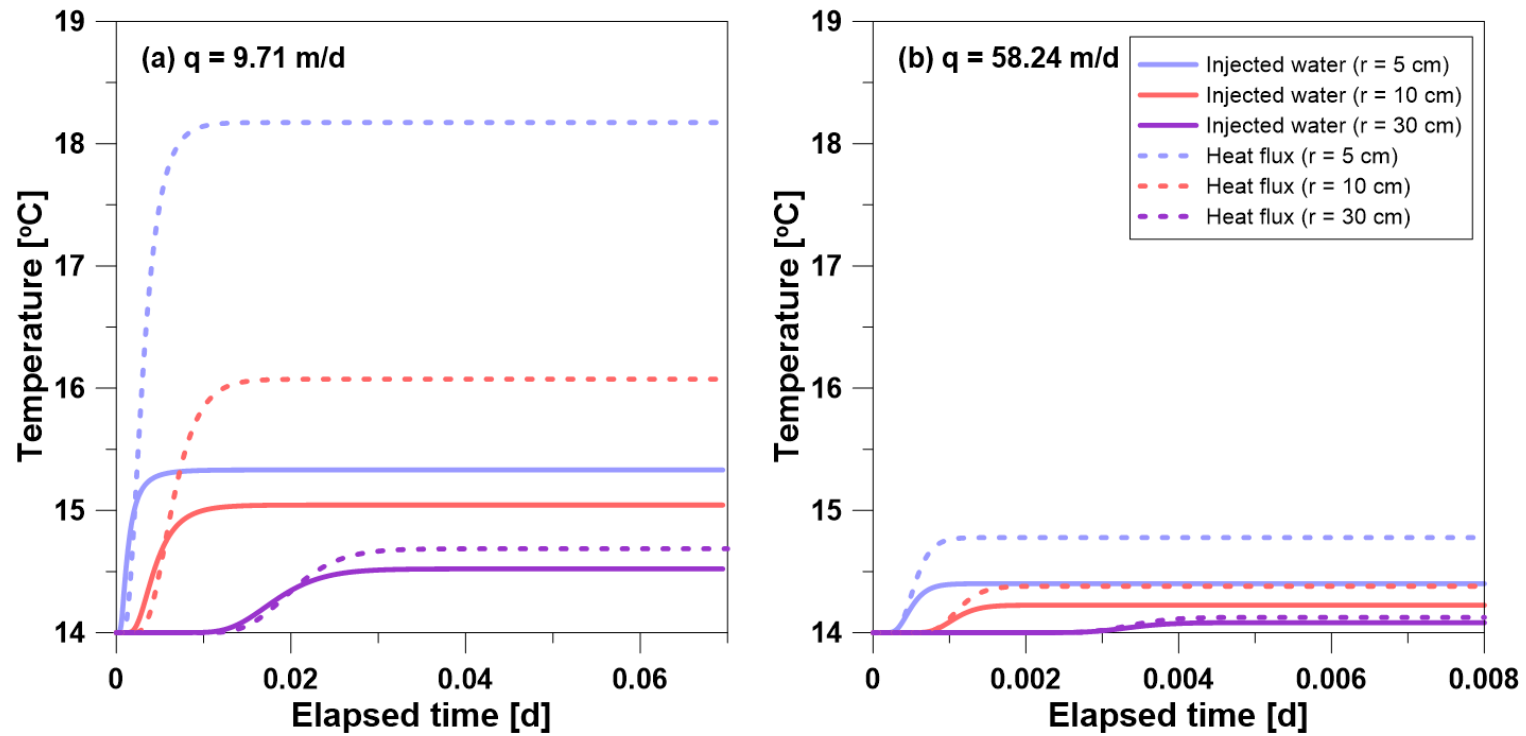


Figure 4.12. Temperature breakthrough curves for two different heat source types of injected water and heat flux observed at three points ($r' = 5, 10,$ and 30 cm) with (a) a low flow velocity and high injection rates ($q = 9.71$ m/d, $Q_w = 0.1$ m³/d, and $Q_h = 7.30$ W), and (b) a high flow velocity and low injection rates ($q = 58.24$ m/d, $Q_w = 0.025$ m³/d, and $Q_h = 1.82$ W).

Figure 4.13 indicates the forced flow field due to warm water injection at various flow velocities and injection rates. It was observed that a dramatic increase in flow velocities occurs, especially near the injection well (Figure 4.13a). When the results were expressed by the thermal Peclet number, the regions close to the injection point were found to stay within the transition zone ($0.5 < Pe' < 2.5$) or convection dominant regime regardless of background flow velocities (Figure 4.13b).

The thermal dispersion coefficients were calculated from equation (4.13) using the estimated properties of the porous medium and the modeled flow velocities. Figure 4.14 shows the effect of water injection on the thermal dispersion coefficients as a ratio to the background value at various background flow velocities (9.71–58.24 m/d) with an injection rate of 0.1 m³/d. The results indicated that the thermal dispersion coefficients also increase greatly around the injection point, up to 2.89 times longitudinally and up to 1.93 times transversally even in the linear dispersion model used in this study.

An additional modeling was performed to investigate the effect of thermal dispersivity on thermal plume propagation under the forced flow field by injected water. Figure 4.15 shows the temperature breakthrough curves for different dispersivity values ($\beta \times 0.01, 1, 10, \text{ and } 100$) observed at two observation points ($r' = 10$ and 30 cm) with a background flow velocity of 9.71 m/d and an injection rate of 0.1 m³/d. The result indicated that thermal dispersivity has a great influence on both breakthrough time and peak temperature of the thermal plume.

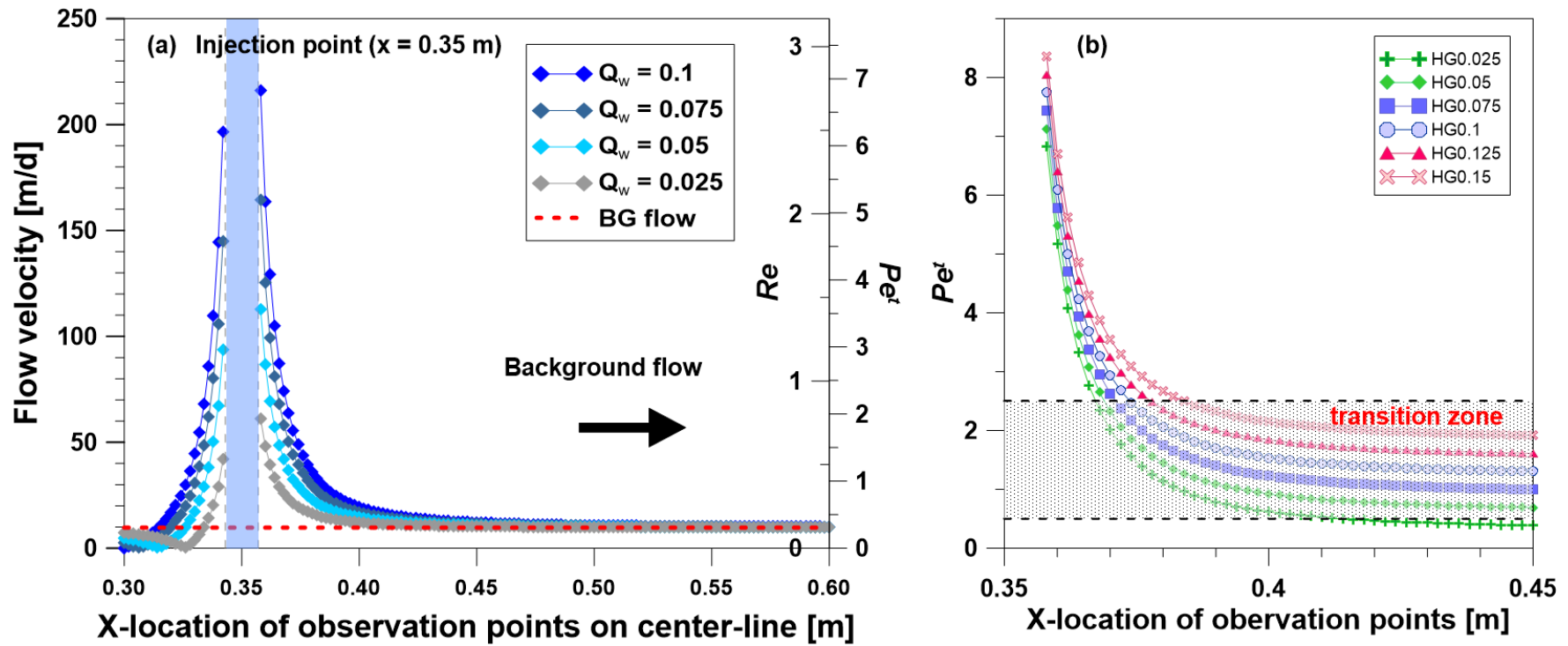


Figure 4.13. Influence of injected water on the flow field. (a) Flow velocities along the x-axis at a background flow velocity of 9.71 m/d and (b) Thermal Peclet numbers at an injection rate of $0.1 \text{ m}^3/\text{d}$.

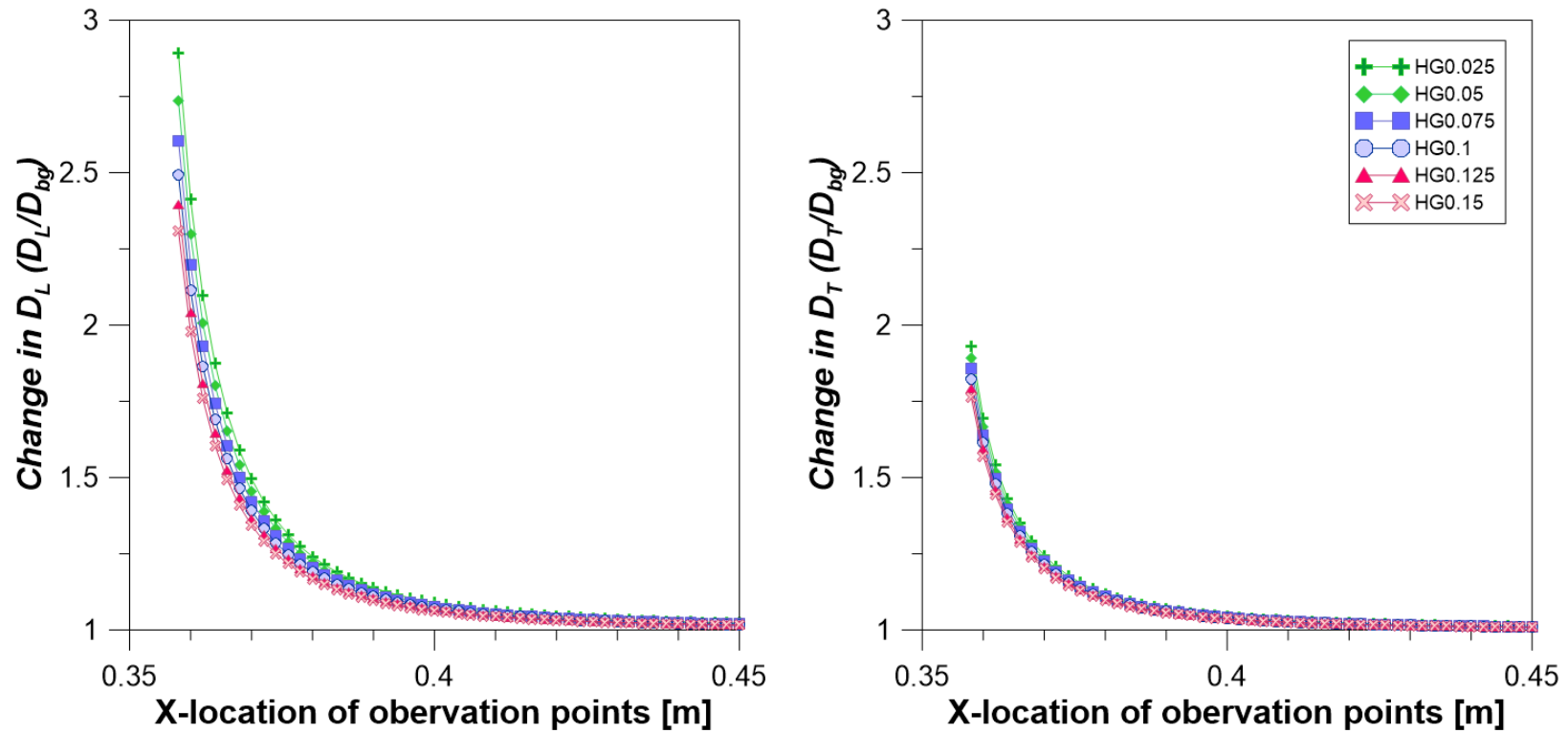


Figure 4.14. Effect of injected water on both (a) longitudinal and (b) transverse thermal dispersion coefficients expressed as a ratio to background value at various background flow velocities (9.71–58.24 m/d) with an injection rate of 0.1 m³/d.

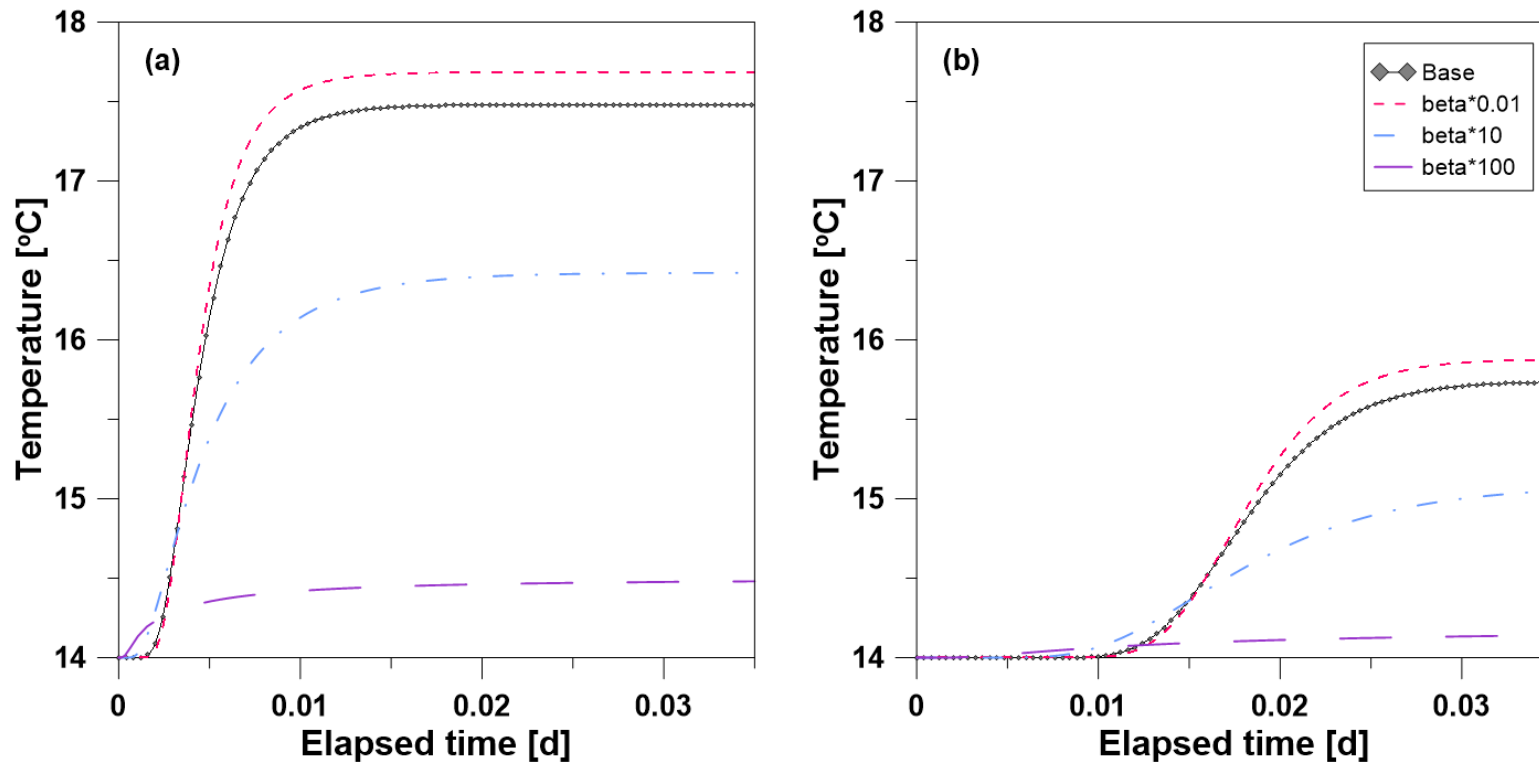


Figure 4.15. Temperature breakthrough curves for different dispersivity values ($\beta \times 0.01, 1, 10,$ and 100) observed at two observation points of (a) $r' = 10$ cm and (b) $r' = 30$ cm with a background flow velocity of 9.71 m/d and an injection rate of 0.1 m³/d.

4.5. Discussions

4.5.1. Relationship between thermal dispersion coefficients and flow velocities

Although heat tracer tests in this study were performed within the conduction dominant regime ($Pe^t < 1$), it was observed that thermal dispersion coefficients increase with flow velocities (Figure 4.10). However, there was also the scatter in their relations as found in the previous studies, especially for low flow velocities (Kunii & Smith, 1961; Rau et al., 2012a; Yagi et al., 1960; Yuan et al., 1991). There can be several reasons. As Yuan et al. (1991) explained about the results of Kunii & Smith (1961), the dominant part of the thermal dispersion coefficient is the effective thermal diffusivity (first term in equation (4.7)) when Pe^t is very low. In such a case, the contribution of the fluid flow to the coefficient is very small. In addition, flow can be nonuniform even if the small-scale experiments were performed with relatively homogeneous sand ($U = 1.36$) as Rau et al. (2012b) mentioned in their experiments, and this can be supported by the thermal front velocities estimated from heat tracer tests. Differences in the estimated thermal conductivities and volumetric heat capacities can be another reason for the scatter. When the relations were analyzed by observation points, a more distinct trend was observed even in the transverse dispersion coefficients with very high R^2 values over 0.9 (Figure 4.10). It is noteworthy that the longitudinal dispersion coefficient reduces the difference due to the thermal properties and converges at a high flow velocity, while the transverse dispersion coefficient maintains a deviation. Such a difference may cause the transverse thermal dispersion coefficient to have more scatter and low R^2 values at a low flow velocity, as observed in the previous study (Rau et al., 2012a).

As shown in Figure 4.10, the longitudinal and transverse thermal dispersivity values estimated by the linear regression method present thermal dispersivity ratios (β_L/β_T) of 1.48–

2.13 (cf. 3.70 in Rau et al. (2012a) and 3.00 in Saeid et al. (2014)). It is noted that these ratios are different from the value of 10 used in commercial software packages or commonly assumed for heat transport (Alcaraz et al., 2016; Hopmans et al., 2002; Lo Russo & Civita, 2009; Lo Russo et al., 2011; Molson et al., 1992; Park et al., 2015a; Park et al., 2015b; Piga et al., 2017; Smith & Chapman, 1983; Su et al., 2004). The difference in the dispersivity ratio can affect the thermal plume propagation and this will be covered in Section 4.5.2.

4.5.2. Impacts of injected water on flow and heat transport

Because groundwater flow velocity is relatively slow and thermal diffusion occurs much faster than solute diffusion by two orders of magnitude, the effective thermal diffusivity containing the mechanical dispersion term as a constant has been used in applications such as closed-loop geothermal systems. However, the results can vary greatly depending on the heat source type, especially when the background flow is slow and the injection rate is high (see Figure 4.12). It is noted that these conditions are common in field applications such as GWHP systems.

As shown in Figures 4.13 and 4.14, injected water increases both flow velocities and thermal dispersion coefficients, especially near the injection well, and thus makes the effect of mechanical dispersion on heat transport very important even at low background flow velocity (Figure 4.15). Although heat tracer tests in this chapter were performed within the conduction dominant regime ($Pe^t < 1$), it was observed that the regions around the injection well stay in the different thermal regimes of the transition zone ($0.5 < Pe^t < 2.5$) or convection dominant regime (see Figure 4.13b). This suggests that the relationship between the thermal dispersion coefficient and thermal front velocity should be described by a square law in equation (4.8)

(Rau et al., 2012a) or a power law in equation (4.7) (Green et al., 1964; Lu et al., 2009; Metzger et al., 2004). However, most commercial software packages, including FEFLOW[®], are based on the linear dispersion model in equation (4.13), and this can lead to errors in the analysis of thermal behavior in high-velocity fields around the injection well.

The thermal dispersivities in current work were estimated to have very small values ($\beta_L = 1.232 \times 10^{-3}$ m and $\beta_T = 5.782 \times 10^{-4}$ m) because relatively homogeneous sand ($U = 1.36$) was used in the experiments. Thermal dispersivities on the field scale, however, are much larger and have a wide range of values depending on the degree of heterogeneity (see Molina-Giraldo et al., 2011; Stauffer et al., 2013). In field applications such as GWHP systems, large amounts of pumping and injection can further increase the magnitude of thermal dispersion. For these reasons, the impacts of injection on the field scale were investigated using the field-based model in Park et al. (2015a) at a regional groundwater flow velocity of 3.64 m/d with various injection rates of 50–200 m³/d. The modeling results confirmed that the effect of injected water on flow and heat transport observed in the laboratory-scale experiments can also be found on the field scale (Figure 4.16). It is noteworthy that the radius of hydraulic and thermal effects has greatly increased from tens of centimeters on the laboratory scale to tens of meters on the field scale.

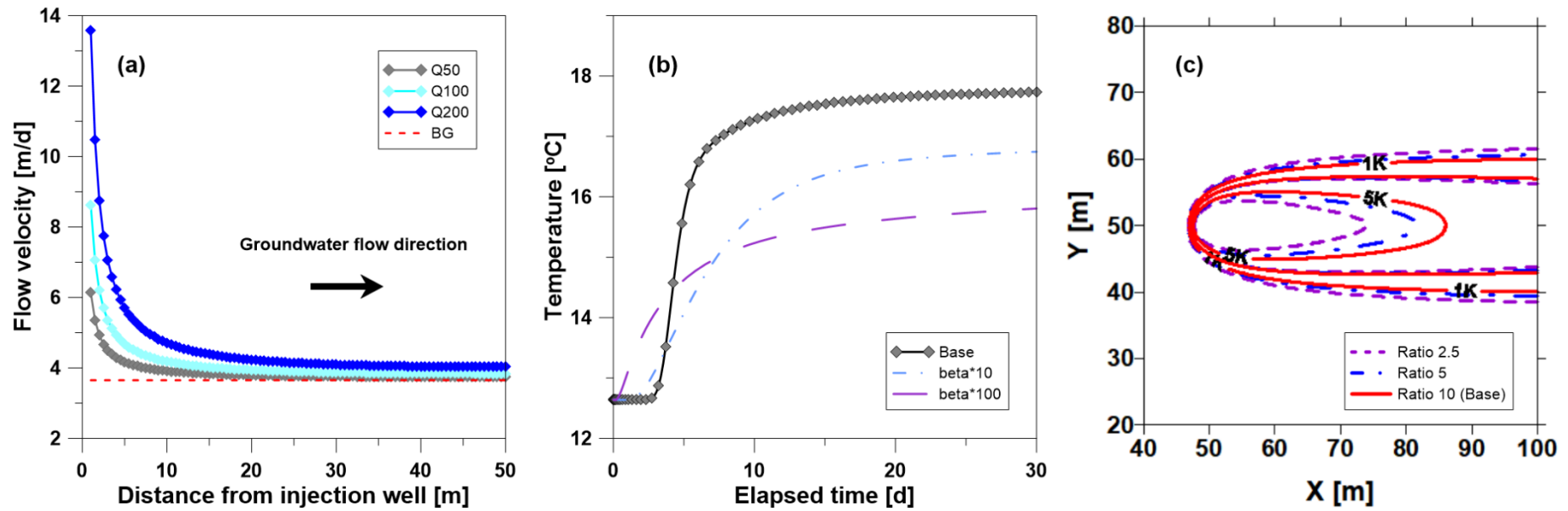


Figure 4.16. Up-scaled modeling results performed at a regional groundwater flow velocity of 3.64 m/d with various injection rates of 50–200 m³/d indicating the impacts of injection on (a) flow velocity field, (b) thermal plume propagation, and (c) dimensions of the thermal plume.

As mentioned in Section 4.5.1, the difference in the thermal dispersivity ratio can affect the heat transport processes, and therefore the field-scale simulations were performed for 30 days to investigate the effect of the dispersivity ratio by adjusting the transverse dispersivity value. As can be seen in Figure 4.16c, the thermal dispersivity ratio has a significant effect on both plumes length and width. This differs from a recent study on the thermal risk assessment of GWHPs, where the authors used the fixed dispersivity ratio of 10 and showed that the thermal dispersivity has a significant effect on plume length but a negligible impact on plume width (Piga et al., 2017). In particular, the results are significant because the transverse thermal dispersivity has been rarely estimated although field experiments were carried out.

The mechanical dispersion term has often been neglected or underestimated because thermal diffusion occurs much faster than solute diffusion and groundwater flow velocity is relatively slow. Injected water, however, greatly increases the flow velocity and makes the region around the injection point into a different thermal regime (Figure 4.13b), where the thermal dispersivity can be significant regardless of a background flow velocity (Figures 15 and 16). Moreover, Sauty et al. (1982) inferred from the field experiments that the macroscopic thermal dispersivity can vary greatly depending on the distance traveled by the thermal plume and the degree of aquifer heterogeneity, which is consistent with recent findings on the scaling behavior of macrodispersivity (Chang & Yeh, 2012; Zech et al., 2015). This can be the reason for the wide range of dispersivity values reported in the literature (Molina-Giraldo et al., 2011; Stauffer et al., 2013). Therefore, field-based assessment of thermal dispersivity is required to ensure sustainability in applications such as the GWHP system without underestimating or overestimating the associated thermal effects.

4.6. Conclusions

In this study, laboratory-scale heat tracer tests using two different heat sources were performed at various background flow velocities ($Re < 0.52$) to investigate the effects of injected water on the flow field, dispersion coefficient, and associated transport processes. The resistor experiments were analyzed by a curve fitting procedure and the analytical models were confirmed to be successful in reproducing the observed temperature data ($R^2 > 0.9932$ for all the tests). From the analysis results, thermal front velocity and the three thermal properties of thermal conductivity, volumetric heat capacity, and thermal dispersion coefficient were estimated.

Although the experiments in this study were performed at a low background flow velocity ($Pe' < 1$), the thermal dispersion coefficients were observed to increase with the flow velocities. However, data scatter was also found in their relationship and this might be explained by the thermal regime and nonuniform flow. In addition, the regression analysis result conducted by observation points indicates that spatial differences in thermal properties can be another reason for scattering.

In the case of injection tests, the numerical model was used to analyze the experimental results, and case simulations using the validated model were performed at different heat source types, background flow velocities, and injection rates. The mechanical dispersion term has often been neglected or underestimated due to the fast thermal diffusion and relatively slow groundwater flow. However, the simulation results indicate that there can be a great deal of difference in the temperature breakthrough curves depending on the heat source type. Injected water increases both flow velocities and thermal dispersion coefficients, especially near the injection well, and thus makes the mechanical dispersion significant even at low flow velocity.

Although heat tracer tests in this study were conducted within the conduction dominant regime ($Pe' < 1$), it was found that the regions around the injection well stay in the different thermal regimes of the transition zone ($0.5 < Pe' < 2.5$) or convection dominant regime. This suggests that the relationships between thermal dispersion coefficient and thermal front velocity should be described by a square law (Rau et al., 2012a) or a power law (Green et al., 1964; Lu et al., 2009; Metzger et al., 2004). However, most commercial software packages are based on a linear dispersion model, which can result in errors in the analysis of the heat transport processes at a high-velocity field near an injection well.

Field-based modeling results have shown that the effect of injected water on flow and heat transport observed in laboratory-scale experiments can also be found in field-scale applications. It is notable that the radius of hydraulic and thermal effects has increased significantly from tens of centimeters on the laboratory scale to tens of meters on the field scale. The difference in the thermal dispersivity ratio found in the experimental results was also investigated in the field-scale simulations. The results show that the thermal dispersivity ratio affects the dimension of the thermal plume. This is very important because the transverse thermal dispersivity has been hardly estimated even when the field experiments were performed.

In field applications, the mechanical thermal dispersion has often been neglected or underestimated by using zero or the default value in the simulators, or by using the scaling law for solute dispersivity as a thermal dispersivity value. The experimental and numerical results in this chapter indicate that mechanical thermal dispersion can be significant even at low background flow velocity. In particular, thermal dispersivity on a macroscale is known to increase depending on the scale of measurement and the degree of aquifer heterogeneity (Sauty et al., 1982; Chang & Yeh, 2012). A recent study on the scaling behavior suggests, based on

extensive experimental field results, that the macrodispersivity for a solute does not follow a unique scaling law but is site-specific (Zech et al., 2015). Therefore, to ensure the efficiency and sustainability in field applications such as GWHP systems, it is necessary to evaluate site-specific thermal dispersivity through field experiments.

Chapter 5

Anisotropy Ratio of Longitudinal to Transverse Thermal Dispersivity

This chapter will be published with modifications:

Park, B. H., & Lee, K. K. (In Preparation). Anisotropy Ratio of Thermal Dispersivity Affecting Plume Geometry for Groundwater Heat Pump (GWHP) Systems.

5.1. Introduction

Heat transport in saturated porous media is governed by three mechanisms: advection by the fluid phase, conduction by the solid and fluid phases, and mechanical dispersion by the spatially variable velocity field at the pore scale and the heterogeneous permeability field at the macroscopic scale (de Marsily, 1986; Molina-Giraldo et al., 2011). Thermal dispersion, however, has often been neglected or underestimated in the simulation of heat transport in porous media in that thermal diffusion is hundreds of times faster than solute diffusion and the groundwater flow velocity is relatively slow (Molina-Giraldo et al., 2011; Park et al., 2018). For the last few decades, experimental investigations have been conducted to identify the

dispersion behavior in porous media, demonstrating that the thermal dispersion increases with flow velocity (Anderson, 2005; Bandai et al., 2017; Bear, 1972; Bons et al., 2013; de Marsily, 1986; Green et al., 1964; Hatch et al., 2006; Keery et al., 2007; Lu et al., 2009; Metzger et al., 2004; Park et al., 2018; Rau et al., 2010; Rau et al., 2012a; Rau et al., 2014; Vandenbohede et al., 2009; Vandenbohede & Lebbe, 2010; Yagi et al., 1960). Moreover, large volumes of groundwater generally used in GWHP systems can greatly increase the flow velocity especially around the injection well, leading to an increase in thermal dispersion (Park et al., 2015a; Park et al., 2018). Therefore, thermal dispersion can play an important role in assessing the thermal impacts of the GWHP system.

Many studies on low-enthalpy geothermal applications have indicated that thermal dispersion can be an important heat-transport mechanism in saturated porous media. For instance, Sauty et al. (1982) performed the experimental and numerical investigations and found that thermal dispersion plays an important role in the recovery ratio of aquifer thermal energy storage (ATES). This finding was also confirmed in other numerical studies on ATES experiments (Dwyer & Eckstein, 1987). Lo Russo & Civita (2009) evaluated the feasibility of the GWHP system for a large commercial building and found that thermal plume dimension and geometry are dependent on thermal dispersivity. This is evident in the sensitivity analysis of the GWHP system, showing that thermal plume size varies with longitudinal and transverse thermal dispersivity values (Lo Russo et al., 2012). Park et al. (2015a) investigated the importance of the estimated thermal dispersivity in designing a GWHP system and concluded that the thermal dispersivity of the aquifer have strongly affect the subsurface temperature distribution as well as the arrival time, especially in the elevated velocities induced by pumping and injection. Most recently, Piga et al. (2017) conducted a comprehensive sensitivity analysis

with long-term numerical simulations for open-loop GWHP systems. Their results suggest that thermal dispersivity does not affect the maximum plume width but has a considerable effect on plume length. From a closed-loop geothermal perspective, Molina-Giraldo et al. (2011) performed the analytical modeling on temperature plume development and concluded that thermal dispersion can have a great influence on the temperature distribution around borehole heat exchangers. At a regional scale, Alcaraz et al. (2016) quantified the shallow geothermal potential and related environmental impacts. The analysis results suggest that the consideration of dispersion effects is very important in terms of accuracy and reliability.

In recent years, a variety of researches have been performed in the field of GWHP, such as comprehensive sensitivity analysis (Piga et al., 2017), dynamic viscosity (Lo Russo et al., 2018), injected water (Park et al., 2018), analytical solution (Pophillat et al., 2018), multi-well pairing (Kim et al., 2018), and single-well circulation (Tu et al., 2019). Although all of them considered thermal dispersion effects, but most studies used the default values given in their numerical models as thermal dispersivity. It is noteworthy that transverse dispersivity is generally assumed to be one-tenth that of longitudinal dispersivity (Alcaraz et al., 2016; Hopmans et al., 2002; Kim et al., 2018; Lo Russo & Civita, 2009; Lo Russo et al., 2012; Lo Russo et al., 2018; Molson et al., 1992; Park et al., 2015a; Park et al., 2015b; Piga et al., 2017; Pophillat et al., 2018; Smith & Chapman, 1983; Su et al., 2004; Tu et al., 2019), even when field experiments are carried out. However, the ratios of longitudinal to transverse dispersivity reported in the literature (see Andrews & Anderson, 1979; Rau et al., 2012a; Saeid et al., 2014; Park et al., 2018) suggest that such assumption can be violated. Because most previous studies considering thermal dispersion employed the fixed value for thermal dispersivity ratio, its effect was not fully investigated to the best of my knowledge.

This study aims to investigate the effects of thermal dispersivity ratio on thermal plume propagation through fully saturated porous media with different grain size distributions. This chapter used the laboratory experimental system designed to examine the influence of injected water in the previous study (Chapter 4; also see Park et al., 2018). Heat transport experiments were conducted with two different heat sources at various background flow velocities. First, heat transport experiments using a resistor were performed to estimate the thermal properties of porous media, quantify the relationship between them, and derive the thermal dispersivity ratio. Then, heat transport experiments using injected water were conducted and analyzed by a numerical model to examine the influence of dispersivity ratio on the time evolution of thermal plume length and width. This chapter also considers the effect of injection rates and discusses the meanings of thermal dispersivity ratio for designing the GWHP systems.

5.2. Materials and methods

5.2.1. Experimental setup

The experimental system used in this chapter was initially designed to examine the effect of injected warm water (Chapter 4; Park et al., 2018) and is composed of an acrylic glass tank, two heat sources, and a data acquisition (DAQ) system (Figure 5.1). As the experimental design is described in detail in Chapter 4, this chapter explains only the changes that have been made.

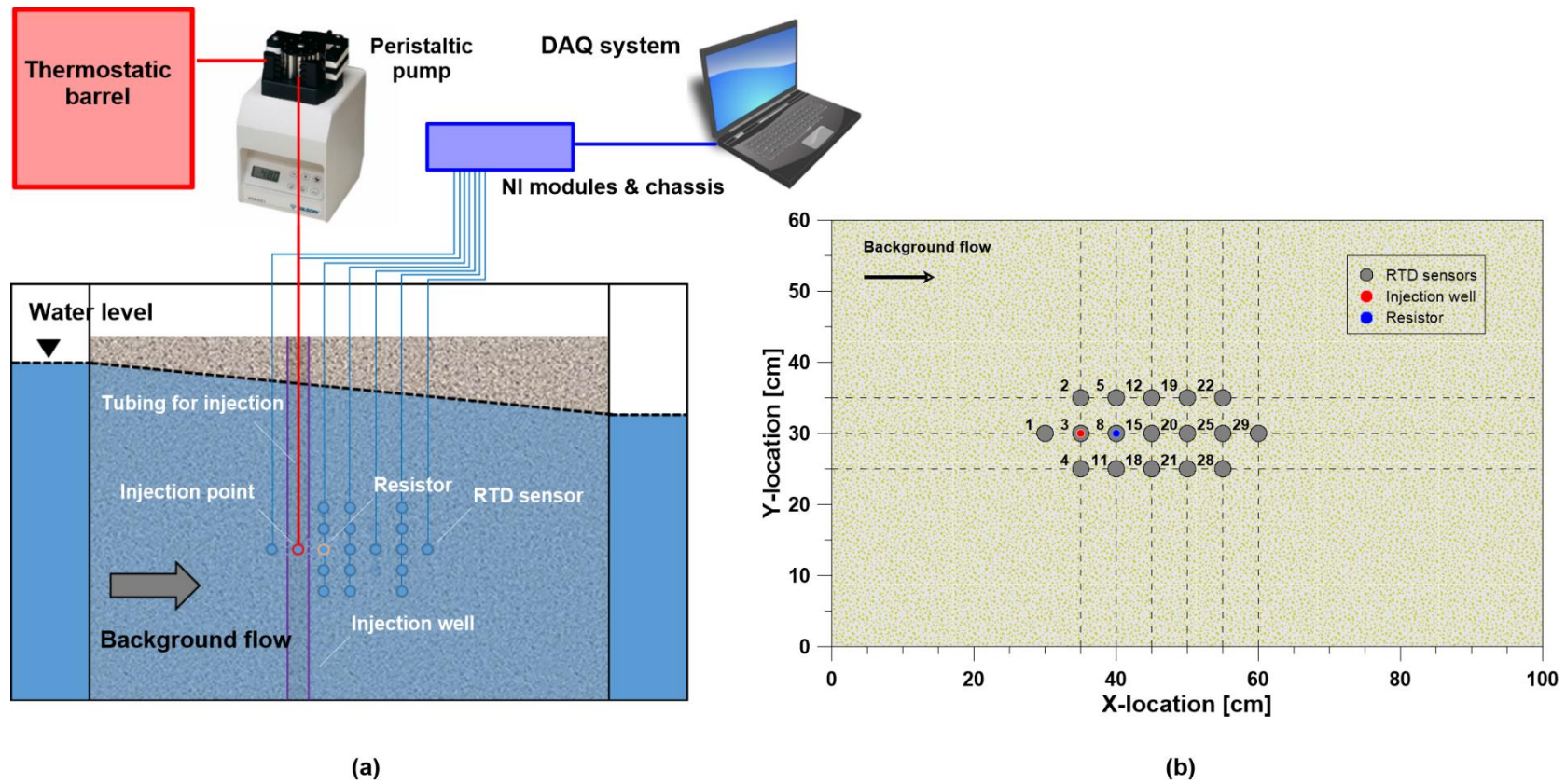


Figure 5.1. Laboratory experimental system for thermal tracer tests: (a) Schematic diagram of the overall design and (b) Horizontal location of heat sources and temperature sensors at a height of 30 cm.

Because RTD sensors at off-center locations did not show a significant change in temperature especially with increasing background water flow, their locations were adjusted (Figure 5.1b). Among 32 RTDs calibrated with the coefficients in Table 4.2, 29 RTD sensors were installed in fully-saturated porous media of sands S4 and S5, and the others were employed to measure the temperatures of ambient air, warm water in the thermostat, and background water. The flow rate of the peristaltic pump can be affected by the size of tubing as well as its rotational speed. Since the tubing used in Chapter 4 for warm water injection was torn by a lot of heat transport experiments, the injection rate of a new tubing was repeatedly measured at different rotational speeds and determined to be 50 ml/min at 20 rpm, which is comparable to the base rate of 48 ml/min at 18 rpm in Chapter 4.

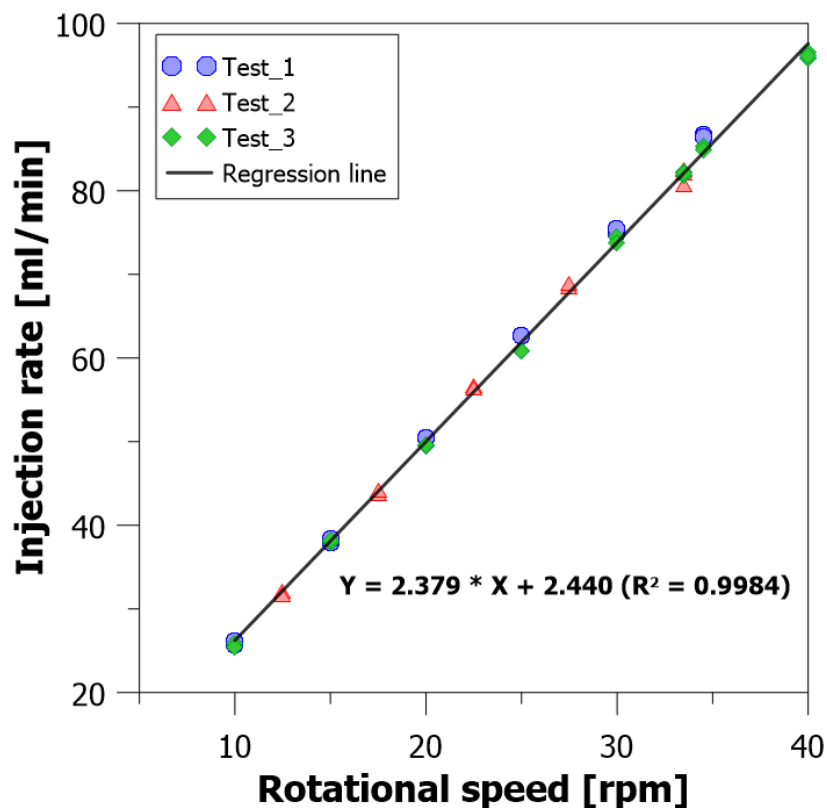


Figure 5.2. Injection rate of new tubing estimated at various rotational speeds of 10 to 40 rpm.

Despite efforts to avoid potential displacement of RTD sensors, it was observed to occur during the sand packing and the arrangement of the lead wires (Section 4.3.4). To minimize these errors at sensor location, two acrylic plates were designed to fix the top and bottom of acrylic tubes where RTD sensors were mounted (see Figure 5.3). With the sensors and heat sources fixed by the acrylic tubes and plates, the middle chamber was filled with saturated sands. After the sand packing process, the upper acrylic plate was removed, and the lead wires of the sensors and heat sources were arranged. The DAQ system consists of temperature sensors, NI modules and chassis, and DAQ softwares. Among the softwares, LabVIEW 2009 has been upgraded to LabVIEW 2015. A detailed description can be found in Section 4.2.3.

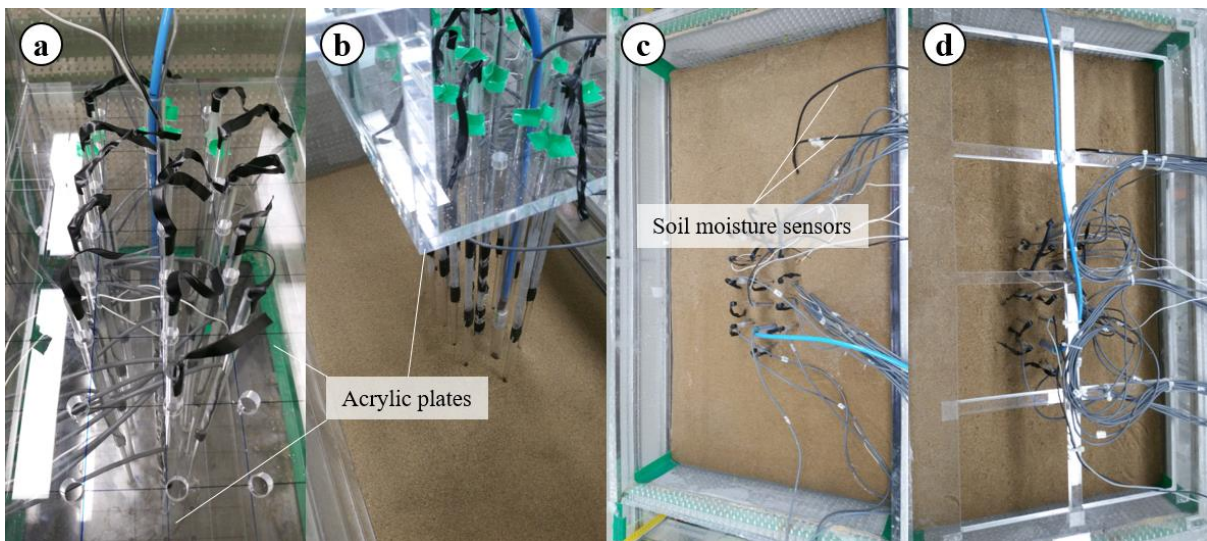


Figure 5.3. Images of experimental preparation. (a) Fixing sensors with acrylic tubes and plates, (b) Sand packing process, (c) Removing the upper plate after sand packing, and (d) Arranging the lead wires of RTD sensors and heat sources.

In Section 4.2.4, the physical properties of porous media were repeatedly measured, and their best estimates and uncertainties were estimated by uncertainty analysis (Appendix A; also see Taylor, 1997). Therefore, this section explains only those parts that are not described or that are different from Chapter 4. The sensitivity analysis in Chapter 3 indicates that hydrodynamic parameters play a significant role on the prediction of thermal plumes. In this sense, specific discharge (or Darcy velocity) and hydraulic gradient were measured repeatedly for 96 sand tank experiments, and the hydraulic conductivity was estimated to 2.032×10^{-3} m/s (2.2%) for sand S5 and 3.228×10^{-3} m/s (0.9%) for sand S4 (Figure 5.4). The porosity of sand S5 was estimated to be 0.331 (0.4%) by measuring the moisture contents in the experimental setup (Figure 5.3c), while that of sand S4 was derived to be 0.374 (0.2%) by measuring the dry sand volume and the bulk volume for 51 samples.

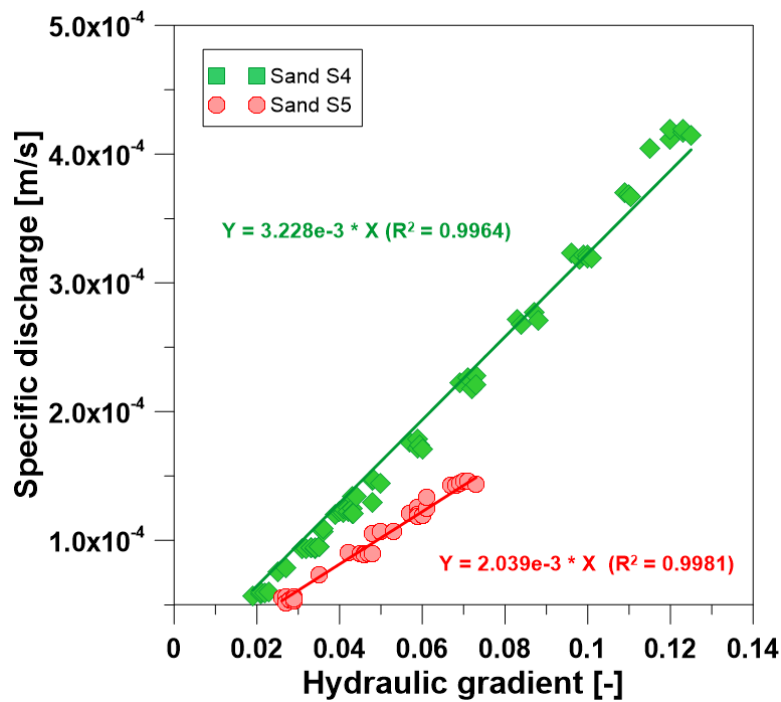


Figure 5.4. Hydrodynamic properties of coarse sands. The hydraulic conductivity values were estimated from the relationship between specific discharge and hydraulic gradient.

5.2.2. Laboratory-scale heat tracer tests

Heat transport experiments using a resistor as a heat source were conducted seven times to estimate the thermal conductivity and the volumetric heat capacity of coarse sands. A constant power of 4.230 W or 4.517 W was applied to the resistor, and the temporal variation in temperature was measured at 29 RTD sensors around the heat source. A total of 44 heat transport experiments using the resistor were also performed at various background flow velocities of 4.74–12.32 m/d for sand S5 and 8.13–36.75 m/d for sand S4. Because the time to reach a steady state is longer at a slower flow velocity, the power applied to the resistor was adjusted in the range of 3.426–4.517 W. Before/after all the experiments, the background water was kept flowing through the sand tank for several hours so that the temperature of the porous media was equal to the temperature of the background water.

To validate the numerical model and investigate the effect of thermal dispersivity ratio, heat transport experiments using injected warm water as a tracer were performed at four different flow velocities of 11.93, 21.21, 29.47, and 37.47 m/d for sand S4. The injection rate of 50 ml/min with 20 rpm was used for a base value, and additional injection rates of 26 and 75 ml/min with corresponding rotational speeds of 10 and 30 rpm were also considered in the experiments. The temperature change monitored at the injection point was not constant for all the experiments, but remained below 5°C.

5.2.3. Estimation of thermal properties

The resistor experiments were analyzed by analytical models to estimate the thermal properties of saturated porous media. The two models are the solutions to the differential HTE

in equation (4.6) for an infinite 3-D porous medium with/without a uniform flow in the x-direction. The CPS model defined as equation (4.12) was employed to derive the bulk thermal conductivity and volumetric heat capacity from the experimental results performed without background flow. As described in equation (4.9), the MCPS model was used to analyze the resistor experiments conducted at various background flows, and the thermal dispersion coefficients and thermal front velocities were estimated from the analysis results.

5.2.4. Heat transport modeling

The heat transport experiments using injected warm water as a tracer were analyzed by the 3-D numerical model developed in Chapter 4. As shown in Figure 5.5, the 3-D model domain constructed in FEFLOW[®] 5.3 (Diersch, 2005a) has the same dimensions as the laboratory experiments, and was discretized into rectangular elements with a mesh spacing of 0.002–0.004 m. The initial time step was set to be 10^{-9} d with the maximum time step of 10^{-4} d.

Figure 5.5 also illustrates the boundary conditions (BCs) for flow and heat transport applied to the numerical model. The initial hydraulic head was set to be 0.6 m all over the model domain. The head distribution was calculated by performing steady-state simulations where the observed water levels were reflected as constant-head BCs. The hydraulic gradient was in the range of 0.041–0.118 depending on the experimental conditions. The initial temperature for the entire domain was set equal to the background water temperature observed prior to the injection tests. Its temperature was also employed as a constant BC at the left boundary of the model where the background water flows in. The injection of warm water was represented by two BCs at the injection point, i.e., the average injection rate and the injection temperature measured in the experiments (see Figure 5.5). The numerical model was then validated by

performing transient flow and transport modeling and comparing the results with observations. The hydrogeological and thermal parameters used in the simulations are listed in Table 5.1.

Table 5.1. Hydrogeological and thermal parameters used for the developed numerical model. A percentage in parentheses indicates the relative uncertainty of the best estimate.

Parameters	Symbol	Unit	N4	Comment
Horizontal hydraulic conductivity	$K_{xx} = K_{yy}$	10^{-4} m/s	32.28 (1%)	Experiments
Vertical hydraulic conductivity	K_{zz}	10^{-4} m/s	3.228	Assumption
Specific yield	S_y	–	0.2	Default in FEFLOW; Johnson (1967)
Specific storage	S_s	1/m	0.0001	Default in FEFLOW; Anderson & Woessner (1992)
Porosity	n	–	0.3740 (0.2%)	Experiments
Volumetric heat capacity of water*	$\rho_w c_w$	10^6 J m ⁻³ K ⁻¹	4.184–4.173	NIST (2019)
Thermal conductivity of water*	λ_w	W m ⁻¹ K ⁻¹	0.590–0.602	NIST (2019)
Volumetric heat capacity of solid	$\rho_s c_s$	10^6 J m ⁻³ K ⁻¹	1.970 (4%)	Experiments
Thermal conductivity of solid	λ_s	W m ⁻¹ K ⁻¹	3.845 (2%)	Experiments
Longitudinal thermal dispersivity	β_L	10^{-3} m	2.278 (5%)	Experiments
Transverse thermal dispersivity	β_T	10^{-4} m	1.533 (6%)	Experiments

*Thermal properties of water depend on the temperature conditions (6–14°C) of the experiment, and they are referenced to NIST (2019).

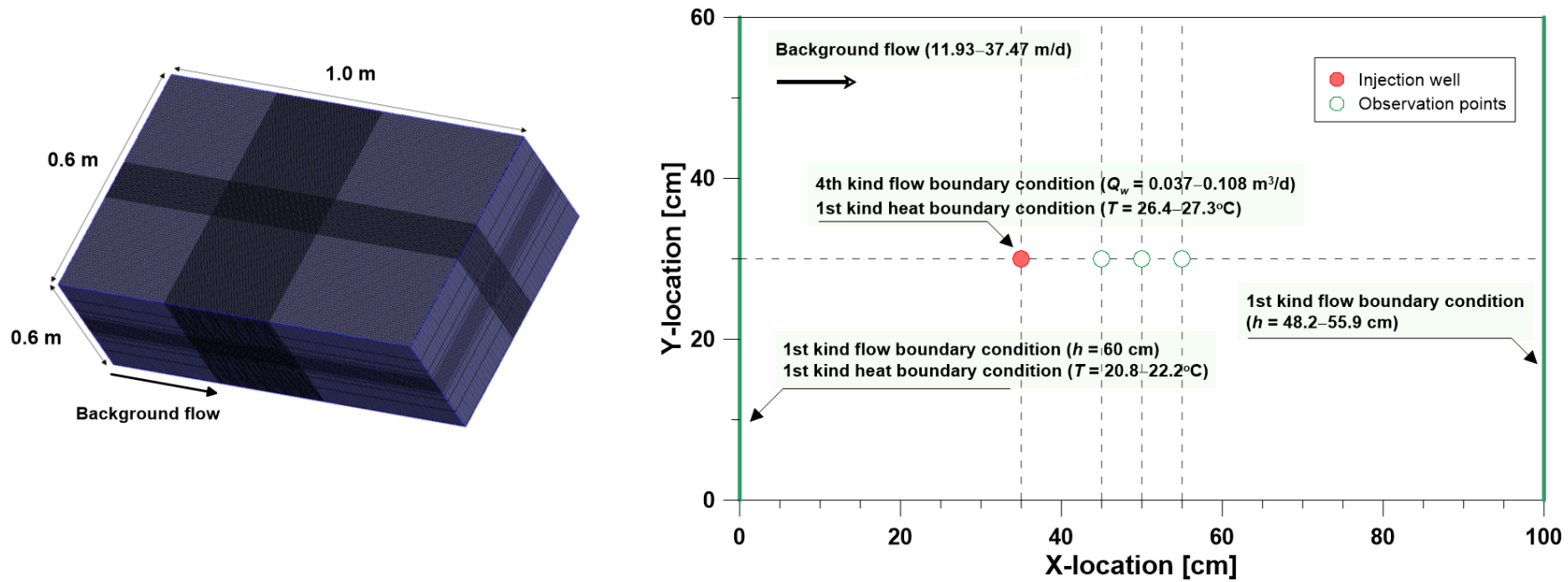


Figure 5.5. The 3-D finite element model developed in the previous work (Chapter 4) and its boundary conditions for the simulations of flow and heat transport.

Thermal dispersion is one of the significant physical mechanisms for investigating the heat propagation in saturated porous media. The lack of information and experimental data available on thermal dispersivity (Piga et al., 2017), however, leads to the use of default values in the simulators, especially the fixed thermal dispersivity ratio of 10. In this context, heat transport modeling using the validated model was performed with different dispersivity ratios of 1–10. The case simulations also took into account the estimated ratios in the previous studies (Rau et al., 2012a; Saeid et al., 2014), background flow velocities, and injection rates.

5.2.5. Parameter estimation

The quality of the fitness in the analytical and numerical modeling results was evaluated by two criteria of root mean square error (RMSE) and normalized root mean square error (NRMSE), defined as equations (4.14) and (4.15). The flow and transport regimes were quantified by Re (de Marsily, 1986) and Pe' (de Marsily, 1986; Anderson, 2005; Rau et al., 2014) given by equations (4.19) and (4.18). Details of the analysis procedure are described in Section 4.3.4.

The thermal plume dimensions in this study were determined based on the isotherm 1°C higher than the background water temperature. To analyze the effect of thermal dispersivity ratio, three variables were defined expressing the plume dimensions (see Figure 5.6). The definition of plume length basically followed that of Lo Russo et al. (2012), but was subdivided into plume length L_1 indicating the upstream propagation and plume length L_2 representing the downstream propagation. The plume length L_2 corresponds to the plume length of Piga et al. (2017). The plume width was defined as the maximum plume extent in the transverse direction to background water flow (Piga et al., 2017).

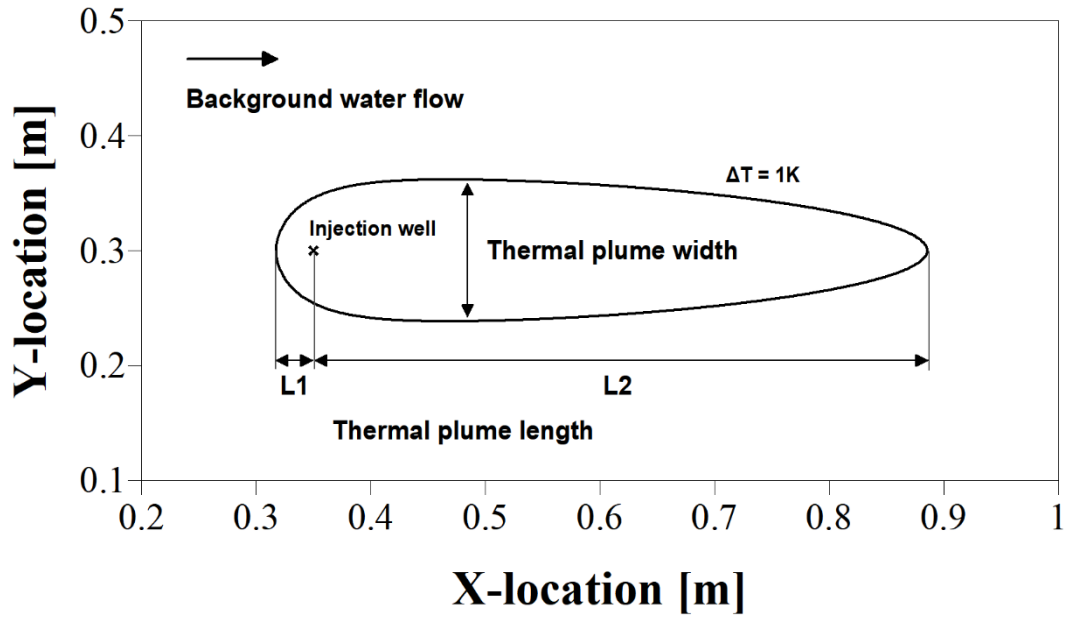


Figure 5.6. Thermal plume dimensions defined by the plume lengths $L1$ and $L2$, and the plume width. They are determined from the isotherm of $\Delta T = 1$ K.

5.3. Results

5.3.1. Heat transport experiments with the resistor

Heat transport experiments using the resistor as a heat source were conducted initially without background flow to estimate the thermal conductivity and volumetric heat capacity of the porous media. Figure 5.7 illustrates the temperature–time series data observed at the center and off-center locations with their best-fitted CPS model results. As shown in Figure 5.7, the model results are in good agreement with the observed temperature data. The thermal properties of the saturated sands and the corrected sensor locations were determined from the best fit satisfying the least RMSE. All the experiments were repeatedly performed and analyzed, and the average values of the estimates are shown in Tables 5.2 and 5.3 as the best estimates. For

sand S4, where the experiments were performed five times, the relative uncertainty of the best estimates was also expressed in parentheses as a percentage. The solid thermal properties were derived from the arithmetic and geometric mean models in equations (4.16) and (4.17). The thermal conductivity and volumetric heat capacity of solids for sand S5 were estimated to be on average $3.826 \text{ W m}^{-1} \text{ K}^{-1}$ and $1.890 \times 10^6 \text{ J m}^{-3} \text{ K}^{-1}$, and those for sand S4 on average $3.845 \text{ W m}^{-1} \text{ K}^{-1}$ and $1.970 \times 10^6 \text{ J m}^{-3} \text{ K}^{-1}$. As can be seen in Tables 5.2 and 5.3, the thermal conductivity values estimated for the two sands are high, so that laboratory XRD analyses of the sand samples were conducted to confirm their chemical composition (Section 4.2.4). The results represent the high quartz contents of 75.6% (sand S4) and 68.3% (sand S5). Based on the quartz contents and the reference values for dry sand and quartz (Balland & Arp, 2005; Stauffer et al., 2013), the possible range of thermal conductivity was calculated from the geometric mean model in equation (4.17). As shown in Figure 5.8, the values estimated from heat transport experiments for both sands are within the calculated possible range for thermal conductivity, indicating that the high thermal conductivity value can originate from the high quartz content.

Heat transport experiments using a resistor were also conducted at various background flow velocities (Darcy velocities of 4.74 to 36.75 m/d) to estimate the thermal dispersion coefficients and the thermal front velocities. Figure 5.9 illustrates observed temperature–time series data and their best-fitted MCPS models for three observation points ($r' = 0.048, 0.096, \text{ and } 0.139$) at Darcy velocities of 10.44 m/d and 35.85 m/d. Compared with a good example in Figure 5.9a with the smallest NRMSE, Figure 5.9b with the largest NRMSE shows a difference between the observed and modeled temperatures, especially at the beginning of the plateau. The analytical models, however, are successful in reproducing the observed temperature

breakthrough curves in that R^2 values are 0.9970 or higher for all the experiments.

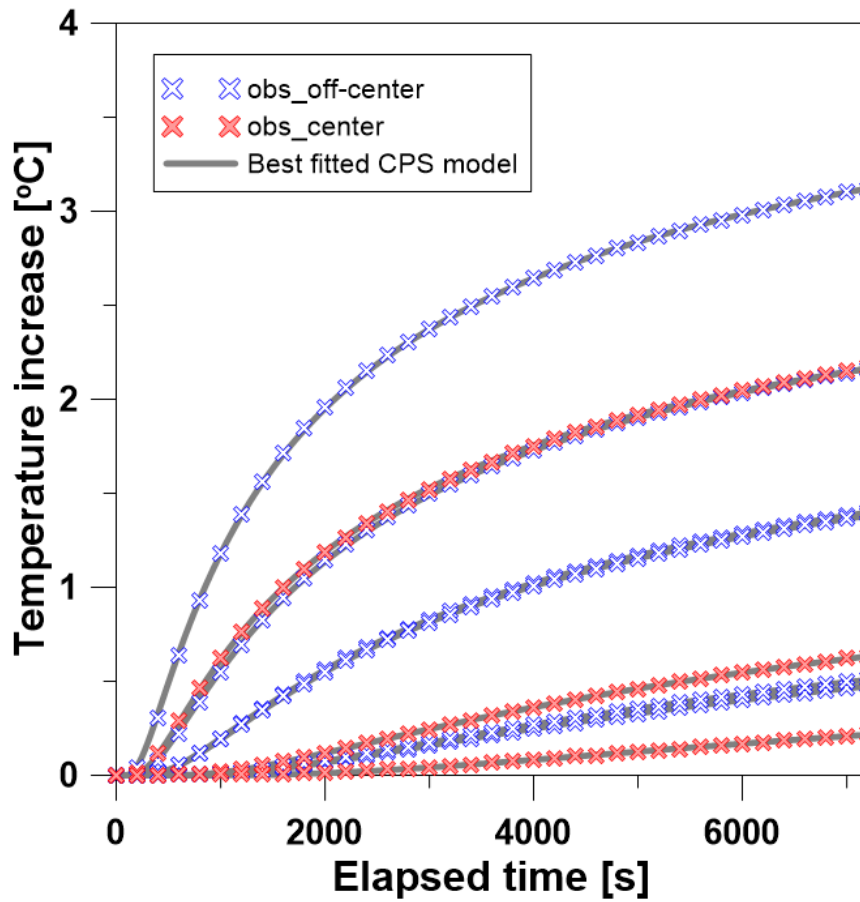


Figure 5.7. Temperature–time series data observed at the center and off-center locations (cross symbol), and the corresponding best-fitted CPS model results (solid line).

Table 5.2. Thermal properties of sand S5 and sensor locations estimated from the best-fitted CPS model. A percentage in parentheses indicates the uncertainty of the best estimate.

S5	RTD 5	RTD 12	RTD 19	RTD 15	RTD 20	RTD 25	RTD 11	RTD 18	RTD 21
r' [m]	0.053	0.067	0.107	0.051	0.096	0.138	0.042	0.068	0.106
$\rho_s c_s$ [J m ⁻³ K ⁻¹]	1,810,615	1,914,451	2,001,083	2,043,365	2,010,683	1,898,575	1,985,147	1,856,645	1,786,276
λ_s [W m ⁻¹ K ⁻¹]	3.602	3.759	3.920	4.044	3.722	4.451	3.640	3.754	3.708
RMSE	0.005	0.003	0.004	0.006	0.003	0.006	0.006	0.003	0.004
NRMSE	0.002	0.002	0.008	0.003	0.005	0.022	0.002	0.002	0.008

Table 5.3. Thermal properties of sand S4 and sensor locations estimated from the best-fitted CPS model. A percentage in parentheses indicates the uncertainty of the best estimate.

S4	RTD 5	RTD 12	RTD 19	RTD 15	RTD 20	RTD 25	RTD 11	RTD 18	RTD 21
r' [m]	0.055 (1%)	0.072 (0.5%)	0.110 (1%)	0.048 (1%)	0.096 (0.2%)	0.139 (1%)	0.037 (0.5%)	0.062 (1%)	0.104 (1%)
$\rho_s c_s$ [$\text{J m}^{-3} \text{K}^{-1}$]	1,899,894 (3%)	1,905,061 (4%)	2,008,958 (5%)	2,005,283 (4%)	2,047,889 (3%)	1,937,789 (4%)	2,060,315 (3%)	1,972,022 (4%)	1,912,148 (4%)
λ_s [$\text{W m}^{-1} \text{K}^{-1}$]	3.867 (2%)	3.909 (2%)	3.594 (2%)	4.167 (2%)	3.814 (3%)	3.271 (3%)	4.060 (2%)	3.999 (1%)	3.756 (2%)
RMSE	0.004	0.005	0.003	0.005	0.003	0.003	0.007	0.005	0.003
NRMSE	0.002	0.004	0.006	0.002	0.004	0.013	0.002	0.003	0.006

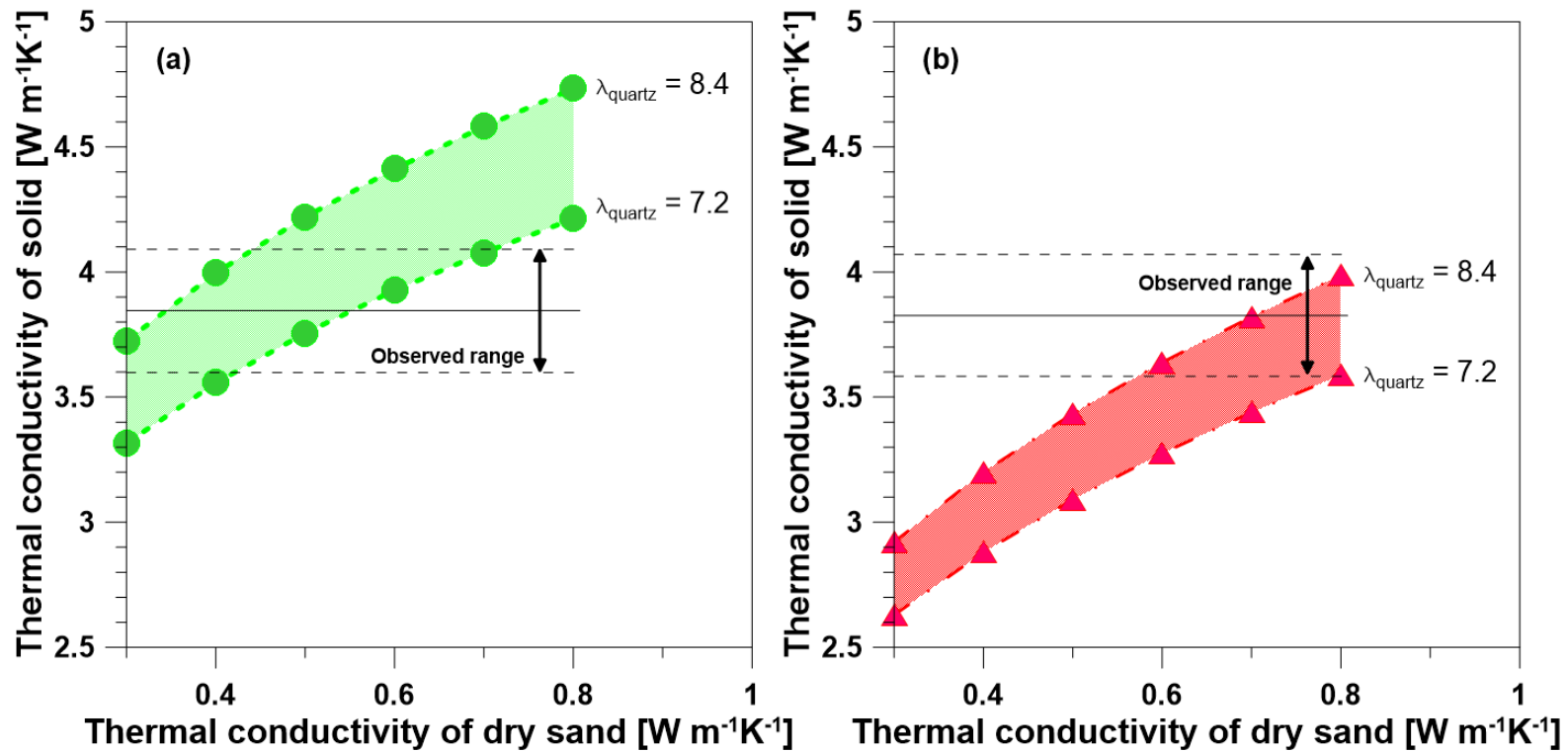


Figure 5.8. Observed and calculated ranges of thermal conductivity for (a) sand S4 and (b) sand S5. The black dashed lines indicate the thermal conductivity range estimated from heat tracer tests and the black solid line represents their average value. The colored region shows the possible range calculated from the reference range for thermal conductivity of dry sand/quartz (mineral): 0.3–0.8 $\text{W m}^{-1} \text{K}^{-1}$ (Stauffer et al., 2013) /7.2–8.4 $\text{W m}^{-1} \text{K}^{-1}$ (Balland & Arp, 2005).

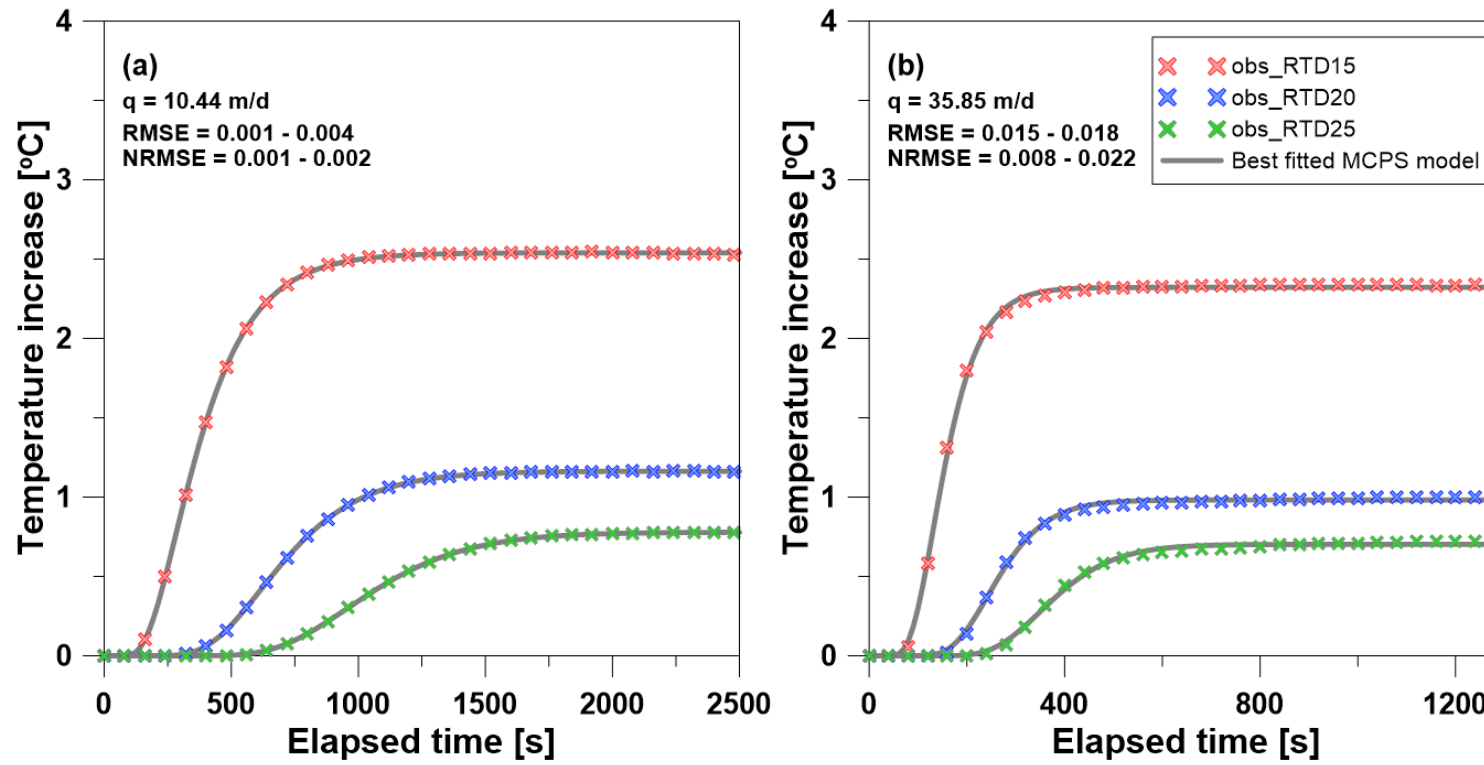


Figure 5.9. Observed temperature–time series data and their best-fitted MCPS models for three observation points ($r' = 0.0479, 0.0961,$ and 0.1390) at a Darcy velocity of (a) 10.44 m/d and (b) 35.85 m/d.

Figures 5.10 and 5.11 show the relationship between the thermal dispersion coefficients and the thermal front velocities, estimated for sands S5 and S4. As shown in Figure 5.10, it was observed for sand S5 that the thermal dispersion coefficients increase in the longitudinal direction but decrease in the transverse direction. Although heat transport experiments for sand S4 were also performed in the conduction dominant regime ($Pe' < 0.7$), it was found that both longitudinal and transverse thermal dispersion coefficients increase with the flow velocities (Figure 5.11). To express quantitatively the relationship between them and to derive thermal dispersivity values, a simple linear regression method was applied. The linear regression equation for sand S5 does not represent a clear tendency ($R^2 < 0.3$), while that for sand S4 shows a distinct increasing trend with R^2 values of 0.7890 in the longitudinal and 0.7593 in the transverse directions (see black solid lines in Figures 5.10 and 5.11). From the regression models, the longitudinal and transverse thermal dispersivity values for sand S4 were estimated to be 2.278×10^{-3} m (5.2%) and 1.533×10^{-3} m (5.6%), respectively. There is, however, the scatter in the relationships between the thermal dispersion coefficients and the thermal front velocities, which makes it difficult to identify their relationships and derive the thermal dispersivity values, especially for sand S5. This will be discussed in Section 5.4.1.

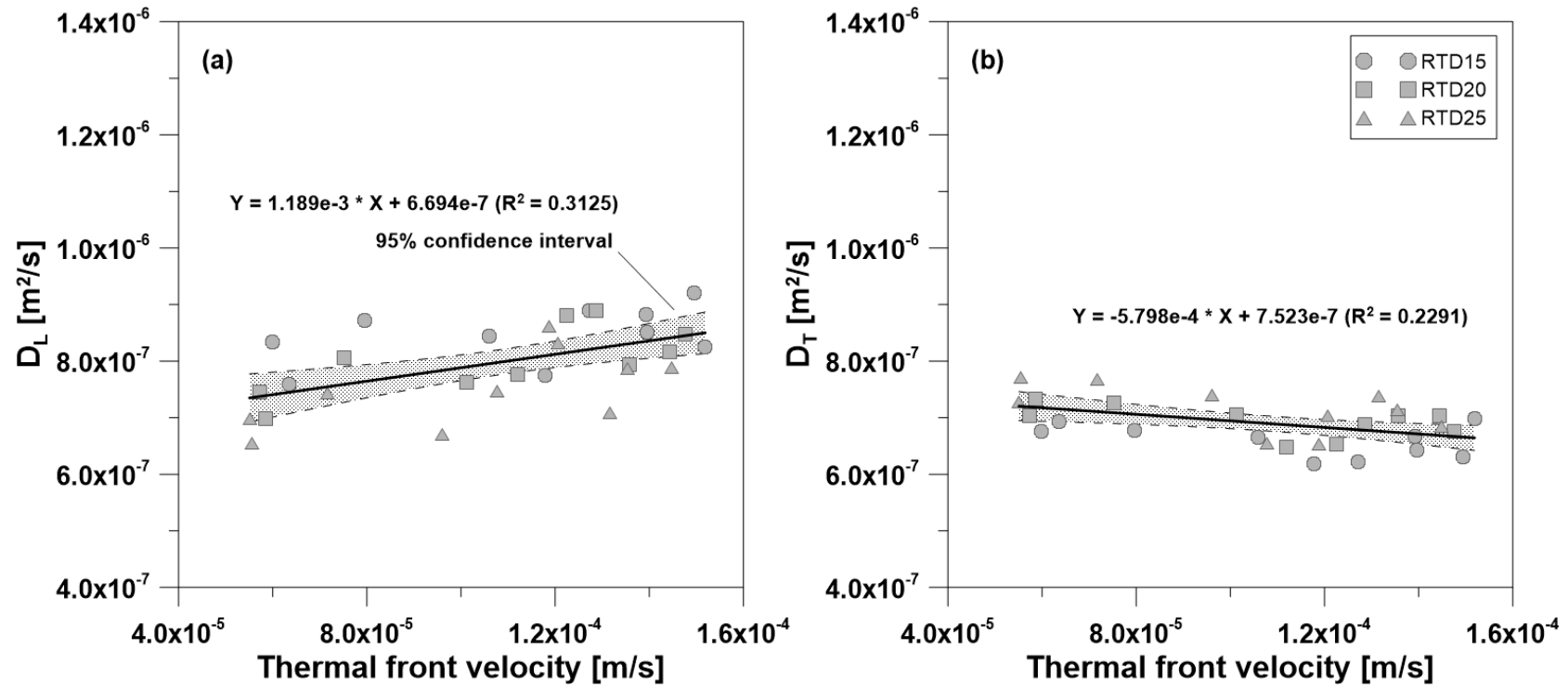


Figure 5.10. The relationship between the thermal dispersion coefficients and the thermal front velocities for sand S5, estimated from the best-fitted MCPS models: (a) longitudinal and (b) transverse directions. The black solid lines represent the linear regression lines for the relationships, and the gray shaded regions indicate their 95% confidence interval.

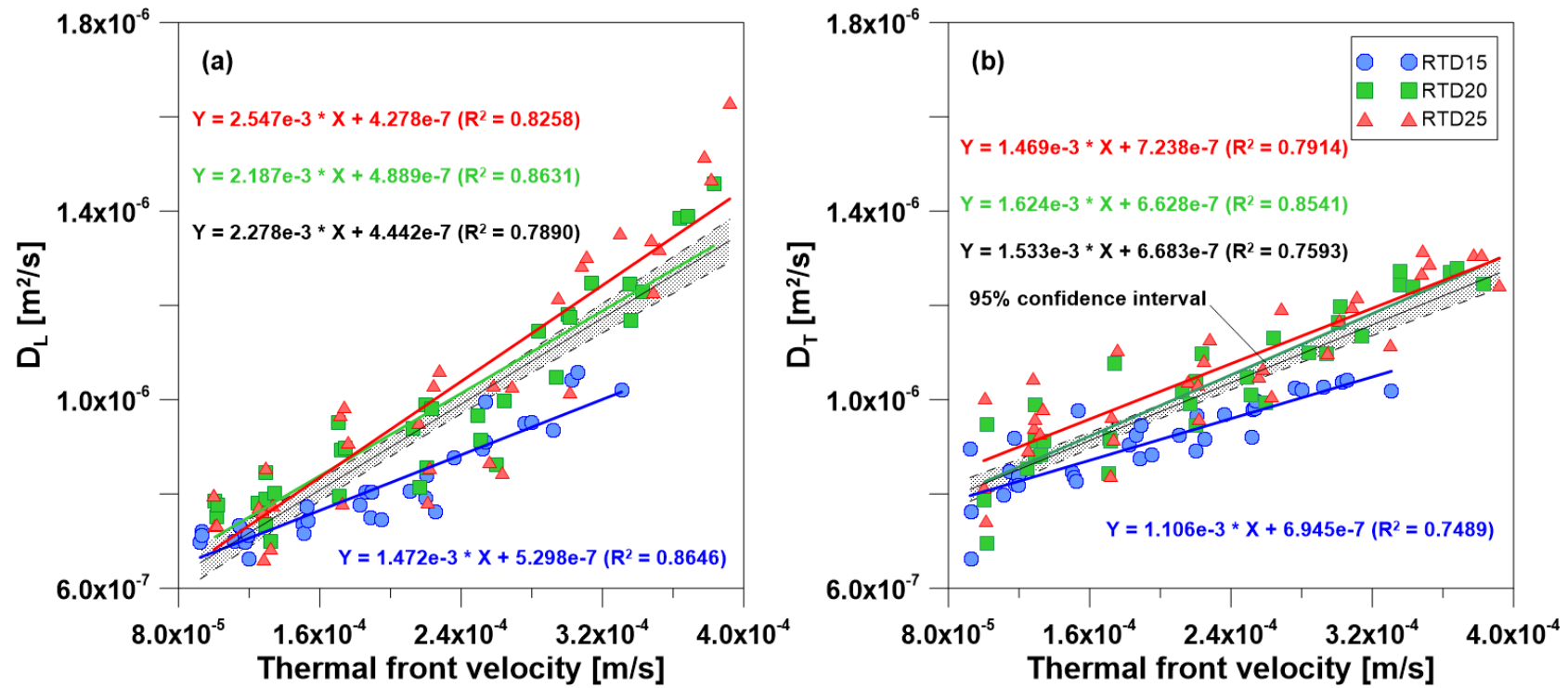


Figure 5.11. The relationship between the thermal dispersion coefficients and the thermal front velocities for sand S4, estimated from the best-fitted MCPS models: (a) longitudinal and (b) transverse directions. The solid lines represent the linear regression lines for the relationships, and the gray shaded regions indicate their 95% confidence interval.

5.3.2. Heat transport experiments with injected water

Heat transport experiments using injected warm water as a heat source were performed to validate the 3-D numerical model and to investigate the influence of the thermal dispersivity ratio in designing the GWHP systems. Figure 5.12 represents the temperature–time series for both the observed data and the numerical model at $r' = 0.1390$ m with Darcy velocities of 11.93 m/d and 29.47 m/d. Despite the deviation at the beginning and end of the temperature breakthrough curves, it was found that the model successfully reproduced the observed data in terms of $R^2 > 0.9905$.

Figure 5.13 shows the thermal plume extensions for steady-state simulations conducted with various thermal dispersivity ratios at two different Darcy velocities of 11.93 m/d and 29.47 m/d. It is obvious that the dimensions of the thermal plumes increase with the thermal dispersivity ratio. In addition, the intensity of the change was found to be larger as the background flow velocity is faster. The gray isotherms in Figure 5.13a represent the projection of the isotherms in Figure 5.13b, which was observed at the faster background flow velocity. A notable thing can be found when comparing the results at different background flow velocities (see Figure 5.13a). As the background flow velocity increases, the thermal plume width decreases, but the thermal plume length can increase or decrease depending on the thermal dispersivity ratio.

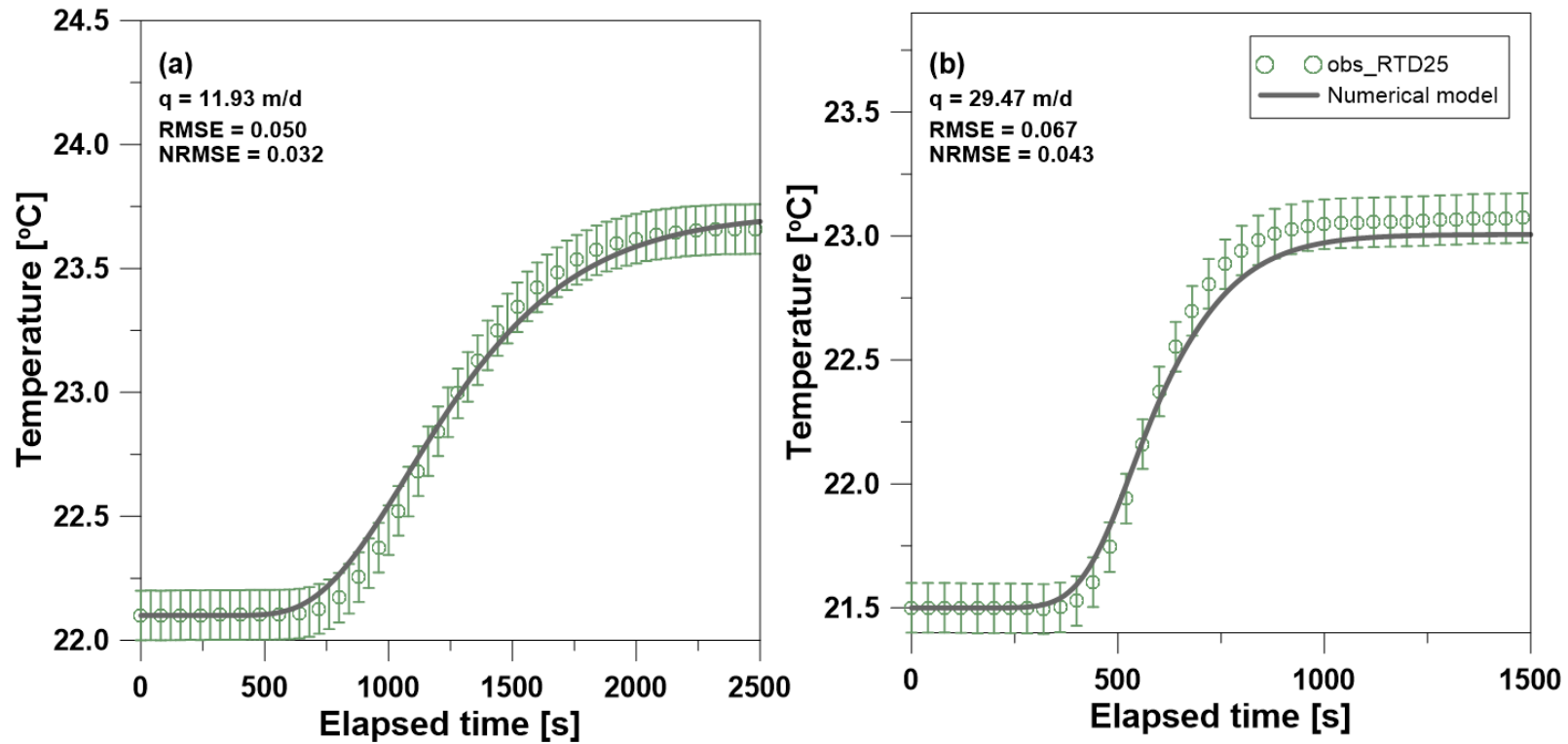


Figure 5.12. Temperature–time series for the observed data (green circle) and the numerical model (grey solid line) at $r' = 0.1390$ m with a Darcy velocity of (a) 11.93 m/d and (b) 29.47 m/d. The vertical bar indicates the uncertainty of observed temperature data, which can result from the accuracy of RTD sensors ($\pm 0.1^\circ\text{C}$).

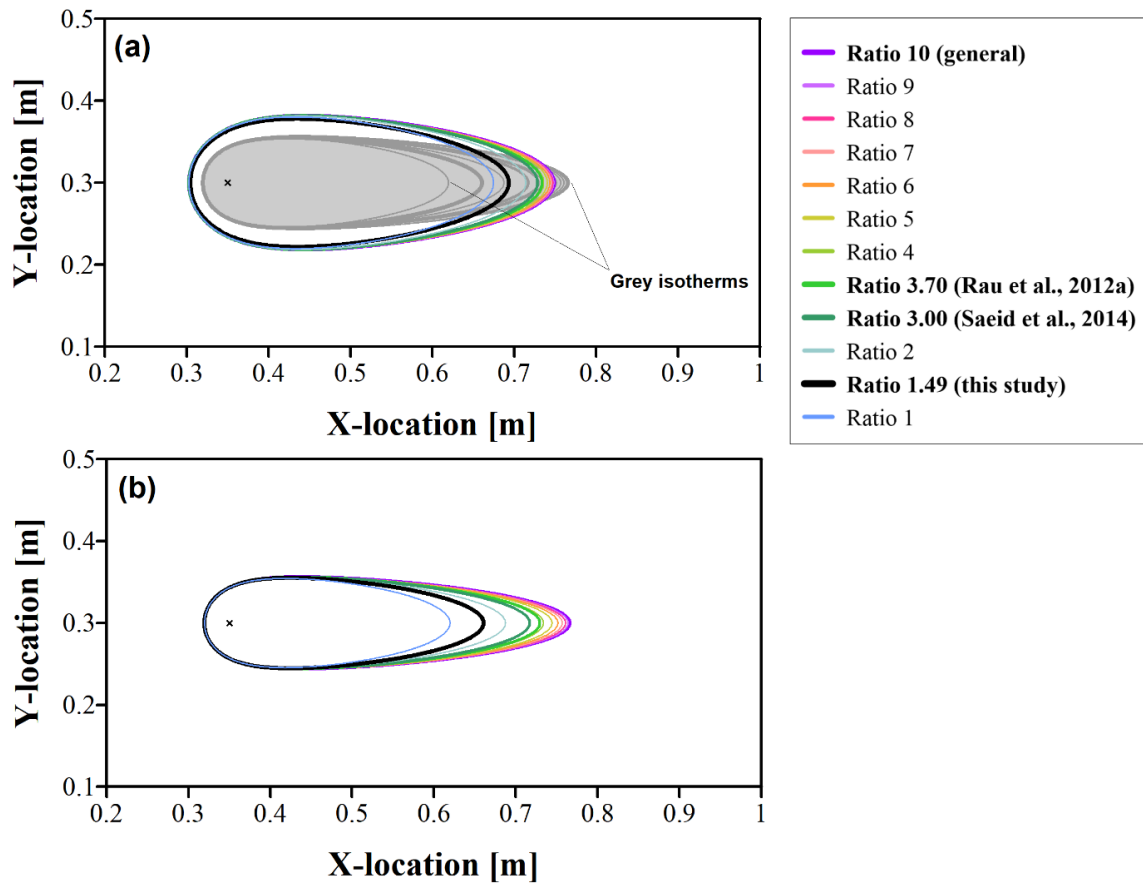


Figure 5.13. Thermal plume extensions for steady-state simulations performed with different thermal dispersivity ratios at a Darcy velocity of (a) 11.93 m/d and (b) 29.47 m/d. Each thermal plume was drawn based on the isotherm 1°C higher than the background water temperature. The grey isotherms in Figure 5.13a represent the projection of the isotherms in Figure 5.13b for comparison.

As a result of the transient simulations, Figure 5.14 displays the temporal variation of the thermal plume lengths with different thermal dispersivity ratios ranging from 1 to 10 at the Darcy velocity of 29.47 m/d. It was difficult to identify the difference in the thermal plume length L_1 calculated from the isotherm of $\Delta T = 1^\circ\text{C}$. Because the plume length L_1 can be a reference to avoid the thermal recycling between pumping and injection wells and ensure the system efficiency, a more stringent criterion of $\Delta T = 0.1^\circ\text{C}$ was applied to calculate the plume length L_1 . As shown in Figure 5.14, it is obvious that the thermal dispersivity ratio affects the thermal plume dimension parallel to the background flow direction. Its influence, however, is observed to be different with space and time. The effect of the thermal dispersivity ratio is stronger in the downstream direction than the upstream direction, and in the steady state than the transient. Figure 5.15 illustrates the temporal variation of the thermal plume widths with different thermal dispersivity ratios at two Darcy velocities of (a) 11.93 m/d and (b) 29.47 m/d. It was confirmed that the thermal dispersivity ratio also affects the thermal plume dimension perpendicular to the background flow direction, especially for the steady state. Its influence on the plume width, however, is much weaker than that on the plume length L_2 . As the background flow velocity increases, the thermal plume width decreases noticeably but the effect of the dispersivity ratio increases only marginally (Figure 5.15).

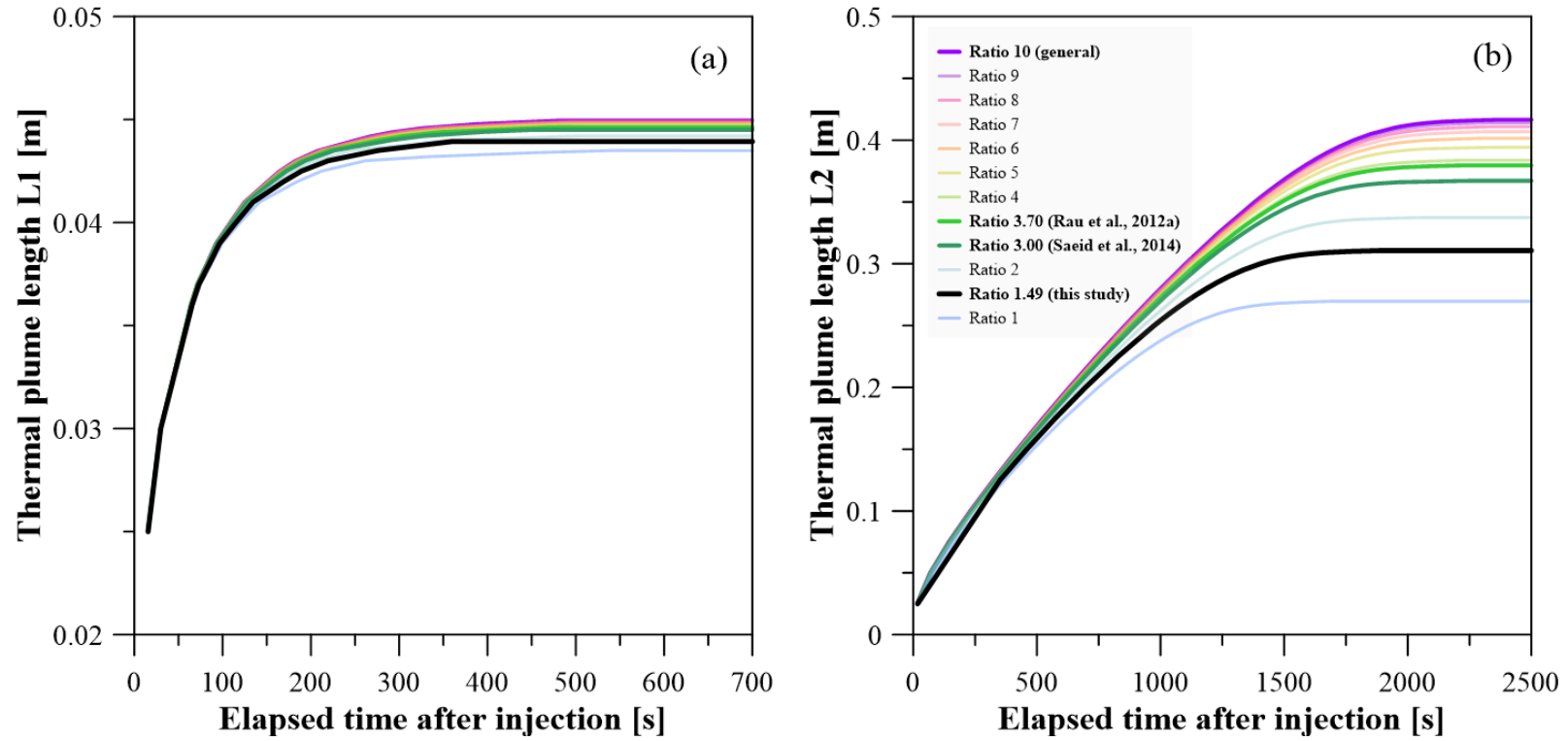


Figure 5.14. Temporal variation of the thermal plume lengths of (a) L1 and (b) L2 with different thermal dispersivity ratios ranging from 1 to 10 at a Darcy velocity of 29.47 m/d.

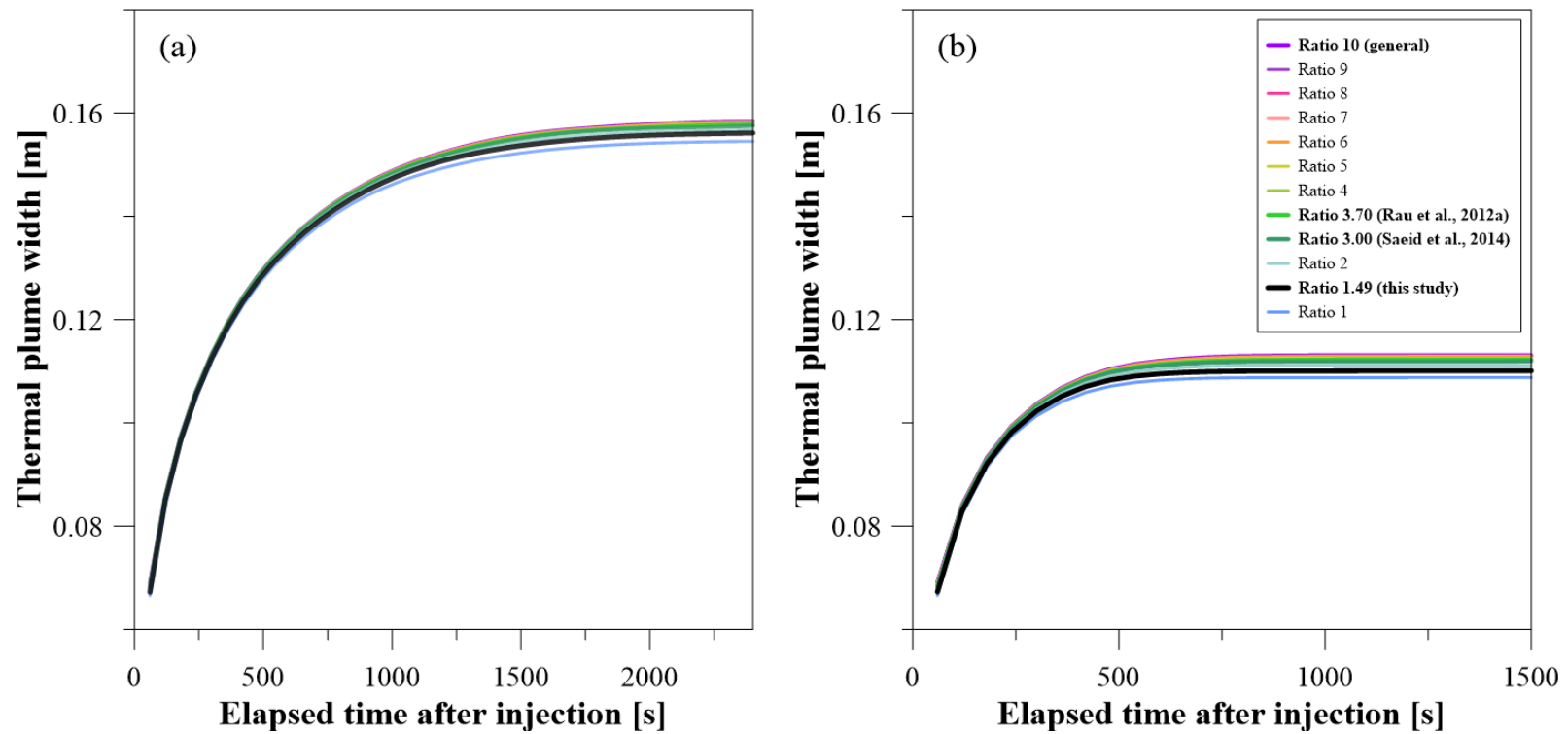


Figure 5.15. Temporal variation of the thermal plume widths with different thermal dispersivity ratios at a Darcy velocity of (a) 11.93 m/d and (b) 29.47 m/d.

5.4. Discussions

5.4.1. Thermal dispersion and flow velocity

The relationship between the thermal dispersion coefficients and the thermal front velocities represented a distinct increasing trend for sand S4, but there was no clear tendency for sand S5. As shown in Figures 5.10 and 5.11, the scatter makes it difficult to quantify their relationship, especially for low flow velocities. This has also been observed in the previous studies (Kunii & Smith, 1961; Park et al., 2018; Rau et al., 2012a; Yagi et al., 1960; Yuan et al., 1991). There can be several reasons for the scatter. The first reason can be found in the transport regime. Although the hydraulic gradient between the chambers on the side was kept as high as possible (Figure 5.1a), it was found that all the experiments were performed in the conduction dominant regime ($Pe^t < 0.2$ for sand S5 and $Pe^t < 0.7$ for sand S4). In the thermal regime represented by very low Pe^t , the thermal diffusivity (first term in equation (4.13)) takes up to 89% of the longitudinal thermal dispersion coefficient, and is up to 8.1 times higher than the mechanical dispersion (Figure 5.16). Thus, the dominance of conductive heat transport makes the contribution of background flow to the dispersion coefficient insignificant for $q < 1.50 \times 10^{-4}$ m/s. This partly explains why it is difficult to identify the relation between the thermal dispersion coefficients and the thermal front velocities for sand S5 ($R^2 < 0.3$, see Figure 5.10), in which all experiments were performed under very slow flow condition ($Pe^t < 0.2$).

Figure 5.17 shows the variation of thermal front velocity estimated from three observation points as background flow increases. For $q < 1.50 \times 10^{-4}$ m/s, the velocity difference among RTD sensors are less than 13% and 11% for sands S5 and S4 compared to the respective maximum velocity. This difference in the thermal front velocity can change the longitudinal dispersion coefficient to less than 4%, which can not account for the scatter in the dispersion

coefficient. As listed in Tables 5.2 and 5.3, the thermal conductivity and volumetric heat capacity of coarse sands S5 and S4 indicate spatial heterogeneity. The thermal diffusivity (first term in equation (4.13)) calculated from the bulk thermal properties varies up to 13% among RTD15, RTD20, and RTD25, and this can affect the dispersion coefficient in the longitudinal direction by up to 11% and 10% for S5 and S4 sands. Considering the variation in the longitudinal dispersion coefficient of 5–21% (S5) and 4–19% (S4), the heterogeneity of the thermal properties can be a main reason for the scatter in the dispersion–velocity relationship especially for low flow velocity. These explanations more clarify the interpretation by Park et al. (2018) for heat tracer tests in a saturated porous medium with homogeneous but different textured materials ($U = 1.36$ and $d_{50} = 1.28$ mm) and low flow ($Pe^t < 1$), and can be partly supported by the fact that a more pronounced trend is observed with higher R^2 values when the relationship is analyzed by observation points (see Figure 5.11).

For $q > 1.50 \times 10^{-4}$ m/s (= 12.96 m/d) where thermal diffusion and mechanical dispersion are comparable, the spatial variability of thermal properties alone can not explain the increasing deviation of the thermal dispersion coefficients among temperature measurement points with increasing background flows (see Figure 5.11). As can be seen in Figure 5.17b, the difference in thermal front velocity increases even at a single location as well as among observation points. This result indicates that the velocity field may not be homogeneous. Rau et al. (2012b) experimentally demonstrated that a nonuniform flow field occurs even in a small-scale experiment (0.96 m \times 0.96 m \times 0.4 m) with homogeneous natural materials ($U = 1.68$ and $d_{50} = 2$ mm) under a transition regime ($Pe^t < 0.7$). This flow field makes heat transport inhomogeneous in flow direction, resulting in lateral temperature gradients which is further enhanced with increasing flow velocity (see Rau et al., 2012b). This can be a possible

explanation for the spatial temperature variability found in a more complex shallow aquifer near Han river with the heterogeneous distribution of hydraulic conductivity (Kaown et al., 2018). In recent years, numerical studies at the streambed scales show that lateral heat transport can significantly affect the temperature-based specific discharge estimation (Ferguson & Bense, 2011; Schornberg et al., 2010). As Rau et al. (2012b) further commented, the flow field nonuniformity and lateral heat conduction stemming from the small-scale heterogeneity of permeability can violate the underlying assumptions of the uniform flow field and plume fringe of MCPS model (equation (4.9)), and this leads to the scatter in the dispersion-velocity relation especially for $q > 1.50 \times 10^{-4}$ m/s (Figure 5.11).

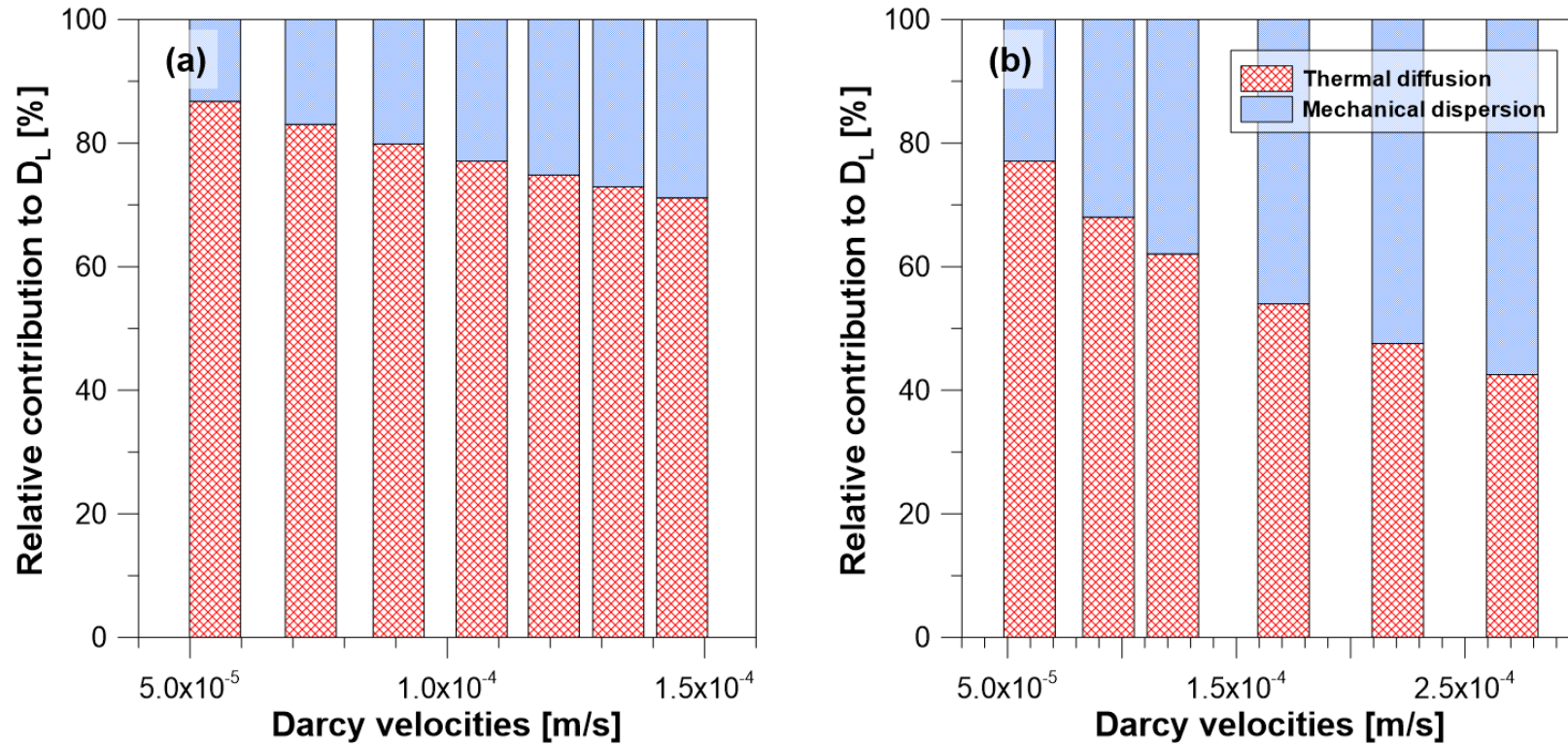


Figure 5.16. Relative contribution of thermal diffusion and mechanical dispersion to the longitudinal dispersion coefficient for (a) S5 and (b) S4 sands.

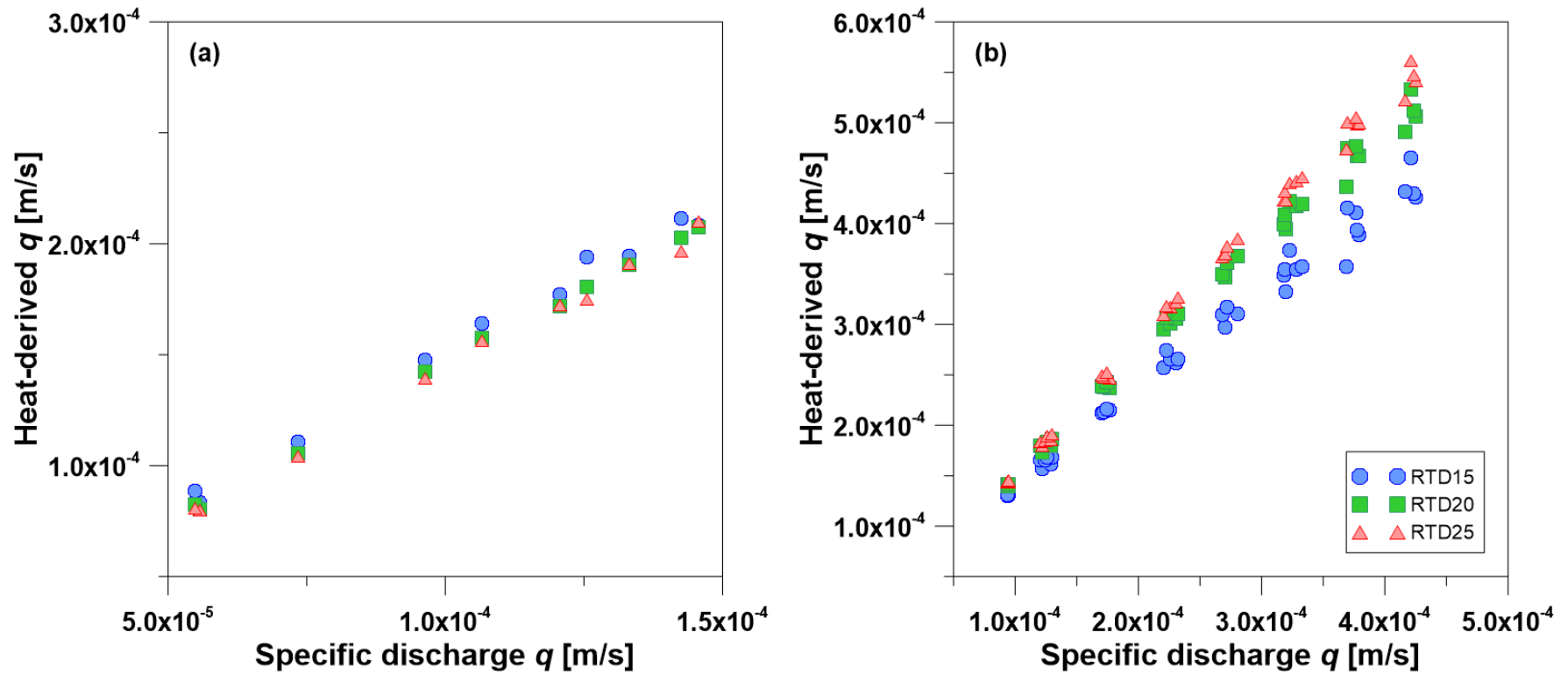


Figure 5.17. Variation of thermal front velocity with increasing background flow velocity for coarse sands (a) S5 and (b) S4.

The ratio between longitudinal and transverse thermal dispersivity values, in general, is assumed to be 10 in the simulation of heat transport (Alcaraz et al., 2016; Hopmans et al., 2002; Kim et al., 2018; Lo Russo & Civita, 2009; Lo Russo et al., 2012; Lo Russo et al., 2018; Molson et al., 1992; Park et al., 2015a; Park et al., 2015b; Piga et al., 2017; Pophillat et al., 2018; Smith & Chapman, 1983; Su et al., 2004; Tu et al., 2019). The different values of thermal dispersivity ratio found in the literature (cf., 4.00 in Andrews & Anderson (1979), 2.13 in Park et al. (2018), 3.70 in Rau et al. (2012a), 3.00 in Saeid et al. (2014)), however, indicate that such an assumption can be violated. As shown in Figure 5.11, the thermal dispersivity values estimated by the linear regression models represent the thermal dispersivity ratios of 1.33–1.73, comparable to the values of the previous study (cf. 1.48–2.13 in Park et al. (2018)). These results confirm the previous finding that the thermal dispersivity ratio may be different from the value of 10 used in commercial software packages or commonly assumed for heat transport (Section 4.5.1; Park et al., 2018). The impacts of such differences on the thermal plume propagation and their implications will be discussed in Section 5.4.2.

5.4.2. Effects of thermal dispersivity ratio on thermal plume propagation

As shown in Figure 5.13, an increase in the thermal dispersivity ratio leads to an increase in the thermal plume dimension. This is relevant to the influence of transverse thermal dispersion on the thermal plume propagation. For steady-state conditions, the transverse dispersion is dominant over the longitudinal dispersion (Alcaraz et al., 2016; Metzger et al., 2004; Molina-Giraldo et al., 2011). This results in heat dissipation in the transverse direction to the background flow, reducing the dimension of the thermal plume. Hence, the modeling results for the general value of 10 can overestimate the thermal plume extension under steady-state

conditions in comparison to the dispersivity ratios reported in the literature (Figure 5.13).

The groundwater flow is closely related to the hydrodynamic parameters and has a great influence on the thermal plume propagation (Lo Russo et al., 2012). A recent study also confirms that the higher groundwater flow velocity causes an increase in the plume length but a decrease in the plume width (Piga et al., 2017). As shown in Figure 5.13a, however, the thermal plume length L_2 does not always increase for all dispersivity ratios. It is noteworthy that the plume length L_2 decreases with the increasing background flow velocity if the dispersivity ratio is less than 5. A possible explanation is that a sufficiently small dispersivity ratio makes the transverse dispersion still prevail over the other transport processes although the increase in the background flow velocity leads to the increase in both advection and dispersion. Therefore, the enhanced heat spreading in the transverse direction results in a shorter plume length.

As can be seen in Figures 5.14 and 5.15, the impacts of thermal dispersivity ratio on thermal plumes can vary depending on the thermal state (transient or steady state) of the system. For early transient times, the thermal plume dimension varies little with the dispersivity ratio. On approaching the steady-state condition, the difference in the plume extensions dramatically increases, especially in the plume length L_2 (Figure 5.14b). This is attributed to the fact that the importance of longitudinal and transverse dispersivity values is time dependent, as demonstrated by the relative sensitivities as a function of time (Metzger et al., 2004; Molina-Giraldo et al., 2011). Therefore, using a fixed value of 10 as a thermal dispersivity ratio can overestimate the thermal plume propagation, especially in long-term simulations, vital to reduce thermal risks and to ensure the efficiency and sustainability of the GWHP systems.

Figures 5.14 and 5.15 also show that the influence of the thermal dispersivity ratio is not

isotropic. This can be related to the anisotropic velocity field caused by injected water and background flow. In a real system, heterogeneous thermal properties and nonuniform flow field can affect the temperature distribution, and hence may complicate the spatially variable effect of the dispersivity ratio. As depicted in Figures 5.14 and 5.15, its effect is smallest in the upstream direction while largest in the downstream propagation of thermal plumes. This suggests that the thermal dispersivity ratio has an important role in assessing the environmental impacts of the GWHP systems, which can impair the sustainable use of groundwater in the downstream regions, such as drinking water, water curtain cultivation, and space heating and cooling.

The injected water in the GWHP system increases the flow velocity and thus makes the mechanical thermal dispersion more important in the heat-transport mechanism (Chapters 2 and 4; also see Park et al., 2015a; Park et al., 2018). To investigate the influence of injection on the significance of the thermal dispersivity ratio, numerical simulations were also conducted with different injection rates of 26–75 ml/min. Figure 5.18 show that the plume length L_1 and the plume width increase with injection rates, matching well with the previous results (Piga et al., 2017), but the effect of dispersivity ratio hardly changes and is small enough to be neglected (less than 6% change). As shown in Figure 5.18b, however, the dispersivity ratio can have a greater influence on the plume length L_2 with the higher injection rates, indicating that it can play an important role in assessing the environmental impacts of large-scale GWHP systems. It is noteworthy that the relative importance of the ratio can vary with the assessment time because the thermal states of temperature plumes in a short period of time are different depending on injection rates (see red dashed lines in Figure 5.18b).

Previous studies (Lo Russo et al., 2012; Molina-Giraldo et al., 2011; Park et al., 2015a; Park

et al., 2015b; Piga et al., 2017) used a fixed dispersivity ratio in the sensitivity analysis, making it difficult to determine the independent effect of longitudinal dispersivity alone. Figure 5.19 shows the results of the simulations, in which the longitudinal dispersivity was changed with respect to the fixed transverse dispersivity and hence its effect can be investigated independently. Figure 5.19a shows that the longitudinal dispersivity increases the plume length L_1 , showing that it can affect the thermal recycling between pumping and injection wells and thus the efficiency of the GWHP systems. As can be seen in Figure 5.19b and 5.19c, differently from the transverse dispersivity, the longitudinal dispersivity is important under transient conditions and this is consistent with the recent studies on vertical GSHP systems (Alcaraz et al., 2016; Molina-Giraldo et al., 2011). Note that the longitudinal dispersivity increases the upstream propagation of thermal plumes while it decreases the plume length L_2 and the plume width (Figure 5.19). Such decrease in the plume extensions was not observed in the short-term simulations (Lo Russo et al., 2012), but in the steady-state modeling using the fixed dispersivity ratio, it was considered as the effect of transverse thermal dispersivity (Molina-Giraldo et al., 2011). A possible explanation is that for steady state conditions the transverse dispersion dominates over the longitudinal dispersion (Metzger et al., 2004; Molina-Giraldo et al., 2011) but the latter also contributes to the energy dissipation.

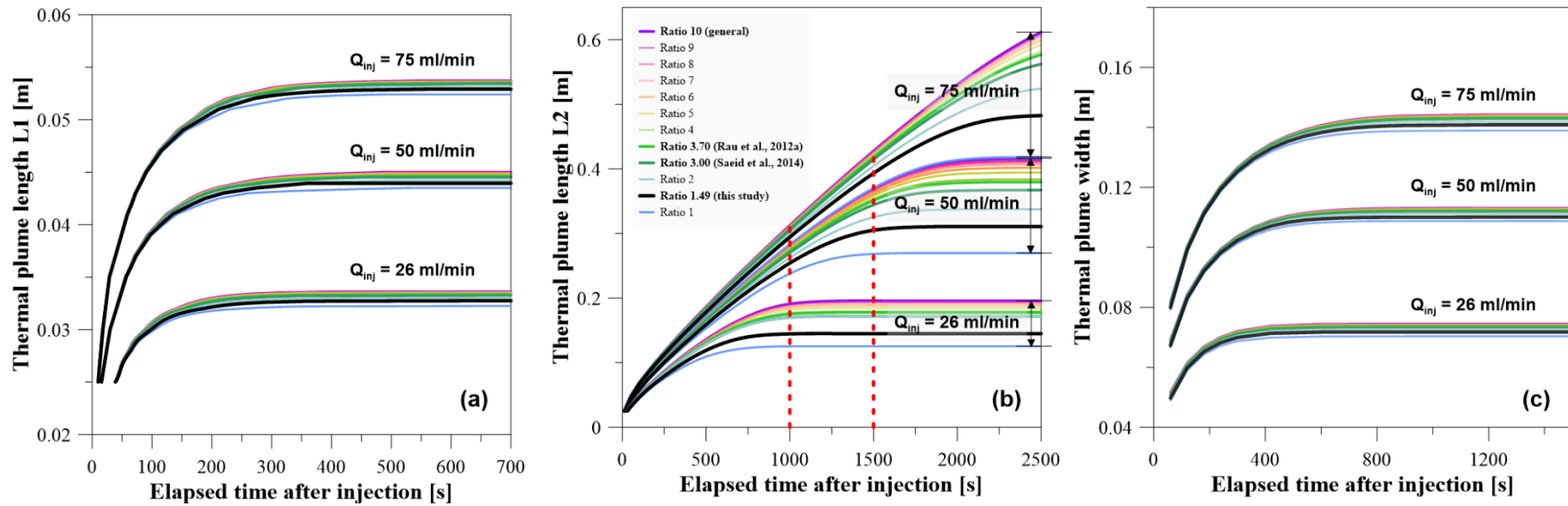


Figure 5.18. Impact of injection rate on thermal plume dimensions of (a) plume length L1, (b) plume length L2, and (c) plume width with different thermal dispersivity ratios at a Darcy velocity of 29.47 m/d. The red dashed lines indicate the assessment time for the thermal plume extensions as examples. For $t = 1000$ s, the effect of dispersivity ratios is largest for $Q_{inj} = 26$ ml/min, while it is largest for $Q_{inj} = 50$ ml/min for $t = 1500$ s.

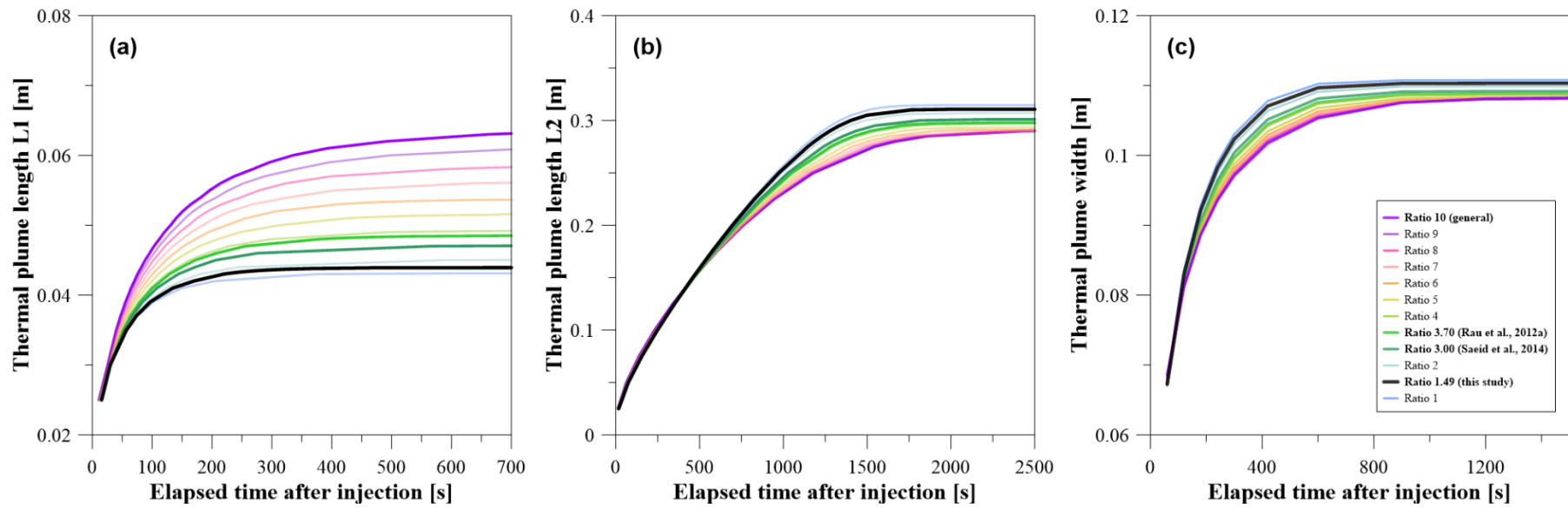


Figure 5.19. Independent influence of longitudinal thermal dispersivity on thermal plume dimensions of (a) plume length L1, (b) plume length L2, and (c) plume width with an injection rate of 50 ml/min at a Darcy velocity of 29.47 m/d.

In recent years, the importance of thermal dispersion has been reported in the field of shallow geothermal energy. Most studies, however, have assumed the ratio of longitudinal to transverse dispersivity values to be 10. Because the thermal dispersivity depends on the thermal properties and the geometry of materials (Rau et al., 2012a; Yuan et al., 1991), its ratio can also be affected by the heterogeneous properties and the structure of the porous medium. Experimental investigations in this chapter support the previous finding (Chapter 4; Park et al., 2018) that the thermal dispersivity ratio can be different from the general assumption. Numerical investigations also confirmed that the dispersivity ratio can play a significant role in assessing the environmental impacts, particularly for large-scale GWHP facilities under steady-state conditions (Figure 5.18). Although the thermal dispersivity values estimated in the present chapter were very small because sub-meter scale experiments were performed with relatively homogeneous materials ($U < 1.50$), the macroscopic dispersivity can be greater by several orders of magnitude (see Stauffer et al., 2013) depending on the degree of aquifer heterogeneity and the scale of measurement (Chang & Yeh, 2012; Sauty et al., 1982; Zech et al., 2015). Therefore, it is necessary to evaluate their relationship as well as their magnitude through field experiments to ensure the sustainable use of shallow groundwater as a renewable energy source.

5.5. Conclusions

Experimental investigations were conducted on the validity of the general assumption that the transverse dispersivity is one-tenth that of the longitudinal dispersivity. For this purpose, heat transport experiments on the sub-meter scale were performed using two different heat sources of the resistor and warm water at various background flow velocities ($Re < 0.3$). Two analytical models describing the subsurface heat transport processes with/without background water flow were employed to analyze the resistor experiments and estimate the thermal properties of the saturated coarse sands.

A linear regression method was applied to quantify the relationships between thermal parameters and derive the thermal dispersivity values. For low flow velocity ($Pe^l < 0.2$), it was difficult to find a clear trend in the relationships mainly due to the scatter (Figure 5.10). The scatter can be explained by three reasons, namely conduction dominant regime, nonuniform flow field, and inhomogeneity of thermal properties. The dispersivity values estimated from the regression models showed different ratios from the assumed value, suggesting that the dispersivity ratio may also vary depending on the porous medium as the dispersivity does.

Numerical simulations were conducted to investigate the effect and the significance of the thermal dispersivity ratio on the thermal plume propagation of the GWHP systems. For steady state conditions, the thermal plume dimension increases with the dispersivity ratio because the transverse dispersion is a dominant heat transport process and its decrease leads to the decrease in energy dissipation. It is noteworthy that the increase in the flow velocity can increase or decrease the plume length L_2 (Figure 5.13a) because the relative importance of advection and transverse dispersion varies with the dispersivity ratio.

Transient simulations for flow and heat transport showed that the impact of the dispersivity ratio is time dependent and anisotropic. The effect of dispersivity ratio on thermal plumes increases with time because the transverse dispersion dominates over the longitudinal dispersion for steady-state conditions. Its influence is also not isotropic because of the anisotropic velocity field caused by background flow and injected water. Therefore, using the assumed value as a dispersivity ratio can overestimate the environmental impacts of the GWHP systems, especially for long-term operations.

Numerical investigations also considered different injection rates and independent changes of longitudinal dispersivity. Higher injection rates strengthened the effect of dispersivity ratio on the downstream propagation of temperature plumes, indicating the significance of dispersivity ratio on the environmental impact assessment for large-scale GWHP facilities. The longitudinal dispersivity affected the upstream propagation of thermal plumes and thus can play an important role in ensuring the efficiency of the GWHP systems.

In recent years, a variety of studies have demonstrated that the thermal dispersion is a significant transport mechanism in the field of shallow geothermal applications. Most studies have used the assumed value as a thermal dispersivity ratio, and this might be due to the lack of information and reliable experimental data (Piga et al., 2017). Our results suggest that the thermal dispersivity ratio might be different depending on the porous medium, and the use of the general assumption can overestimate the environmental impacts, in particular, for large-scale GWHP plants under steady-state conditions. This can be a special issue for the sustainable use of shallow groundwater, especially in urban areas. Therefore, it is necessary to estimate the relationship as well as the magnitude for longitudinal and transverse dispersivity through field experiments.

Chapter 6

Concluding Remarks

GWHP systems can contribute to reducing carbon emission and ensuring energy security by making use of groundwater as a renewable and sustainable energy resource. Due to water injection after heat exchange to reduce hydraulic influences, however, they generate thermal plumes which can adversely affect the sustainable use of groundwater in neighboring facilities as well as the efficiency of GWHP systems. The prediction of thermal plume propagation is therefore of great importance in the design stage. Thermal plumes developing from injection wells transfer in saturated porous media by physical mechanisms of conduction, advection, and dispersion. In recent years, a lot of studies have been performed to evaluate the feasibility of GWHP systems for space heating and cooling of buildings, indicating that groundwater flow conditions are an important factor influencing system design. Most of them focused on investigating the thermal interference between pumping and injection wells under site-specific conditions, instead of fundamental physical processes behind the phenomenon. In particular, thermal dispersion has been underestimated in the simulation of subsurface heat transport processes by using default values in the simulator or solute dispersivity as thermal dispersivity

without any field-based evaluation. These conventions or assumptions may be based on the fact that thermal diffusion occurs hundreds times faster than solute diffusion and groundwater flow velocity is relatively slow. There are several clues that contradict such assumptions. Thermal dispersivity reported from field experiments has a wide range of values from 0.1 to 100 m, suggesting that it can be site-specific. The transport of heat and solute in porous media also has dissimilarity as well as similarity. Moreover, the increased flow velocity by pumping and injection in GWHP systems can change the relative importance of thermal diffusion and mechanical dispersion. This dissertation addressed these principal questions about the validity of the assumptions.

Field and numerical studies were performed in the alluvial aquifer near north Han river to investigate the importance of thermal dispersivity in designing GWHP systems. Experimental observations showed that mechanical dispersion can dominate over thermal diffusion even in natural flow condition. Numerical simulations indicated that thermal dispersivity has a great influence on both the subsurface temperature distribution and the extent of thermal plume, and its impact on flow and transport increases with pumping and injection rates. These results reveal that thermal dispersivity is of significance in the design of GWHP systems.

Recent studies have demonstrated that aquifer properties have a great effect on GWHP systems. Only a few studies, however, have analyzed their influences based on site-specific values. There is therefore a lack of information on the relative importance of the properties despite of its necessity in terms of time and cost for the aquifer characterization. In this sense, the developed field-based model has been extended to investigate the sensitivity of seven parameters characterizing aquifers under four different boundary conditions, taking into account changes in background flow rate and system capacity. The sensitivity analysis results

confirmed and developed the previous finding that hydrodynamic parameters have a significant influence on the dimension of thermal plumes, and thereby indicate that aquifer properties composing of mechanical dispersion term are influential in the thermal impact assessment of GWHP systems.

The results of sensitivity analyses, however, are based on the specific initial and boundary conditions constrained to the study area, and also short-term modeling results. Especially, the research site is represented by highly complex hydrogeological and thermal subsurface settings, which can not be repeated and reproduced. For these reasons, a precise laboratory experimental system for heat tracer tests was designed, developed, and assembled to examine the thermal dispersion behavior in fully saturated porous media under disturbed flow field by water injection of GWHP systems. In addition, physical properties of sand particles making up saturated porous media were repeatedly measured and their uncertainties were estimated.

The developed experimental system was employed to perform laboratory thermal tracer tests using two different heat sources at various background flow velocities. The main objective of the experiments was to investigate the influence of injected water on flow fields, thermal dispersion coefficients, and associated heat transport processes. Experimental and analytical results showed that thermal dispersion coefficients increase with flow velocities even in the conduction dominant regime, but there is also scatter in the relations between them. This work found that the heterogeneity of thermal properties can be another reason for the scatter, with thermal regime and flow field. Numerical results indicate that injected water greatly increases both flow velocities and thermal dispersion coefficients, letting the regions around the injection well stay in transition zone or convection dominant regime, and thus making mechanical dispersion important even at low background flow velocity. Field-based modeling results also

suggest that the radius of hydraulic and thermal influences can be increased significantly on the field scale.

Analysis results for heat tracer tests also indicated that the relationship between longitudinal and transverse thermal dispersivity can be different from the generally assumed value of 10. Therefore, additional heat transport experiments were repeatedly conducted using two different sands as a porous medium to investigate the validity of the general assumption on thermal dispersivity ratio, and its influence on thermal plume propagation. The results support the previous interpretation that the scatter can be explained by three reasons, and also confirm that the assumption can be violated. Numerical results show that the effect of thermal dispersivity ratio is time-dependent, anisotropic, and varying with injection rates, indicating that it can be significant in assessing the long-term environmental impacts for large-scale GWHP facilities.

This dissertation describes the significance and role of thermal dispersion on the subsurface heat transport processes for using groundwater as a renewable and sustainable energy resource. GWHP systems have high potential to reduce carbon footprint and energy costs, but they are not always efficient and sustainable. In this regard, the results of this study can be helpful to lessen thermal risks and improve environmental and economic benefits. In addition, the results can also enable the better prediction of thermal plumes, help to manage and regulate the potential risks, and thus contribute to groundwater and energy policies. This work can also deepen the understanding of subsurface heat transport processes, and thereby contribute to a variety of researches using heat as a tracer in saturated porous media.

Bibliography

- Alcaraz, M., García-Gil, A., Vázquez-Suñé, E., & Velasco, V. (2016). Advection and dispersion heat transport mechanisms in the quantification of shallow geothermal resources and associated environmental impacts. *Sci. Total Environ.* 543, 536–546. <https://doi.org/10.1016/j.scitotenv.2015.11.022>
- Anderson, M. P. (2005). Heat as a ground water tracer. *Groundwater* 2005, 43(6), 951–968. <https://doi.org/10.1111/j.1745-6584.2005.00052.x>
- Anderson, M. P., & Woessner, W. W. (1992). *Applied Groundwater Modeling: Simulation of Flow and Advective Transport*, San Diego, CA: Academic Press Inc.
- Andrews, C. B., & Anderson, M. P. (1979). Thermal alteration of groundwater caused by seepage from a cooling lake. *Water Resour. Res.* 15(3), 595–602. <https://doi.org/10.1029/WR015i003p00595>
- Al-Zyoud, S., Rühaak, W., & Sass, I. (2014). Dynamic numerical modeling of the usage of groundwater for cooling in north east Jordan – A geothermal case study. *Renew. Energ.* 62, 63–72. <https://doi.org/10.1016/j.renene.2013.06.027>
- Balland, V., & Arp, P. A. (2005). Modeling soil thermal conductivities over a wide range of conditions. *J. Environ. Eng. Sci.* 4, 549–558. <https://doi.org/10.1139/S05-007>
- Bandai, T., Hamamoto, S., Rau, G.C., Komatsu, T., & Nishimura, T. (2017). The effect of

- particle size on thermal and solute dispersion in saturated porous media. *Int. J. Therm. Sci.* 122, 74–84. <https://doi.org/10.1016/j.ijthermalsci.2017.08.003>
- Banks, D. (2009). Thermogeological assessment of open-loop well-doublet schemes: a review and synthesis of analytical approaches. *Hydrogeol. J.* 17(5), 1149–1155. <https://doi.org/10.1007/s10040-008-0427-6>
- Banks, D. (2012). *An introduction to thermogeology: ground source heating and cooling*. Chichester, UK: John Wiley & Sons.
- Bayer, P., Saner, D., Bolay, S., Rybach, L., & Blum, P. (2012). Greenhouse gas emission savings of ground source heat pump systems in Europe: a review. *Renew. Sustain. Energy Rev.* 16(2), 1256–1267. <https://doi.org/10.1016/j.rser.2011.09.027>
- Bear, J. (1972). *Dynamics of fluids in porous media*. New York, NY: Elsevier.
- Beretta, G. P., Coppola, G., & Della Pona, L. (2014). Solute and heat transport in groundwater similarity: Model application of a high capacity open-loop heat pump. *Geothermics* 51, 63–70.
- Bons, P. D., van Milligen, B. P., & Blum, P. (2013). A general unified expression for solute and heat dispersion in homogeneous porous media. *Water Resour. Res.* 49(10), 6166–6178. <https://doi.org/10.1002/wrcr.20488>
- Buntebarth, G., & Schopper, J. R. (1998). Experimental and theoretical investigations on the influence of fluids, solids and interactions between them on thermal properties of porous rocks. *Phys. Chem. Earth* 23(9–10), 1141–1146. [https://doi.org/10.1016/S0079-1946\(98\)00142-6](https://doi.org/10.1016/S0079-1946(98)00142-6)

- Carslaw, H. S., & Jaeger, J. C. (1959). *Conduction of heat in solids*. New York, NY: Oxford University Press.
- Casasso, A., & Sethi, R. (2014). Efficiency of closed loop geothermal heat pumps: A sensitivity analysis. *Renew. Energ.* 62, 737–746. <https://doi.org/10.1016/j.renene.2013.08.019>
- Casasso, A., & Sethi, R. (2015). Modelling thermal recycling occurring in groundwater heat pumps (GWHPs). *Renew. Energ.* 77, 86–93. <https://doi.org/10.1016/j.renene.2014.12.003>
- Cha, J. H., Myoung, D. W., Koo, M. H., Song, Y. H., & Kim, H. C. (2007). Analysis for the thermal properties by rock type in South Korea. *The Korean Society for New and Renewable Energy (KSNRE)* 6, 493–496. [in Korean]
- Chang, C. M., & Yeh, H. D. (2012). Stochastic analysis of field-scale heat advection in heterogeneous aquifers. *Hydrol. Earth Syst. Sc.* 16(3), 641–648. <https://doi.org/10.5194/hess-16-641-2012>
- Constantz, J. (1998). Interaction between stream temperature, streamflow, and groundwater exchanges in alpine streams. *Water Resour. Res.* 34(7), 1609–1615. <https://doi.org/10.1029/98WR00998>
- Constantz, J., & Thomas, C. L. (1997). Streambed temperatures profiles as indicators of percolation characteristics beneath arroyos in the Middle Rio Grande Basin, USA. *Hydrol. Process.* 11(12), 1621–1634. [https://doi.org/10.1002/\(SICI\)1099-1085\(19971015\)11:12<1621::AID-HYP493>3.0.CO;2-X](https://doi.org/10.1002/(SICI)1099-1085(19971015)11:12<1621::AID-HYP493>3.0.CO;2-X)
- Constantz, J., Thomas, C. L., & Zellweger, G. (1994). Influence of diurnal variations in stream temperature on streamflow loss and groundwater recharge. *Water Resour. Res.* 30(12),

3253–3264. <https://doi.org/10.1029/94WR01968>

Cooper Jr, H. H., & Jacob, C. E. (1946). A generalized graphical method for evaluating formation constants and summarizing well-field history. *Eos, Transactions American Geophysical Union* 27(4), 526–534.

de Marsily, G. (1986). *Quantitative hydrogeology: groundwater hydrology for engineers*. San Diego, CA: Academic.

De Rosa, M., Bianco, V., Scarpa, F., & Tagliafico, L. A. (2014). Heating and cooling building energy demand evaluation; a simplified model and a modified degree days approach. *Appl. Energ.* 128, 217–229. <https://doi.org/10.1016/j.apenergy.2014.04.067>

Diersch, H. J. G. (2005a). *Reference Manual for FEFLOW[®]*. Berlin, Germany: WASY GmbH.

Diersch, H. J. G. (2005b). Discrete feature modeling of flow, mass and heat transport processes by using FEFLOW. *White Papers* 1, 147–190.

Dwyer, T. E., & Eckstein, Y. (1987). Finite-element simulation of low-temperature, heat-pump-coupled, aquifer thermal energy storage. *J. Hydrol.* 95(1–2), 19–38. [https://doi.org/10.1016/0022-1694\(87\)90113-2](https://doi.org/10.1016/0022-1694(87)90113-2)

Fetter, C. W. (2001). *Applied Hydrogeology*. Upper Saddle River, NJ: Prentice-Hall Inc.

Ferguson, G., & Bense, V. (2011). Uncertainty in 1D heat-flow analysis to estimate groundwater discharge to a stream. *Groundwater* 49(3), 336–347. <https://doi.org/10.1111/j.1745-6584.2010.00735.x>

Ferguson, G., & Woodbury, A. D. (2005). Thermal sustainability of groundwater-source cooling in Winnipeg, Manitoba. *Can. Geotech. J.* 42(5), 1290–1301. <https://doi.org/>

10.1139/t05-057

- Ferguson, G., & Woodbury, A. D. (2006). Observed thermal pollution and post-development simulations of low-temperature geothermal systems in Winnipeg, Canada. *Hydrogeol. J.* 14, 1206–1215. <https://doi.org/10.1007/s10040-006-0047-y>
- Ferguson, G. (2007). Heterogeneity and thermal modeling of ground water. *Groundwater* 45(4), 485–490. <https://doi.org/10.1111/j.1745-6584.2007.00323.x>
- Florides, G., & Kalogirou, S. (2005). Annual ground temperature measurements at various depths. 8th Rehva World Congress, Clima, Lausanne. <https://ktisis.cut.ac.cy/handle/10488/844>
- Freeze, R. A., & Cherry, J. A. (1979). *Groundwater*. Upper Saddle River, NJ: Prentice-Hall Inc.
- Friedman, G. M., & Sanders, J. E. (1978). *Principles of sedimentology*. New York, NY: Wiley.
- Gao, Q., Zhou, X. Z., Jiang, Y., Chen, X. L., & Yan, Y. Y. (2013). Numerical simulation of the thermal interaction between pumping and injecting well groups. *Applied thermal engineering* 51(1–2), 10–19. <https://doi.org/10.1016/j.applthermaleng.2012.09.017>
- Green, D. W., Perry, R. H., & Babcock, R. E. (1964). Longitudinal dispersion of thermal energy through porous media with a flowing fluid. *AIChE J.* 10, 645–651. <https://doi.org/10.1002/aic.690100514>
- Hatch, C. E., Fisher, A. T., Revenaugh, J. S., Constantz, J., & Ruehl, C. (2006). Quantifying surface water–groundwater interactions using time series analysis of streambed thermal records: Method development. *Water Resour. Res.* 42(10), W10410. <https://doi.org/10.1029/2005WR004787>

- Hidalgo, J. J., Carrera, J., & Dentz, M. (2009). Steady state heat transport in 3D heterogeneous porous media. *Adv. Water Resour.* 32(8), 1206–1212. <https://doi.org/10.1016/j.advwatres.2009.04.003>
- Hopmans, J. W., Šimunek, J., & Bristow, K. L. (2002). Indirect estimation of soil thermal properties and water flux using heat pulse probe measurements: Geometry and dispersion effects. *Water Resour. Res.* 38(1), 7-1–7-14. <http://dx.doi.org/10.1029/2000WR000071>
- Isaac, M., & Van Vuuren, D. P. (2009). Modeling global residential sector energy demand for heating and air conditioning in the context of climate change. *Energ. policy* 37(2), 507–521. <https://doi.org/10.1016/j.enpol.2008.09.051>
- Johnson, A. I. (1967). Specific yield-Compilation of specific yields for various materials, 74 pp., *U.S. Geol. Surv. Water Supply Pap.*, 1662-D
- Kaown, D., Koh, E. H., Mayer, B., Kim, H., Park, D. K., Park, B. H., & Lee, K. K. (2018). Application of multiple-isotope and groundwater-age data to identify factors affecting the extent of denitrification in a shallow aquifer near a river in South Korea. *Hydrogeol. J.* 26(6), 2009–2020. <https://doi.org/10.1007/s10040-017-1716-8>
- Kearl, P. M. (1997). Observations of particle movement in a monitoring well using the colloidal borescope. *J. Hydrol.* 200(1–4), 323–344. [https://doi.org/10.1016/S0022-1694\(97\)00026-7](https://doi.org/10.1016/S0022-1694(97)00026-7)
- KEEI (Korea Energy Economics Institute) (2015). *Yearbook of energy statistics 2014*. Ulsan, South Korea: KEEI. [in Korean]
- Keery, J., Binley, A., Crook, N., & Smith, J. W. (2007). Temporal and spatial variability of groundwater–surface water fluxes: development and application of an analytical method

- using temperature time series. *J. Hydrol.* 336(1–2), 1–16. <https://doi.org/10.1016/j.jhydrol.2006.12.003>
- KEMCO (Korea Energy Management Corporation) (2011). *New and Renewable Energy RD&D Strategy 2030: Geotherm.* Yongin, South Korea: KEMCO. [in Korean]
- KEMCO (Korea Energy Management Corporation) (2013). *New and Renewable Energy Statistics 2012.* Yongin, South Korea: KEMCO. [in Korean]
- Kim, S. K., Bae, G. O., Lee, K. K., Shim, B. O., & Song, Y. (2008). Model Development to Simulate Geothermal Heat Transport and Sensitivity Analyses on the Design Parameters of Closed-loop Geothermal Heat Pump System. *The Korean Society for Geosystem Engineering* 45(4), 326–336. [in Korean]
- Kim, H., Nam, Y., & Jeoun, O. (2018). Development of a multi-well pairing system for groundwater heat pump systems. *Energies* 11(12), 3485. <https://doi.org/10.3390/en1123485>
- Kim, J., Park, Y., & Harmon, T. C. (2005). Real-time model parameter estimation for analyzing transport in porous media. *Groundwater Monit. Rem.* 25(2), 78-86. <https://doi.org/10.1111/j.1745-6592.2005.0018.x>
- KMA (Korea Meteorological Administration) (2014). *Annual Report of Automatic Weather Station Data 2004–2013.* Seoul, South Korea: KMA. [in Korean]
- Kunii, D., & Smith, J. M. (1961). Heat transfer characteristics of porous rocks: II. Thermal conductivities of unconsolidated particles with flowing fluids. *AIChE J.* 7(1), 29–34. <https://doi.org/10.1002/aic.690070109>

- Kwon K. S., Lee J. Y., & Mok J. K. (2012). Update of Current Status on Ground Source Heat Pumps in Korea (2008–2011), *Journal of the Geological Society of Korea* 48(2), 193–199. [in Korean]
- Leaf, A. T., Hart, D. J., & Bahr, J. M. (2012). Active thermal tracer tests for improved hydrostratigraphic characterization. *Groundwater* 50(5), 726–35. <https://doi.org/10.1111/j.1745-6584.2012.00913.x>
- Lee J. Y. (2009). Current status of ground source heat pumps in Korea. *Renew. Sustain. Energy Rev.* 13, 1560–1568. <https://doi.org/10.1016/j.rser.2008.10.005>
- Lee, S., Lee, K. K., & Yoon, H. (2019). Using artificial neural network models for groundwater level forecasting and assessment of the relative impacts of influencing factors. *Hydrogeol. J.* 27(7), 567–579. <https://doi.org/10.1007/s10040-018-1866-3>
- Lee J. Y., Won J. H., & Hahn J. S. (2006). Evaluation of hydrogeologic conditions for groundwater heat pumps: analysis with data from national groundwater monitoring stations. *Geosciences Journal* 10(1), 91–99.
- Levec, J., & Carbonell, R. G. (1985). Longitudinal and Lateral Thermal Dispersion in Packed Beds Part 2. Comparison between Theory and Experiment. *Aiche Journal* 31(4), 591–602. <https://doi.org/10.1002/aic.690310409>
- Lo Russo, S., & Civita, M. V. (2009). Open-loop groundwater heat pumps development for large buildings: a case study. *Geothermics* 38, 335–345. <http://dx.doi.org/10.1016/j.geothermics.2008.12.009>
- Lo Russo, S., Taddia, G., Baccino, G., & Verda, V. (2011). Different design scenarios related to an open loop groundwater heat pump in a large building: Impact on subsurface and

- primary energy consumption. *Energy Build.* 43, 347–357. <https://doi.org/10.1016/j.enbuild.2010.09.026>
- Lo Russo, S., Taddia, G., & Verda, V. (2012). Development of the thermally affected zone (TAZ) around a groundwater heat pump (GWHP) system: A sensitivity analysis. *Geothermics* 43, 66–74. <https://doi.org/10.1016/j.geothermics.2012.02.001>
- Lo Russo, S., Taddia, G., & Abdin, E. C. (2018). Modeling the effects of the variability of temperature-related dynamic viscosity on the thermal-affected zone of groundwater heat-pump systems. *Hydrogeol. J.* 26(4), 1239–1247. <https://doi.org/10.1007/s10040-017-1714-x>
- Lu, X., Ren, T., & Gong, Y. (2009). Experimental investigation of thermal dispersion in saturated soils with one-dimensional water flow. *Soil Sci. Soc. Am. J.* 73(6), 1912–1920. <http://dx.doi.org/10.2136/sssaj2008.0251>
- Ma, R., & Zheng, C. (2010). Effects of density and viscosity in modeling heat as a groundwater tracer. *Groundwater* 48(3), 380–389. <https://doi.org/10.1111/j.1745-6584.2009.00660.x>
- Ma, R., Zheng, C., Zachara, J. M., & Tonkin, M. (2012). Utility of bromide and heat tracers for aquifer characterization affected by highly transient flow conditions. *Water Resour. Res.* 48(8), W08523. <https://doi.org/10.1029/2011WR011281>
- Metzger, T., Didierjean, S., & Maillet, D. (2004). Optimal experimental estimation of thermal dispersion coefficients in porous media. *Int. J. Heat Mass Tran.* 47, 3341–3353. <https://doi.org/10.1016/j.ijheatmasstransfer.2004.02.024>
- Michopoulos, A., Bozis, D., Kikidis, P., Papakostas, K., & Kyriakis, N. A. (2007). Three-years operation experience of a ground source heat pump system in Northern Greece. *Energy*

Build. 39, 328–334. <https://doi.org/10.1016/j.enbuild.2006.08.002>

Miotliński, K., Dillon, P. J., Pavelic, P., Cook, P. G., Page, D. W., & Levett, K. (2011). Recovery of injected freshwater to differentiate fracture flow in a low-permeability brackish aquifer. *J. Hydrol.* 409, 273–282.

Mok, J. G., Lim H. G., Jang B. J., Park Y. C., & Lee J. Y. (2010). Time Series Analysis of the Effect of Ground-source Heat Pumps on Groundwater Characteristics. *The Journal of Engineering Geology.* 21(1), 35–43. [in Korean with English abstract]

Molina-Giraldo, N., Bayer, P., & Blum, P. (2011). Evaluating the influence of thermal dispersion on temperature plumes from geothermal systems using analytical solutions. *Int. J. Therm. Sci.* 50(7), 1223–1231. <https://doi.org/10.1016/j.ijthermalsci.2011.02.004>

Molson, J. W., Frind, E. O., & Palmer, C. D. (1992). Thermal energy storage in an unconfined aquifer: 2. Model development, validation, and application. *Water Resour. Res.* 28(10), 2857–2867. <https://doi.org/10.1029/92WR01472>

Mourshed, M. (2011). The impact of the projected changes in temperature on heating and cooling requirements in buildings in Dhaka, Bangladesh. *Appl. Energ.* 88(11), 3737–3746. <https://doi.org/10.1016/j.apenergy.2014.04.067>

Nam, Y. J., & Ooka, R. (2010). Numerical simulation of ground heat and water transfer for groundwater heat pump system based on real-scale experiment. *Energy Build.* 42, 69–75. <https://doi.org/10.1016/j.enbuild.2009.07.012>

NIST (2019). *NIST Chemistry Webbook*. <http://webbook.nist.gov/chemistry/fluid/> [accessed March 5, 2019]

- Ozlu, S., Dincer, I., & Naterer, G. F. (2012). Comparative assessment of residential energy options in Ontario, Canada. *Energy Build.* 55, 674–684. <https://doi.org/10.1016/j.enbuild.2012.09.033>
- Park, B. H., Kim, H. S., & Lee, K. K. (2013). A verification study on saving energy cost and reducing CO₂ emission with large-scale geothermal heat pump systems in Korea. *J. Renew. Sustain. Ener.* 5(5), 052009. <https://doi.org/10.1063/1.4824983>
- Park, B. H., Bae, G. O., & Lee, K. K. (2015a). Importance of thermal dispersivity in designing groundwater heat pump (GWHP) system: Field and numerical study. *Renew. Energ.* 83, 270–279. <https://doi.org/10.1016/j.renene.2015.04.036>
- Park, B. H., Joun, W. T., Lee, B. H., & Lee, K. K. (2015b). A study on significant parameters for efficient design of open-loop groundwater heat pump (GWHP) systems. *J. Soil Groundw. Environ.* 20(4), 41–50. <https://doi.org/10.7857/JSGE.2015.20.4.041> [in Korean with English abstract]
- Park, B. H., Ha, S. W., & Lee, K. K. (2017). Minimum Well Separation for small groundwater heat pump (GWHP) systems in Korea: preliminary analysis based on regional aquifer properties, *IGSHPA Conference & Expo 2017*, 186–191. <https://doi.org/10.22488/okstate.17.000515>
- Park, B. H., Lee, B. H., & Lee, K. K. (2018). Experimental investigation of the thermal dispersion coefficient under forced groundwater flow for designing an optimal groundwater heat pump (GWHP) system. *J. Hydrol.* 562, 385–96. <https://doi.org/10.1016/j.jhydrol.2018.05.023>
- Piga, B., Casasso, A., Pace, F., Godio, A., & Sethi, R. (2017). Thermal impact assessment of

- groundwater heat pumps (GWHPs): rigorous vs. simplified models. *Energies* 10(9), 1385.
<https://doi.org/10.3390/en10091385>
- Pophillat, W., Attard, G., Bayer, P., Hecht-Méndez, J., & Blum, P. (2018). Analytical solutions for predicting thermal plumes of groundwater heat pump systems. *Renew. Energ.* <https://doi.org/10.1016/j.renene.2018.07.148>
- Rau, G. C., Andersen, M. S., McCallum, A. M., & Acworth, R. I. (2010). Analytical methods that use natural heat as a tracer to quantify surface water–groundwater exchange, evaluated using field temperature records. *Hydrogeol. J.* 18(5), 1093–1110. <https://doi.org/10.1007/s10040-010-0586-0>
- Rau, G. C., Andersen, M. S., & Acworth, R. I. (2012a). Experimental investigation of the thermal dispersivity term and its significance in the heat transport equation for flow in sediments. *Water Resour. Res.* 48, W03511. <http://dx.doi.org/10.1029/2011WR011038>
- Rau, G. C., Andersen, M. S., & Acworth, R. I. (2012b). Experimental investigation of the thermal time-series method for surface water-groundwater interactions. *Water Resour. Res.* 48(3), W03530. <https://doi.org/10.1029/2011WR011560>
- Rau, G. C., Andersen, M. S., McCallum, G. C., Roshan, H., & Acworth, R. I. (2014). Heat as a tracer to quantify water flow in near-surface sediments. *Earth-Sci. Rev.* 129, 40–58. <http://dx.doi.org/10.1016/j.earscirev.2013.10.015>
- Saeid, S., Al-Khoury, R., Nick, H. M., & Barends, F. (2014). Experimental–numerical study of heat flow in deep low-enthalpy geothermal conditions. *Renew. Energ.* 62, 716–730. <https://doi.org/10.1016/j.renene.2013.08.037>
- Sauty, J. P., Gringarten, A. C., Fabris, H., Thiéry, D., Menjoz, A., & Landel, P. A. (1982).

- Sensible energy storage in aquifers: 2. Field experiments and comparison with theoretical results. *Water Resour. Res.* 18(2), 253–265. <https://doi.org/10.1029/WR018i002p00253>
- Schärli, U., & Rybach, L. (2001). Determination of specific heat capacity on rock fragments. *Geothermics* 30(1), 93–110. [https://doi.org/10.1016/S0375-6505\(00\)00035-3](https://doi.org/10.1016/S0375-6505(00)00035-3)
- Schornerberg, C., Schmidt, C., Kalbus, E., & Fleckenstein, J. H. (2010). Simulating the effects of geologic heterogeneity and transient boundary conditions on streambed temperatures—Implications for temperature-based water flux calculations. *Adv. Water Resour.* 33(11), 1309–1319. <https://doi.org/10.1016/j.advwatres.2010.04.007>
- Smith, L., & Chapman, D. S. (1983). On the thermal effects of groundwater flow: 1. Regional scale systems. *J. Geophys. Res.: Solid Earth* 88(B1), 593–608. <https://doi.org/10.1029/JB088iB01p00593>
- Su, G. W., Jasperse, J., Seymour, D., & Constantz, J. (2004). Estimation of hydraulic conductivity in an alluvial system using temperatures. *Groundwater* 42(6), 890–902. <https://doi.org/10.1111/j.1745-6584.2004.t01-7-.x>
- Stauffer, F., Bayer, P., Blum, P., Molina-Giraldo, N., & Kinzelbach, W. (2013). *Thermal use of shallow groundwater*. Boca Raton, FL: CRC Press.
- Taylor, J. R. (1997). *Introduction to error analysis, the study of uncertainties in physical measurements*. Sausalito, CA: University Science Books.
- Testu, A., Didierjean, S., Maillet, D., Moyne, C., Metzger, T., & Niass, T. (2007). Thermal dispersion for water or air flow through a bed of glass beads. *Int. J. Heat Mass Tran.* 50, 1469–1484. <https://doi.org/10.1016/j.ijheatmasstransfer.2006.09.002>

- Theis, C. V. (1935). The relation between the lowering of the piezometric surface and the rate and duration of discharge of a well using ground-water storage. *Eos, Transactions American Geophysical Union* 16(2), 519–524.
- Tu, K., Wu, Q., & Sun, H. (2019). A mathematical model and thermal performance analysis of single-well circulation (SWC) coupled ground source heat pump (GSHP) systems. *Appl. Therm. Eng.* 147, 473–481. <https://doi.org/10.1016/j.applthermaleng.2018.09.029>
- Vandenbohede, A., & Lebbe, L. (2010). Parameter estimation based on vertical heat transport in the surficial zone. *Hydrogeol. J.* 18(4), 931–943. <https://doi.org/10.1007/s10040-009-0557-5>
- Vandenbohede, A., Louwyck, A., & Lebbe, L. (2009). Conservative solute versus heat transport in porous media during push-pull tests. *Transp. Porous Media* 76(2), 265–287. <https://doi.org/10.1007/s11242-008-9246-4>
- Ward, J. D., Simmons, C. T., & Dillon, P. J. (2007). A theoretical analysis of mixed convection in aquifer storage and recovery: How important are density effects?. *J. Hydrol.* 343, 169–186. <https://doi.org/10.1016/j.jhydrol.2007.06.011>
- Woodside, W., & Messmer, J. H. (1961). Thermal conductivity of porous media. I. Unconsolidated sands. *J. Appl. Phys.* 32(9), 1688–1699. <https://doi.org/10.1063/1.1728419>
- Xue, Y., Xie, C., & Li, Q. (1990). Aquifer thermal energy storage: a numerical simulation of field experiments in China. *Water Resour. Res.* 26(10), 2365–2375. <https://doi.org/10.1029/WR026i010p02365>
- Yagi, S., Kunii, D., & Wakao, N. (1960). Studies on axial effective thermal conductivities in

packed beds. *AIChE J.* 6(4), 543–546. <https://doi.org/10.1002/aic.690060407>

Yeh, T.-C. J., Khaleel, R., & Carroll K. C. (2015). *Flow Through Heterogeneous Geologic Media*, New York, NY: Cambridge University Press.

Yuan, Z. G., Somerton, W. H., & Udell, K. S. (1991). Thermal dispersion in thick-walled tubes as a model of porous media. *Int. J. Heat Mass Tran.* 34(11), 2715–2726. [https://doi.org/10.1016/0017-9310\(91\)90230-C](https://doi.org/10.1016/0017-9310(91)90230-C)

Zech, A., Attinger, S., Cvetkovic, V., Dagan, G., Dietrich, P., Fiori, A., Rubin, Y., & Teutsch, G. (2015). Is unique scaling of aquifer macrodispersivity supported by field data?. *Water Resour. Res.* 51(9), 7662–7679. <https://doi.org/10.1002/2015WR017220>

Zhou, X., Gao, Q., Chen, X., Yu, M., & Zhao, X. (2013). Numerically simulating the thermal behaviors in groundwater wells of groundwater heat pump. *Energy* 61, 240–247. <https://doi.org/10.1016/j.energy.2013.09.020>

Appendix

A. Uncertainty Analysis

The uncertainty of the quantity x is denoted as E_x , and its relative uncertainty as e_x . The uncertainty analysis method and procedure are referred to the literature (Taylor, 1997).

A.1. Uncertainty in physical properties

In this study, physical properties of porous media were estimated on the basis of repeated measurements. The best estimate for N measurements of the quantity x is their mean \bar{x} , and its uncertainty is given as:

$$E_{\bar{x}} = \sqrt{\frac{\sum(x_i - \bar{x})^2}{N(N-1)}} \quad (\text{A1})$$

A.2. Uncertainty in dimensionless numbers

The dimensionless numbers Re and Pe^t are represented in equations (4.19) and (4.18), respectively. If they are independent and random, the uncertainties in the product and quotient are given as the quadratic sum of the relative uncertainties. Therefore, the uncertainties can be estimated as:

$$E_{Re} = Re \times \sqrt{e_{\rho_w}^2 + e_q^2 + e_{d_{50}}^2 + e_{\mu}^2} \approx Re \times \sqrt{e_q^2 + e_{d_{50}}^2} \quad (A2)$$

$$E_{Pe^t} = Pe^t \times \sqrt{e_{\rho_w c_w}^2 + e_q^2 + e_{d_{50}}^2 + e_{\lambda}^2} \approx Pe^t \times \sqrt{e_q^2 + e_{d_{50}}^2 + e_{\lambda}^2} \quad (A3)$$

The uncertainties in the water properties (NIST, 2019) were assumed to be negligible. The estimated uncertainties for the dimensionless numbers were less than 2% of their best estimates.

A.3. Uncertainty in statistical models

The linear regression models were employed to estimate the hydraulic conductivity and the thermal dispersivity of the saturated coarse sands and they are given as:

$$y = A + Bx, \quad (A4)$$

where A and B are the coefficients of the regression models. The uncertainties in the estimated hydraulic conductivity and thermal dispersivity can be represented as:

$$E_B = \sqrt{\frac{1}{N-2} \sum (y_i - A - Bx_i)^2} \sqrt{\frac{N}{N \sum x_i^2 - (\sum x_i)^2}}. \quad (A5)$$

Research Outcomes

Peer Reviewed Paper

Park, B. H., & Lee, K. K. (In Preparation). Anisotropy Ratio of Thermal Dispersivity Affecting Plume Geometry for Groundwater Heat Pump (GWHP) Systems.

Park, B. H., Lee, B. H., & Lee, K. K. (2018). Experimental Investigation of the Thermal Dispersion Coefficient Under Forced Groundwater Flow for Designing an Optimal Groundwater Heat Pump (GWHP) System. *J. Hydrol.* 562, 385–396. <https://doi.org/10.1016/j.jhydrol.2018.05.023>

Kaown, D., Koh, E. H., Mayer, B., Kim, H., Park, D. K., **Park, B. H.**, & Lee, K. K. (2018). Application of multiple-isotope and groundwater-age data to identify factors affecting the extent of denitrification in a shallow aquifer near a river in South Korea. *Hydrogeol. J.* 26(6), 2009–2020. <https://doi.org/10.1007/s10040-017-1716-8>

Park, B. H., & Lee, K. K. (2018). Impacts of injection temperature on the relevant heat transport processes in groundwater heat pump (GWHP) systems. *IGSHPA Proceedings*, 432–438. <https://doi.org/10.22488/okstate.18.000042>

Ha, S. W., **Park, B. H.**, Lee, S. H., & Lee, K. K. (2017). Experimental and Numerical Study on Gaseous CO₂ Leakage through Shallow-depth Layered Porous Medium: Implication

for Leakage Detection Monitoring. *Energy Procedia* 114, 3033–3039. <https://doi.org/10.1016/j.egypro.2017.03.1431>

Park, B. H., Ha, S. W., & Lee, K. K. (2017). Minimum well separation for small groundwater heat pump (GWHP) systems in Korea: preliminary analysis based on regional aquifer properties. *IGSHPA Proceedings*, 186–191. <https://doi.org/10.22488/okstate.17.000515>

Park, B. H., Joun, W. T., Lee, B. H., & Lee, K. K. (2015b). A Study on Significant Parameters for Efficient Design of Open-loop Groundwater Heat Pump (GWHP) Systems. *J. Soil Groundw. Environ.* 20(4), 41-50. <https://doi.org/10.7857/JSGE.2015.20.4.041> [in Korean with English abstract]

Park, B. H., Bae, G. O., & Lee, K. K. (2015a). Importance of thermal dispersivity in designing groundwater heat pump (GWHP) system: Field and numerical study. *Renew. Energ.* 83, 270–279. <https://doi.org/10.1016/j.renene.2015.04.036>

Park, B. H., Kim, H. S., & Lee, K. K. (2013). A verification study on saving energy cost and reducing CO₂ emission with large-scale geothermal heat pump systems in Korea. *J. Renew. Sustain. Ener.* 5(5), 052009. <https://doi.org/10.1063/1.4824983>

Oral Presentations (in recent years and 1st author only).....

Park, B. H., & Lee, K. K. (2019). Role of thermal dispersivity ratio in predicting thermal plumes of groundwater heat pump (GWHP) systems. *2019 KSNRE Spring Meeting* in Busan, South Korea

Park, B. H., & Lee, K. K. (2019). Impacts of thermal dispersivity ratio on the relevant heat transport processes in groundwater heat pump (GWHP) systems. *2019 EGU General Assembly* in Vienna, Austria

Park, B. H., & Lee, K. K. (2018). Impacts of injection temperature on the relevant heat transport processes in groundwater heat pump (GWHP) systems, *2018 IGSHPA 2nd research track* in Stockholm, Sweden

Park, B. H., & Lee, K. K. (2018). Influence of density driven flow on the relevant heat transport processes in groundwater heat pump (GWHP) systems. *2018 IAH congress* in Daejeon, South Korea

Park, B. H., & Lee, K. K. (2018). Influence of water injection on the relevant heat transport processes in groundwater heat pump (GWHP) systems. *2018 IGSHPA conference and expo* in Orlando, Florida [30 min presentation]

Park, B. H., Jung, D., Lee, B. H. & Lee, K. K. (2017). Thermal dispersion behavior under the induced flow field by the GWHP system. *2017 GSA Annual Meeting* in Seattle, Washington

Park, B. H., Lee, B. H. & Lee, K. K. (2017). Experimental Study on Thermal Dispersion under disturbed flow field induced by GWHP systems. *2017 KSNRE Spring meeting* in Jeju, South Korea

Park, B. H., Ha, S. W. & Lee, K. K. (2017). Minimum well separation for small groundwater heat pump (GWHP) systems in Korea: preliminary analysis based on regional aquifer properties. *2017 IGSHPA 1st research track* in Denver, Colorado [60 min presentation]

Park, B. H., Kim, H. S. & Lee, K. K. (2016). Variability of energy demand for space heating and cooling and its effect on shallow geothermal applications. *2016 KSNRE Spring meeting* in Jeju, South Korea

Park, B. H., Lee, B. H., Jeon, W. T. & Lee, K. K. (2015). A study on the aquifer properties affecting the design of open-loop groundwater heat pump (GWHP) systems. *2015 KSNRE Spring meeting* in Jeju, South Korea

Honors and Awards.....

2017 Superior Presentation Winner. **Park, B. H.**, Lee, B. H. & Lee, K. K. (2017). Experimental Study on Thermal Dispersion under disturbed flow field induced by GWHP systems. *The Korean Society for New and Renewable Energy*.

2016 Excellent 100 in the National R & D Projects. Lee, K. K., **Park, B. H.**, Park, J. et al. (2016). High Performance System Development for Space Heating and Cooling Using Groundwater Energy. *Ministry of Science*.

2016 Superior Presentation Winner. Lee, B. H., **Park, B. H.**, & Lee, K. K. (2016). Thermal dispersion behavior under forced groundwater flow conditions in GWHP systems. *The Korean Society for New and Renewable Energy*.

Abstract in Korean

개방형 지열 시스템은 항상 효율적이고 지속 가능한 것은 아니다. 개방형 시스템은 대수층에 열 플룸을 생성시켜 시스템 효율과 지중 환경에 악영향을 미칠 수 있으므로 그에 대한 예측은 설계 단계에서 매우 중요한 문제이다. 생성된 열 플룸은 포화된 다공성 매질 내에서 전도, 이류 및 분산에 의해 이동할 수 있다. 그러나 열 분산은 현장 기반의 평가없이 수치 모델의 기본값이나 용질의 분산도를 열 분산도로 사용함으로써 지중 열 전달 과정에서 과소평가되어왔다. 이러한 관행이나 가정은 개방형 지열 시스템의 열적 영향을 평가하는데 결정적인 역할을 할 수 있지만, 지금까지는 완전히 검증되지 않았다.

층적 대수층에 대한 현장 및 수치 연구를 수행하여 개방형 지열 시스템에서 열 분산도의 중요성을 조사하였다. 수치적 분석은 열 분산도가 열 플룸의 범위뿐만 아니라 온도 분포에도 큰 영향을 미친다는 것을 나타낸다. 관측된 자료는 또한 자연적인 지하수 흐름 하에서도 기계적 열 분산이 열 확산에 비해 우세할 수 있음을 보여준다. 현장 기반 모델을 수정하여 대수층 특성의 역할을 살펴보았다. 민감도 분석을 통해 수력학적 변수들이 열 플룸의 발달에 영향을 준다는 선행 연구 결과를 확인하고 발전시켜, 기계적 열 분산을 구성하는 대수층 특성들이 개방

형 시스템의 열 플룸을 예측하는데 매우 중요하다는 것을 밝혔다.

흐름 및 온도에 대한 경계 조건을 제어하고 주입수로 인해 교란된 유동장에서 다공성 매질을 통한 열 분산 거동을 규명하고자 실내실험장치를 제작하였다. 두 개의 다른 열원을 사용하는 추적자 실험을 포화된 조립질 모래($d_{50} = 1.28 \text{ mm}$)에서 다양한 배경 유속($Re < 0.52$)과 함께 수행하였다. 실험 및 해석 모델은 열 분산 계수와 열 전달 속도 사이의 관계에 나타나는 산란을 전도 지배 영역, 불균일한 속도장 및 불균질한 열 물성에 의해 설명할 수 있음을 보여준다. 수치 모의 결과는 주입수가 유속 및 열 분산 계수를 크게 증가시킴으로써 주입점 주변 지역을 전이대나 대류 지배 영역에 머물게 한다는 것을 나타낸다. 따라서 낮은 유속에서도 기계적 열 분산이 중요해진다.

횡 방향 열 분산도가 종 방향 열 분산도의 10분의 1이라는 일반적인 가정의 타당성을 조사하고 이러한 가정이 열 플룸 전파에 미치는 영향을 분석하기 위해 추가적인 열 추적자 시험을 수행하였다. 실험 결과는 일반적인 가정이 위배될 수 있음을 확인한다. 수치 모델은 열 분산도 비율의 영향이 시간에 의존적이고 이방성을 가지며 주입량에 따라 달라진다는 것을 보여준다. 이러한 결과는 열 분산도 비율이 대규모 시설의 장기 환경 영향 평가에 중요할 수 있음을 나타낸다. 그러므로 개방형 지열 시스템의 설계 단계에서는 지속 가능성을 위해 분산도의 크기와 비율을 평가하고 이를 반영해야 한다.

본 연구는 지하수를 에너지 자원으로 활용할 때의 열 분산의 중요성과 역할

에 대해 기술한다. 본 연구의 결과들은 천부 지하수의 효율적이고 지속가능한 사
용뿐만 아니라 포화된 다공성 매질에서의 열 거동에도 중요한 함의를 지닌다.

주요어: 지하수 히트 펌프; 열 분산; 열 플룸; 열 분산도; 열 분산도 비율; 환경
영향; 지하수; 열 전달

학번: 2013-20331

